POWER MANAGEMENT FOR INTERNET OF BATTERY-LESS THINGS

A Dissertation
Presented to
The Academic Faculty

By

Qianao Ju

In Partial Fulfillment
of the Requirements for the Degree
Doctor of Philosophy in the
School of Electrical and Computer Engineering

Georgia Institute of Technology

May 2018

POWER MANAGEMENT FOR INTERNET OF BATTERY-LESS THINGS

Approved by:

Dr. Ying Zhang, Advisor
Associate Professor, School of Electrical and Computer Engineering
Georgia Institute of Technology

Dr. Mary Ann Weitnauer
Professor, School of Electrical and Computer Engineering
Georgia Institute of Technology

Dr. Raheem Beyah
Professor, School of Electrical and Computer Engineering
Georgia Institute of Technology

Dr. Linda M. Wills
Associate Professor, School of Electrical and Computer Engineering
Georgia Institute of Technology

Dr. Yang Wang
Associate Professor, School of Civil and Environmental Engineering
Georgia Institute of Technology

Date Approved: March 28, 2018

Life never gives anything for nothing, and that a price is always exacted for what fate bestows.

Stefan Zweig

To my wife Yanming and my parents.

ACKNOWLEDGEMENTS

First and foremost, I would like to thank my advisor, Dr. Ying Zhang, for her tireless guidance and support during my PhD study. Her knowledge, enthusiasm and patience helped me go through the ups and downs. I feel lucky to have had the chance to work with Dr. Zhang, and will always be grateful for her mentorship.

I would like to thank Dr. Mary Ann Weitnauer, Dr Raheem Beyah, Dr. Linda M. Wills and Dr. Yang Wang for serving on my dissertation committee. Their valuable suggestions and comments have helped to strengthen the dissertation.

Special thanks go out to my M. Sc advisor, Dr. Linda M. Wills, for her continued support during my study at Georgia Tech, ever since I was a master student. I also wish to thank my late advisor, Dr. Scott Wills, for all his helpful advice and guidance.

I would like to thank my colleagues in the Sensors and Smart Systems Lab, including Hengzhao Yang, Xiangmin Wei, Zhenhua Xie, Ruizhi Chai, Zongyang Xia, Fan Liu, Geng Sun, Xukai Ding, Zhen Liu and all others. It has been a pleasure to work with such talented and hardworking colleagues. I want to thank them for all the discussions and contributions to my research. I am also grateful to my friends, Cen Lin, Sen Yang, Shiyang Chen, Yunlong Cai and many others. Thank you for all the help and support. I will always remember the good time we spent together.

I owe a debt of gratitude to my family, especially my parents, for all their unwavering support. Their endless love inspires, empowers and encourages me to set out on the adventure of pursuing a doctoral degree in Georgia Tech.

Most of all, I wish to thank my wife Yanming. It is her support and encouragement that helps me overcome all the difficulty. Yanming, I could never have done this far without your support.

TABLE OF CONTENTS

LIST OF TABLES

LIST OF FIGURES

LIST OF ABBREVIATIONS

ADC	Analog-to-Digital Converter
AS	Approximated Search
BS	Base Station
CH	Cluster Head
CM	Cluster Member
CSMA/CA	Carrier Sense Multiple Access with Collision Avoidance
D-PEA	Deviation-aware Predictive Energy Allocation
DSSS	Direct Sequence Spread Spectrum
DVFS	Dynamic Voltage Frequency Scaling
ENO	Energy Neutral Operation
ES	Exhausted Search
ETPC	Energy efficient Transmission Power Controller
FDMA	Frequency Division Multiple Access
HaEA	Harvesting-aware Energy Allocation
IC	Integrated Circuits
IoT	Internet of Things
IoBT	Internet of Battery-less Things
JCTO	Joint Computation and Transmission Optimization
LDP	Latency-aware Data Partition
LRIC	Lexicographic Rate for IoBT Cluster
MCU	Micro Control Unit
MOSFET	Metal-Oxide-Semiconductor Field-Effect Transistor
MPPT	Maximum Power Point Tracking
NVRAM	Non-Volatile Random Access Memory
PER	Packet Error Rate

PF	Progressive Filling
PPM	Predictive Power Management
PRR	Packet Receive Rate
PV	Photovoltaic
QPSK	Quadrature Phase Shift Keying
QoS	Quality of Service
RF	Radio Frequency
RSSI	Received Signal Strength Index
SC	Supercapacitor
SNR	Signal to Noise Ratio
SoC	State of Charge
TDMA	Time Division Multiple Access
VLR	Variant Leakage Resistor
WCMA	Weather Conditioned Moving Average
WSN	Wireless Sensor Network

SUMMARY

With the proliferation of Internet of Things (IoT) and IoT related services, how to power such a gigantic number of IoT systems in a cost-efficient and environment-friendly way becomes a bottleneck problem. Empowered by energy harvesting technologies and extremely long cycle life of the energy storage device Supercapacitors (SC), Internet of Battery-less Things (IoBT) is a promising solution with prolonged lifetime and self-sustainable operation. The objective of the thesis is to develop power management strategies for IoBT.

Energy efficient operation of IoBT systems has been investigated at both the node- and network-levels. At the node level, a power manager is first developed to minimize the internal energy loss of the energy storage device SC. In particular, a charge redistribution-aware power manager is developed to minimize the SC charge redistribution loss and improve the overall energy efficiency of an energy harvesting IoBT system. The SC charge redistribution occurs due to the unbalanced voltages of the SC internal RC branches. The specialized power manager balances the SC internal voltages by dispatching the workload in an eager way. Evaluated using the real-world solar energy profiles, the redistribution-aware power manger reduces the SC redistribution loss by 71% compared with other existing approaches. Then, a Predictive Power Management (PPM) framework is developed to enable energy efficient operation of each IoBT system. In the PPM framework, based on the developed IoBT system model, an optimal working point in terms of the SC terminal voltage is derived to minimize the IoBT system power loss. To maintain the SC terminal voltage at the optimal working point in an environment with varying ambient energy harvesting opportunities, Deviation aware Predictive Energy Allocation (D-PEA) is proposed to track the SC terminal voltage and adjust the energy allocation process accordingly. Moreover, Energy efficient Transmission Power Controller (ETPC) is investigated to achieve energy efficient wireless transmission over the varying wireless channel quality. PPM is shown to outperform the state-of-the-art power managers with 15% of system power loss reduction

and 20% of improvement in the energy efficiency of wireless transmission.

At the network-level, an adaptive clustering framework is developed to achieve high and fair data collection for IoBT networks. To fully utilize the harvested energy, the IoBT cluster follows the lexicographic rate assignment to dynamically derive the transmission rate based on the ambient energy generation. An approximation-based Cluster Head (CH) selection scheme is investigated to achieve similar data collection rate as that of the optimal CH selection algorithm at a much lower computational cost. The IoBT-specialized adaptive clustering framework is validated to be effective in providing high and fair data collection rate with low communication and computation overhead. Compared with the existing strategies, the proposed adaptive clustering framework enables up to 43% higher data collection rate. Moreover, a collaborative in-network processing framework is developed to minimize the data processing latency for IoBT networks. A latency-aware data partition algorithm is designed to split the input data into small-sized segments and dispatch the data segments to the IoBT nodes. By iteratively optimizing the data partition, MCU frequency and transmit power of each IoBT nodes, the collaborative in-network processing framework minimizes the overall latency. Extensive simulation results have proven the effectiveness of the collaborative in-network processing framework with a 30% reduction in the processing latency compared with the existing methods.

In summary, the power management schemes proposed in the thesis provide a holistic resource management framework for IoBT.

CHAPTER 1
INTRODUCTION

As an enabling technology for the fifth generation (5G) mobile communication networks [1], Internet of Things (IoT) brings revolutionary changes into both academia [2] and industry [3]. It is estimated that the total number of IoT will reach 20 billion by the end of 2020. How to power such a large number of IoT systems in a low-cost and environment-friendly manner becomes a major concern. Due to the limited capacity, batteries provide constrained lifetime. The depletion of batteries is inevitable and will incur huge amount of cost for battery replacement and recycling. It is desirable to have IoT systems that are self-sustainable and maintenance-free with renewable energy sources.

1.1 Background and Motivation

With the advances in energy harvesting technologies and low power electronics, various types of ambient energy have been utilized to provide IoT with prolonged lifetime, such as solar energy [4], Radio Frequency (RF) energy [5, 6] and human kinetic energy [7, 8]. This kind of energy harvesting low-power IoT is referred to as Internet of Battery-less Things (IoBT) in the proposal. Empowered by regenerable energy, IoBT is suitable for a plethora of future Smart X applications (such as Smart Home [9], Smart Grid [10] and so on) that require dense deployment of environment-friendly and cost-efficient wireless networks.

Compared with the conventional battery-operated IoT, IoBT presents new challenges in the following aspects:

(1) **Dynamic energy source:** The energy supply of IoBT system is subject to the time-varying ambient environment. The dynamic ambient energy generation casts adverse effect on the operation of IoBT. IoBT is expected to be aware of the energy variation and adaptively adjust the workload to maintain a balance between the harvested power and system

load power. Harvesting-aware energy allocation algorithms need to be developed to achieve prolonged lifetime over the varying energy sources.

(2) **Energy efficient operation:** Considerable amount of energy is dissipated during the operation of IoBT systems. Due to the efficiency loss incurred by the energy storage devices and voltage converters, the usable energy is precious. To improve the energy efficiency for IoBT, it is desired to design specialized power management to minimize the IoBT system power loss.

(3) **Collaborative IoBT networks:** As ultra-densification is one of the main features of 5G wireless networks, it is desired for multiple IoBT systems to work collaboratively for a variety of applications, such as data collection, in-network processing and so on. Different from the conventional battery-operated wireless networks, the IoBT network requires the overall network operation to be adaptive to the ambient energy generation. Network-level resource management needs to be developed by taking into account of the network architecture and ambient energy generation. Moreover, the computation and control message overhead is required to be minimized due to the restrained hardware and energy resources.

The major goal of the research is to provide a systematic power management framework from node-level to network-level for IoBT. To be specific, the major focus of this thesis is on Supercapacitor (SC)-operated IoBT due to the extreme long cycle life and simplified interface circuit. Holistic power management strategies are provided from node-level to network-level and enable high Quality of Service (QoS) of IoBT.

1.2 Related Work

Energy efficiency has long been a popular research topic in wireless networks. In comparison, research on IoBT has only recently started gaining attention. In this chapter, a brief overview of the related work is provided in the following topics: (1) IoBT systems; (2) node-level power management; (3) network-level power management.

1.2.1 IoBT Systems

IoBT is developed based on the conventional energy harvesting networked systems. This thesis focuses on SC-operated IoBT system equipped with a low-power wireless communication module (wireless transceiver) and computation unit (MCU). In this section, the major innovations and features of IoBT systems will be presented.

1.2.1.1 Energy Storage Device

Due to the versatility of ambient energy sources, energy storage devices are essential in energy harvesting systems. Rechargeable batteries are widely adopted in the conventional energy harvesting systems to store the harvested energy [4, 11, 12]. Despite the high energy density, conventional rechargeable batteries have limited cycle life. For example, a NiMH rechargeable battery has typical cycle life ranging from 500 to 1000 discharge/charge cycles [13]. Once the cycle life is used up, rechargeable batteries will experience severe degradation incurred by the loss of capacity and increase of the internal resistance, which makes them unsuitable for long-term energy harvesting applications.

Supercapacitor (SC) has much longer cycle life, which can reach up to 500,000 cycles [14]. There is a growing trend to adopt SC as the energy buffer in many recent IoBT systems [15, 16, 17, 18, 19, 20]. However, SC has higher internal dissipation rate compared with rechargeable batteries. The 24-hour energy dissipation rate of an SC is about 5.9% [14], while the self-discharge rate for a NiMH rechargeable is less than 1%. It is also demonstrated in [21, 22] that in addition to the self-discharge power (also known as the SC leakage power [19]), the SC charge redistribution loss is correlated to the workload dispatch pattern.

Moreover, SC has much lower energy density compared with the conventional rechargeable battery. With a limited capacity of energy storage device, maintaining a stable Quality of Service (QoS) over the variation of the ambient energy generation becomes a challenge. It is desired to design an SC-specialized power manager to mitigate the SC internal energy

loss and improve the energy efficiency.

1.2.1.2 Voltage Regulator

The terminal voltage of SC varies from $0\,\mathrm{V}$ to the nominal voltage (usually $2.7\,\mathrm{V}$ for a single SC). A voltage regulator is required to output a stable voltage to power the system [23]. Due to the imperfect voltage regulation circuit, efficiency loss is inevitable. Through the experimental measurement, Wang *et al.* [24] report that the energy dissipated by the voltage regulator reaches up to 30% of the total energy consumption for a solar-powered IoBT system.

According to the previous study [25], the voltage conversion efficiency is affected by both the regulator hardware and system workload (The system workload decides the load power consumption). Therefore, IoBT-specialized power managers need to take into account the power loss of the voltage regulation while determining control strategies to better utilize the harvested energy.

1.2.2 Node-level Power Management

For energy harvesting systems, harvesting-aware power management is critical due to the variation of ambient energy generation. A typical node-level power manager is a combination of the following parts: (1) harvesting-aware energy allocation; and (2) harvesting-aware power modulation.

1.2.2.1 Harvesting-aware Energy Allocation

Harvesting-aware Energy Allocation (HaEA) [26] usually follows the idea of "budgeting and allocating" to balance the energy expenditure and the energy harvesting. It first estimates the usable energy of the system and then allocates the energy according to the hardware and application specifications. To fully utilize the allocated energy, adaptive duty cycling [11, 27, 28] is used in the energy allocation stage to scale the system power con-

sumption by turning on/off the hardware according to the energy budget. Energy Neutral Operation (ENO) [12] is reached once the energy consumption is matched to the ambient energy generation.

The existing HaEA strategies can be categorized into two main types: non-predictive and predictive. Non-predictive schemes [19, 29] assign workload based on the remaining energy of the storage device, without any requirement of priori information about future energy harvesting. They have low computational cost. However, due to a conservative workload assignment, low energy utilization is common. The state-of-the-art non-predictive energy allocation algorithm, the low bound based scheme [29], is proven to be an asymptotically optimal energy allocation algorithm in long term operation. It requires a sufficiently large energy storage device to buffer the unutilized energy, which makes it unsuitable for IoBT with small energy buffer.

Thanks to the energy harvesting predictors [30, 31, 32], predictive energy allocation is developed to envision and pre-allocate the future incoming energy. Compared with non-predictive allocation algorithms, predictive energy allocation algorithms [33, 34] enable higher energy spending rate but at the same time, incur more power failure risk. With the assumption of deterministic harvesting profile, Progress Filling [33] achieves perfect energy utilization and optimal temporal fairness in energy allocation. In real world deployment, energy predictors are error-prone and their fidelity is affected by many factors, such as temperature, shadowing and so on. When the predictor over-predicts the future energy generating rate, predictive allocation algorithms will assign a high energy spending rate, which potentially leads to power failure of the system. For IoBT systems with limited size of energy storage device, a transient over-prediction error will very likely drain the remaining energy of the SC and thus lead to power failure.

It still remains a problem how to enable high energy utilization and at the same time, buffer the prediction errors for IoBT systems. Previous energy allocation algorithms may have compromised performance if being directly applied to IoBT systems.

1.2.2.2 Harvesting-aware Power Modulation

With the development of low power electronics, modern Integrated Circuits (IC) provide multiple power modes so that dynamic power modulation is enabled. Power modulation techniques provide agility and robustness to maintain energy efficient operation over the ambient energy variation.

Micro Control Unit (MCU) is responsible for data processing and system control tasks. Its power consumption is associated with the supply voltage and clock frequency [35]. A lower frequency helps to save energy but at the same time, increases the task execution time. Harvesting-Aware Dynamic Voltage Frequency Scaling (HA-DVFS) based power manager [36, 37, 38] dynamically assigns the MCU frequency to maintain the ENO condition while respecting the real-time requirements.

Compared with MCU, wireless transceiver consumes more power due to the uncertainty of the wireless channel quality. For example, a TI MSP430 MCU consumes about $150\,\mu\mathrm{W/MHz}$, while a TI CC 2500 transceiver has minimum active power consumption of about $20\,\mathrm{mW}$. Wireless transmission power controller [39, 40, 41, 42] is desired to enable energy efficient wireless transmission for IoBT systems. Set-point based controllers are mainly used to maintain a constant Received Signal Strength Index (RSSI) [43, 44] or Packet Received Rate (PRR) [45] at the receiver side. In the existing transmission power control schemes, the choice of the set-point (RSSI or PRR) remains empirical. For IoBT systems, the power dissipation of the voltage regulator needs to be taken into consideration when selecting an optimal transmission power. It is unclear whether set-point-based transmission power control techniques still achieve optimal energy efficiency.

1.2.3 Network-level Power Management

Based on the node-level power management, network-level power management strategies [34, 46, 47, 48] are designed to facilitate energy harvesting networks. A network-level energy harvesting power manager needs to comprehensively consider the network topology,

energy harvesting variation and application requirements to properly assign resources for each node.

1.2.3.1 Adaptive Transmission Rate

For wireless networks, a fair transmission rate is desired to achieve steady network operation and prolonged lifetime [49, 50]. In order to achieve this goal, lexicographic rate allocation is proposed for the energy harvesting networks [51]. Yang *et al.* [52] further improve the lexicographic rate allocation to a fully distributed algorithm.

The existing lexicographic rate assignment approaches are designed for the flat topology. Data aggregation [53] is not considered. Consequently, the node placed close to the Base Station (BS) is responsible for relaying data from the far-away nodes, which limits the overall network throughput due to the disparity in energy consumption. Moreover, the problem is exaggerated with a densely deployed network due to a heavy load of data relaying.

Compared with the flat topology, adaptive clustering [54, 55, 56] has been proven to be an energy efficient data collection framework with the help of data aggregation schemes [53]. For each clustered network, a Cluster Head (CH) is elected to collect data from the Cluster Member (CM), perform data aggregation and then forward the information back to the BS. However, the existing adaptive clustering strategies [57, 58] use a fixed data collection rate to extend the network lifetime, which will compromise the overall energy utilization for IoBT. It is desired to design a network-level power management framework to enable high and fair data collection for clustered IoBT networks.

1.2.3.2 In-network Processing

With the voluminous amounts of data being produced in the big data era, in-network processing becomes an important topic for networked systems. Typically, in-network processing related research focuses on two aspects: (1) where to process the data; and (2)

how to optimize the computation (MCU frequency) and communication (transmit power) resources.

Initially, client-server architecture was proposed for the conventional battery-operated Wireless Sensor Networks (WSNs). Due to the limited usable energy and insufficient computational power of the end devices, cloud server becomes an ideal host for resource-hungry applications [59]. Considering the fact that public clouds, such as Amazon EC2 and Microsoft Azure, are usually faraway from the end devices, the data exchange between the end devices and servers incurs high energy and timing overhead. Rather than utilizing the remote public servers, the cloudlet based mobile cloud computing framework [60] leverages the physical locality by deploying a designated server/cluster via one-hop access to the end devices. However, due to the space limitation, a nearby server may not provide sufficient resources for a large number of of end devices. The queueing delay can be magnified when every end device requests a task offloading to the server.

More recently, a more flexible paradigm, mobile edge computing, is proposed to make dynamic offload decision to depend on the available computing and energy resources from both the end device and the server sides. Xu *et al.* proposes a game theory based optimization framework to fully utilize the wireless bandwidth for efficient offloading [61]. Mao *et al.* uses Lyapunov optimization to develop effective online offloading strategy [62].

The existing mobile edge computing literature [61, 62] assumes that the end devices are running independent and small-sized tasks. Due to the fact that most end devices are restrained with limited energy and computational capacity, this assumption is valid. However, with the rapid growth of the data generated by IoT devices, it is desired for IoBT networks to process tasks with relatively larger data size with high QoS.

To fully utilize the computational capability of IoBT networks, collaborative in-network processing partitions a task into multiple segments so that each IoBT node can process a segment of data simultaneously to reduce latency. This idea is originated from the field of parallel and distributed computing [63], in which researchers mainly utilize multiple

homogeneous servers to collaboratively process data. These servers usually have similar hardware resources and are co-located in a same data center. The input data can be equally partitioned and then assigned to each of these servers. For IoBT networks, even with the same hardware configuration, each IoBT node displays significant heterogeneity due to the difference with energy harvesting [34]. Moreover, wireless channel has time-varying quality that further increases the disparity. The inherent heterogeneity of IoBT networks makes it non-trivial to achieve efficient collaborative processing. Equal partition may not achieve high performance for IoBT networks. A specialized collaborative in-network processing framework is desired to achieve minimized latency for IoBT networks.

1.3 Research Objective and Main Contribution

From the discussion of the existing literature, the runtime performance of IoBT systems remains problematic. It is desired to investigate power management strategies for IoBT systems to achieve sustainable and autonomous operations.

In this thesis, node- and network-level power managers are proposed for IoBT systems and IoBT networks. The proposed frameworks are adaptive to the ambient energy variation and at the same time, achieves high QoS.

This thesis presents the following contributions.

1) A charge redistribution aware power manager is designed to minimize the SC charge redistribution loss. An SC simulator is developed to study the SC redistribution loss in long term energy harvesting systems. With specialized task scheduling policy, the redistribution-aware power manager is shown to be effective in keeping accumulated charge redistribution loss low in long term operation. Compared with the existing power manager, the redistribution-aware power management reduces the redistribution loss by 71%.

2) A Predictive Power Management (PPM) framework is proposed. PPM combines optimal working point, Deviation aware Predictive Energy Allocation (D-PEA) and Energy efficient Transmission Power Control (ETPC) for IoBT systems. PPM is capable of min-

imizing the system power failure and achieve high energy utilization. Compared with the previous power managers, PPM incurs about 15% reduction in system power loss.

3) A clustered data collection strategy is proposed for IoBT networks, consisting of lexicographic rate assignment and optimal Cluster Head (CH) selection. Extensive simulations show that the proposed method achieves high and fair data collection rate for IoBT networks. Compared with the existing schemes, the proposed method enables up to 43% higher data collection rate and at the same time, incurs low computational overhead.

4) A collaborative in-network processing framework is developed for IoBT networks. A Latency-aware Data Partition (LDP) algorithm is designed to split the task data into small-sized segments and then dispatch the segments to the IoBT nodes. Then, a Joint Computation and Transmission Optimization (JCTO) algorithm is designed to further reduce the task latency by selecting the optimal MCU frequency and transmit power for each IoBT node. By iteratively performing LTP and JCTO, the proposed framework minimizes the overall in-network processing latency for IoBT networks. Compared with the existing approaches, the proposed framework reduces the in-network processing latency by 30%.

1.4 Organization of the Thesis

The rest of the thesis is organized as follows. Chapter 2 presents the charge redistribution aware power manager. Chapter 3 details the predictive power management strategy. Chapter 4 illustrates the clustered data collection mechanism. Chapter 5 develops the collaborative in-network processing framework. Finally, Chapter 6 concludes the thesis.

CHAPTER 2

CHARGE REDISTRIBUTION-AWARE POWER MANAGEMENT

Due to the versatility of the ambient energy generation, energy storage devices are essential for the energy harvesting systems. Supercapacitors (SCs) are considered to be promising energy storage devices due to the extremely long cycle life which can reach up to 500,000 cycles. However, SCs have much higher internal energy dissipation compared with the conventional rechargeable batteries. It is desired to design customized power managers to mitigate the internal energy loss of SCs and improve the energy efficiency of the SC-operated energy harvesting systems.

The rest of this chapter is organized as follows. Section 2.1 discusses the SC simulator. Section 2.2 presents the sensor node model and analyzes the redistribution loss in SC-operated sensor nodes. The charge redistribution aware power management is proposed in Section 2.3. The proposed method is evaluated in simulations with real world energy harvesting profiles in Section 2.4. Section 2.5 concludes the chapter.

2.1 Supercapacitor Simulator

2.1.1 Variant Leakage Resistor (VLR) based SC simulator

The SC simulator implemented in [64] is used to investigate charge redistribution loss. The simulator is based on the VLR model, which has been experimentally validated [65, 66]. As illustrated in Figure 2.1, the VLR model features two RC branches, instant branch with variant capacitor C_1 and delayed branch with constant capacitor C_2. The instant branch has a smaller time constant than that of the delayed branch. Charge redistribution happens when the voltages across C_1 and C_2 (V_{C_1} and V_{C_2}) do not balance. When the redistribution current goes through R_1 and R_2, the overall redistribution power is the sum of P_{R_1} and P_{R_2},

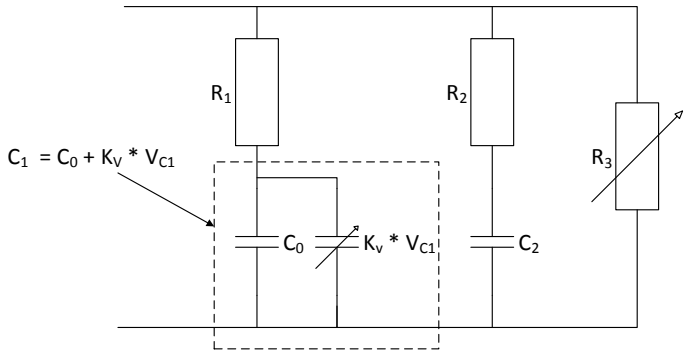

Figure 2.1: Supercapacitor VLR model [64]

as shown in Equation (2.1). Because of the small value of R_1 ($0.067\,\Omega$ for a $10\,\mathrm{F}$ Maxwell SC), V_{C_1} is approximated by the SC terminal voltage V_{SC} if the charging/discharging current is within a limited range (less than $1\,\mathrm{A}$), shown in Equation (2.2). The SC simulator can update the terminal voltage V_{SC} as well as the internal State of Charge (SoC), including the internal voltages V_{C_1}, V_{C_2} and charge redistribution power P_{chd}. The input of the simulator is charging/discharging profiles and initial SoC of the SC.

$$P_{chd} = P_{R_1} + P_{R_2} = \frac{(V_{sc} - V_{C_1})^2}{R_1} + \frac{(V_{sc} - V_{C_2})^2}{R_2} \tag{2.1}$$

$$P_{chd} \approx \frac{(V_{C_1} - V_{C_2})^2}{R_2} \tag{2.2}$$

2.1.2 Validation of the SC simulator

Though the VLR model has been previously verified by experiments [65, 66], the SC simulator uses approximation steps in implementation: (1) the capacitance of the voltage dependent capacitor C_1 is fixed in one time slot (assuming the time step of the simulator is small enough for the approximation [64]); (2) the internal SoC V_{C_1} and V_{C_2} are updated in a sequential way to reduce computation while in real cases V_{C_1} and V_{C_2} are evolving simultaneously. The fidelity of the simulator needs to be verified.

The simulator is validated from two aspects: (1) Whether the simulator can predict the

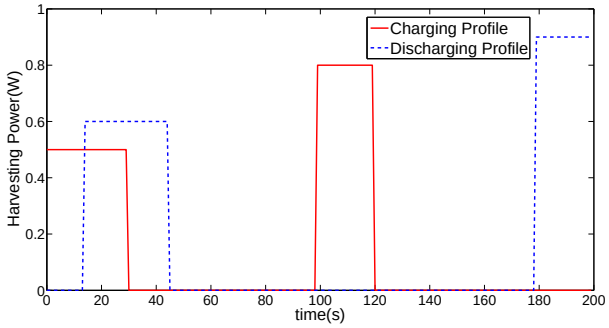

Figure 2.2: Charging and discharging profile of the first test case

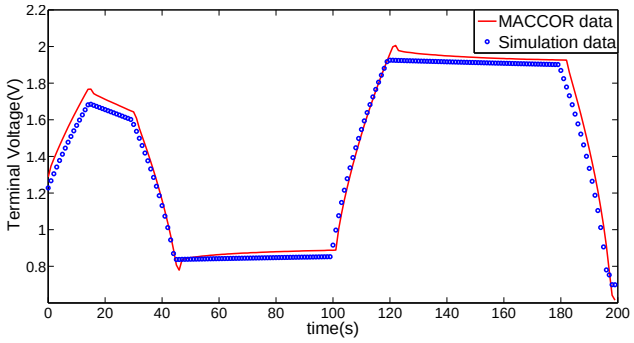

Figure 2.3: Terminal voltage comparison of the first test case

SC terminal voltage with high fidelity; (2) Whether the simulator can correctly analyze the redistribution loss.

The first aspect is tested using a dynamic testing experiment on a Maxwell $10\,\mathrm{F}$ SC. In this experiment, twenty charging and discharging profiles are randomly generated (Figure 2.2 shows the charging/discharging profile of the first test), and the terminal voltage predicted by the SC simulator is compared with the experimental measurements with the same charging/discharging profiles (Figure 2.3 is the comparison result of the first test). The experiments are performed using a MACCOR model 4304 testing system [67]. The averaged errors of the twenty test cases are shown in Figure 2.4. The results indicate that the terminal voltage predicted by the simulator matches well with the measurement of the MACCOR tester. The averaged error of the simulator ranges from 0.92% to 7.25%.

The second aspect is verified by a long term charge redistribution test. The SC simulator uses the terminal voltage V_{SC} to recurrently update the internal SoC of SCs [64]. The

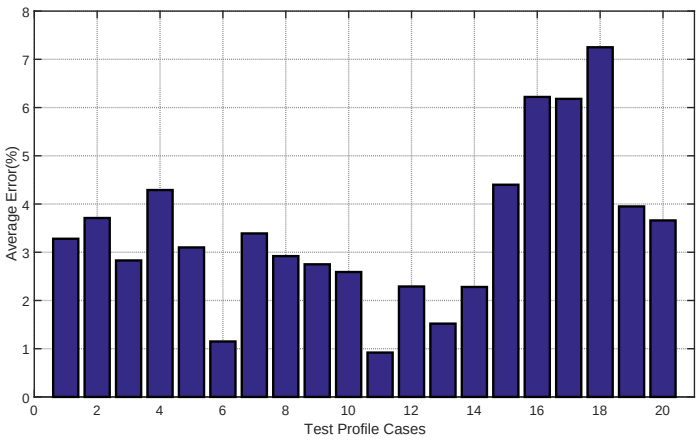

Figure 2.4: Average prediction error of the SC simulator for twenty randomly generated charging/discharging profiles.

redistribution loss P_{chd} is caused by the unbalanced internal voltage $|V_{C_1} - V_{C_2}|$. Thus accurate prediction of SC terminal voltage validated by the first set of experiments guarantees high fidelity of the internal SoC status, which eventually contributes to the effectiveness of long term redistribution analysis. To further verify the capability of long term redistribution loss test, two charging/discharging profiles (Cases 1 and 2) are used to compare the accumulated charge redistribution loss from the SC simulator and experiments. Both cases contain one hour of periodic pulse-wised charging and discharging profiles with a period of $100\,\mathrm{s}$. The charging/discharging pulse has a width of $10\,\mathrm{s}$, and an amplitude of $1\,\mathrm{W}$. The discharging pulses are always arranged at the end of the period. The location of charging pulse is different for case 1 and 2. The charging pulse of case 1 always starts at the beginning of a period while the starting time in case 2 is randomly generated within a period. For each test case, the SC simulator provides the accumulated charge redistribution loss based on Equation (2.2), and the MACCOR tester is used for experimental comparison. Since the MACCOR system only records the SC terminal voltage under the same charging/discharging profiles, the numerical method in previous literature [22] is used to extract the SC SoC (V_{C_1}, V_{C_2} and P_{chd}) iteratively from the terminal voltage recordings. The total redistribution loss calculated from the MACCOR testing is considered as the ground truth. Table 2.1 shows the results of the long term charge redistribution test. The total

Table 2.1: Validation of charge redistribution loss

	Charge redistribution Loss(J)	
	MACCOR test	VLR based simulator
Case 1	1.064	1.095
Case 2	3.663	3.458

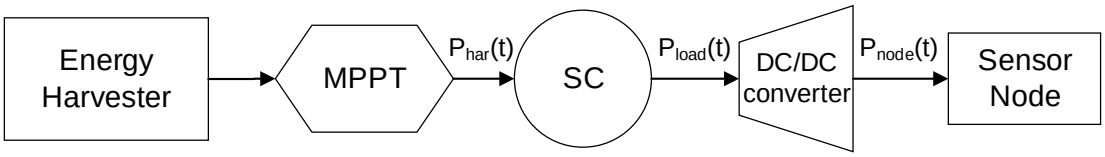

Figure 2.5: SC-operated energy harvesting system model

charge redistribution loss from the simulator is close to the ground truth. The accumulated errors of the one-hour redistribution analysis for case 1 and case 2 are 2.91% and 5.60%, respectively.

2.2 Redistribution loss in SC-operated Sensor Nodes

2.2.1 Simplified SC-operated sensor node model

To evaluate the impact of charge redistribution loss in SC-operated sensor nodes, a simplified SC-operated sensor node system model is built. A typical energy harvesting sensor node includes the components shown in Figure 2.5. An energy harvester is used to convert the ambient energy to electrical energy. The harvested power is regulated through Maximum Power Point Tracking (MPPT) interface and replenish the energy storage device, SC, at the rate of $P_{har}(t)$. The simplified model only captures the replenishment of SC, i.e. energy harvesting profile, without worrying about the type of energy harvester and the associated MPPT. A DC-DC converter is used to boost the SC voltage to a stable output to support the sensor node.

The energy harvesting profile is simplified as a periodic function, and the harvested power is composed of one pulse within each period T, as described in Equation (2.3). t_d and P_{pulse} refer to the duration and the amplitude of the pulse, respectively. *phase* denotes

the time when the harvesting pulse will arrive in the period. The average harvested power $\overline{P}_{har}$ is derived based on Equation (2.3).

$$P_{pulse}t_d = \overline{P}_{har}T \tag{2.3}$$

The sensor node workload is composed of periodic tasks. The average power $\overline{P}_{node}$ of the sensor node is controlled by its duty cycle D, as shown in Equation (2.4). P_{sleep} and P_{active} refer to the power consumption at the sleep mode and active mode, respectively. P_{active} is related to the type of workload and the power consumption of the hardware that the task incurs, such as transmitting and receiving RF message, sensor reading, Analog-to-Digital Converter (ADC) sampling and so on. D changes the ratio between active time and sleep time to balance the sensor node power with the harvested power. Equation (2.5) derives the sensor node power consumption. t_{sch} defines the time when the node starts to dispatch the task in the period. t_{ex} stands for the execution time of the task.

$$\overline{P}_{node} = P_{active}D + (1-D)P_{sleep} \quad (0 \leq D \leq 1) \tag{2.4}$$

$$P_{node}(t) = \begin{cases} 0, & 0 \leq V_{SC} < 0.85 \\ P_{active}(t), & (0.85 \leq V_{SC} \leq V_{nom})\ and \\ & (0 \leq t - kT_{node} - t_{sch} \leq t_{ex}) \\ P_{sleep}, & otherwise \end{cases} \tag{2.5}$$

For an SC, the terminal voltage ranges from $0\,\mathrm{V}$ to the nominal voltage V_{nom} (V_{nom} is usually $2.7\,\mathrm{V}$ or $2.5\,\mathrm{V}$ for a single SC). A DC-DC converter is needed to boost the SC terminal voltage to a stable value required by the sensor node. Previous literatures [34, 68] indicate that the efficiency of the widely used commercial DC-DCs does not vary significantly with the input voltage within the range of $0\,\mathrm{V}$ to $2.7\,\mathrm{V}$ if the output power is fixed (The variation is usually within 6%.). However, when the output power of the DC-

DC is low, for example, in the sleep mode, due to the converter power consumption, the efficiency drops compared with that in active mode with high output power. Based on the TPS6122X DC-DC boost converter [69] feature, the efficiency η of the regulator is defined as Equation (2.6), and the required input power to the DC-DC converter is determined by Equation (2.7), in which $0.85\,\mathrm{V}$ is start up threshold. The SC simulator implemented in this subsection is used to capture the SC behavior.

$$\eta = \begin{cases} 75\%, & if\ P_{node} = P_{sleep} \\ 88\%, & if\ P_{node} = P_{active} \end{cases} \tag{2.6}$$

$$P_{load} = \begin{cases} 0, & 0 \leq V_{SC} < 0.85 \\ \frac{P_{node}}{\eta}, & 0.85 \leq V_{SC} \leq V_{nom} \end{cases} \tag{2.7}$$

2.2.2 Charge redistribution analysis in SC-operated Sensor Nodes

By using the SC-operated sensor model, extensive experiments are conducted to study the charge redistribution behavior in the long term energy harvesting applications. The emulated sensor node is assumed to work under the ENO condition, which is a common condition in energy harvesting sensor networks [5, 12, 44, 64, 70] and can be described by the following equation.

$$\overline{P}_{har} \approx \overline{P}_{load} \approx \frac{\overline{P}_{node}}{\eta} \tag{2.8}$$

Three experiments are conducted to investigate the effects of three potential factors on SC charge redistribution loss: SC terminal voltage, charging/discharging power profiles and task scheduling policy. The Maxwell $10\,\mathrm{F}$ SC in Subsection 2.1 is used in the simulation. In order to minimize the impact of random errors, all three experiments are repeated for 50 times and the results shown in this section are the average values.

The first experiment focuses on the impact of V_{SC} on the charge redistribution loss.

Table 2.2: Charge redistribution loss with different V_{SC}

Terminal Voltage(V)	Charge redistribution Loss(J)
1.0	622.143
1.2	623.612
1.5	627.232

Table 2.3: Charge redistribution loss with different P_{har}

P_{har}(W)	$P_{node}(W)$	Charge redistribution Loss(J)
1.0	0.88	625.366
0.8	0.704	463.886
0.6	0.528	311.957

Under the ENO condition, the terminal voltage of the SC does not fluctuate rapidly. By setting different initial SC terminal voltage, the effect of the terminal voltage on charge redistribution is studied. Three test cases are designed with same workload, task scheduling policy, but different terminal voltage as listed in Table 2.2. The test time is one week. The results in Table 2.2 demonstrate that charge redistribution is irrelevant to the SC terminal voltage. This is different from self-discharge characteristics of SCs, which decreases as the terminal voltage decreases [5, 19].

The second experiment focuses on the impact of charging power P_{har} and discharging power P_{node} on the charge redistribution loss. Due to the ENO condition in Equation (2.8), P_{har} and P_{node} are scaled proportionally to investigate how charging and discharging power affects redistribution loss. The test time is also one week. The results in Table 2.3 reveal that larger charging and discharging power leads to more severe distribution loss. Since SC charge redistribution is caused by the transient voltage difference between the internal instant branch and delayed branch, higher charging and discharging power aggravates the voltage difference and leads to more redistribution loss.

The third experiment is designed to quantify the effect of different task scheduling policies on redistribution loss. Three task scheduling policies are investigated: greedy scheduling, lazy scheduling and eager scheduling. Greedy scheduling schedules the tasks at the beginning of the period, shown in Equation (2.9). Lazy scheduling delays the tasks until the

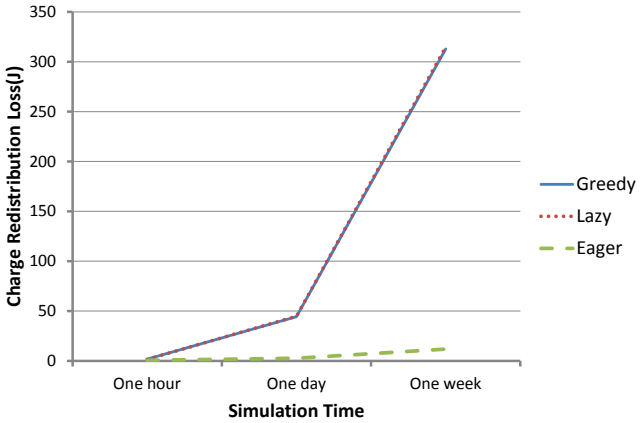

Figure 2.6: Charge redistribution analysis for different task scheduling policy

deadline approaches, shown in Equation (2.10). In the simulation, the lazy scheduling sets the deadline as the end of the period. The eager scheduling schedules the tasks whenever there is enough energy, which means the tasks are always scheduled right after the charging pulse, indicated in Equation (2.11). The phase of the periodic charging pulse is a random number following a uniform distribution between $[0, T]$, where T is the period.

$$(t_{sch})_{greedy} = kT \tag{2.9}$$

$$(t_{sch})_{lazy} = kT - t_{ex} \tag{2.10}$$

$$(t_{sch})_{eager} = kT + phase + t_d \tag{2.11}$$

Figure 2.6 shows the simulation results of different scheduling algorithms. The charge redistribution loss for lazy scheduling and greedy scheduling overlaps well, especially in the long-term test cases. The eager scheduling has the smallest redistribution loss among the three scheduling policies. The charge redistribution loss of the lazy scheduling and the greedy scheduling reaches to $312\,\mathrm{J}$ in one week compared with $11\,\mathrm{J}$ of eager scheduling. The eager scheduling reduces about 96.5% of the redistribution loss. According to

the previous study [64], charge redistribution loss increases monotonically with the time difference between the harvesting pulse $phase$ and the task dispatch time t_{sch}, denoted as Δt, which is calculated by Equation (2.12). The expected values of Δt for different task scheduling policies are shown in Equation (2.13). For harvesting-aware WSNs, duty cycle value is usually small, i.e. $t_{ex} << T$. Therefore, the expected value of Δt is very close for the lazy scheduling and greedy scheduling, which explains why both scheduling policies have almost identical redistribution loss in Figure 2.6. For the eager scheduling, due to the fact that the duration between the charging pulse t_d and the task execution time t_{ex} is much smaller than the period T, thus the value of Δt is smaller leading to a much smaller redistribution loss than those of lazy scheduling and greedy scheduling.

$$\Delta t = |phase - t_{sch}| \tag{2.12}$$

$$\mathbb{E}(\Delta t) = \begin{cases} \frac{T}{2}, & if\ greedy\ scheduling \\ |\frac{T}{2} - t_{ex}|, & if\ lazy\ scheduling \\ t_d, & if\ eager\ scheduling \end{cases} \tag{2.13}$$

To better elaborate the reasons the scheduling policies have large impact on charge redistribution, a snap shot is made on the simulation process from $t = 500$ s to $t = 1000$ s. Previous results indicate that greedy scheduling and lazy scheduling have the same redistribution loss. Therefore, the comparison is made on the variation of SC internal SoC from lazy scheduling and eager scheduling. Figures 2.7 and 2.8 describe the detailed SoC status of lazy scheduling and eager scheduling, respectively. It is obvious that charging pulse leads to the increase of internal voltage difference $|V_{C_1} - V_{C_2}|$ for both policies. When the sensor node executes the task, the internal voltage difference is balanced. Comparing Figure 2.7.c with Figure 2.8.c, $|V_{C_1} - V_{C_2}|$ of the lazy scheduling is larger than that of the eager scheduling for most of the time. Large internal voltage difference brings high

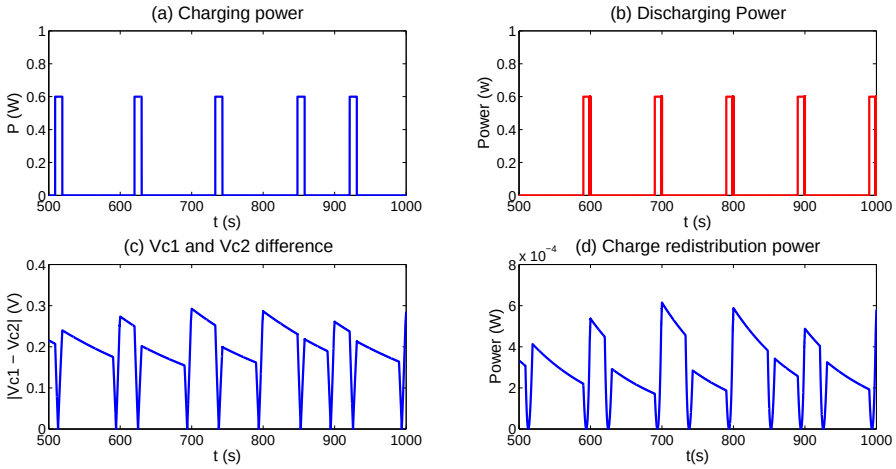

Figure 2.7: A snap shot of the lazy scheduling

redistribution loss, as shown in Equation (2.2). The results indicate that the total charge redistribution loss of lazy scheduling ($1.812\,\mathrm{J}$) is almost 3 times as that of from the eager scheduling ($0.612\,\mathrm{J}$) in one hour. The ratio keeps growing with longer test time, and reaches up to 28 times ($11\,\mathrm{J}$ for the eager scheduling versus $312J$ for the lazy scheduling) in one week.

Another observation lays in the necessity of charge redistribution-based power management. Though the instantaneous charge redistribution power P_{chd} is small, it always exists and thus can be accumulated to considerable amount of loss. For the one week case, the redistribution loss reduced by eager scheduling is about $300\,\mathrm{J}$. Based on the simulation setup ($P_{load} = 0.6\,\mathrm{W}$ and $D = 10\%$), the saved energy could support the node to operate for about 1.4 hours. Thus by cutting down charge redistribution loss, the sensor node can save considerable amount of energy to improve the overall energy efficiency.

2.3 Charge Redistribution aware Power management

Section 2.2 investigates the charge redistribution loss through extensive simulations. The eager scheduling is demonstrated to be effective in reducing charge redistribution. However, considering the randomness and intermittent features of harvesting profile, it remains a question when there will be sufficient incoming energy to execute the workloads. Further-

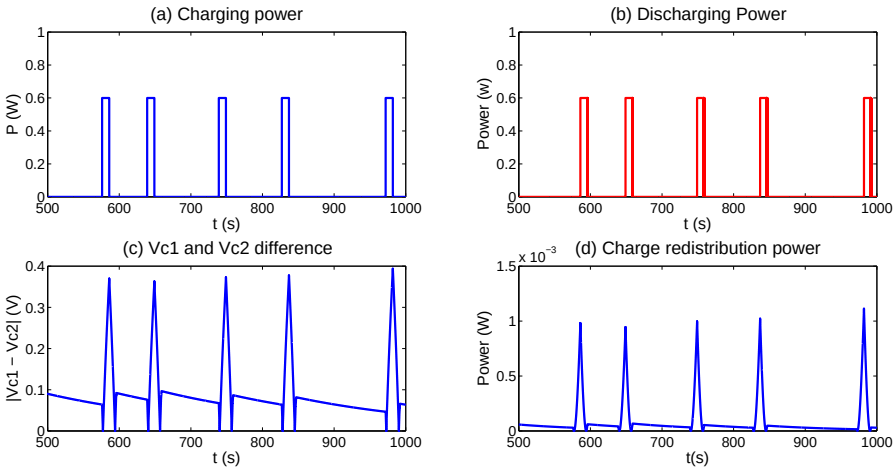

Figure 2.8: A snap shot of the eager scheduling

more, another problem lays in the workload which usually contains different kinds of tasks. More importantly, due to the hardware limitation, sensor node has restricted computational power and usable energy. The overhead of the power manager needs to be minimized. Consequently, the problem of how to efficiently dispatch the workload in a guaranteed eager way is still non-trivial. In this section, a redistribution-aware power management is proposed to reduce charge redistribution energy loss.

Assuming periodic workload contains M tasks in the task queue $\{Q_i, i = 1, 2, ..., M\}$, the first task resides in the head while the Mth (the last one) is in the tail. Each task Q_i is featured by five parameters $(P_i, t_{max_i}, t_{ex_i}, t_{sch_i}, d_i)$. P_i is the power consumption of the ith task. t_{max_i} stands for the maximum execution time restricted by the schedulability, as the Equation (2.14) indicates. t_{max_i} is application-specific. P_{max} is the maximum average power consumption when each task Q_i reaches maximum execution time t_{max_i}, shown in Equation (2.15). t_{ex_i} is the actual execution time of the ith task. t_{ex_i} is adjusted by the duty cycle D, shown in Equation (2.16). t_{sch_i} refers to the time that the ith task is dispatched, which is assigned by the task scheduler. d_i represents the deadline of the ith task. The end

of the period is considered as the deadline.

$$\sum_{i=1}^{M} t_{max_i} = T_{node} \tag{2.14}$$

$$P_{max} = \frac{\sum_{i=1}^{M} (t_{max_i} P_i)}{T_{node}} \tag{2.15}$$

$$t_{ex_i} = D t_{max_i} \tag{2.16}$$

2.3.1 Adaptive duty cycle controller

To respect the ENO condition, the well developed adaptive duty cycle controller [12, 19, 70] is adopted to keep a balance between the node energy consumption and the harvested energy. Algorithm 2.1 details the adaptive duty cycler. Once invoked, the controller measures terminal voltage V_{SC} using ADC and derives the usable remaining energy E_{use}. The software threshold V_{thd} is usually higher than the DC-DC start-up voltage to guarantee stable operation. Based on the duty cycle value D and self-discharge power P_{leak}, the controller is aware of the expected energy consumption E_{con}. By adjusting D with the step size D_{step}, E_{con} is adapted to E_{use}, as described from line 6 to line 15. Thus, the system is kept at ENO. P_{leak} is derived according to V_{SC} and the internal variant resistor R_3 based on the VLR model. The invocation interval of the duty cycle controller is set to be KT_{node}, where T_{node} is the period of the periodic workload. K is a constant depending on the variability of the ambient energy source.

The computational complexity of Algorithm 2.1 depends on the variation of the ambient available energy. μ denotes the average harvested energy variation rate, which calculated

from Equation (2.17). Algorithm 2.1 runs in $O(\frac{\mu}{D_{step}P_{max}})$ time on average.

$$\mu = \frac{1}{N}\sum_{i=1}^{N}\frac{\left|\int_{iT}^{(i+1)T} P_{har}(t)dt - \int_{(i-1)T}^{iT} P_{har}(t)dt\right|}{T} \tag{2.17}$$

Algorithm 2.1 Adaptive Duty Cycle Controller

Require: D, V_{thd}, D_{step}.
Get $V_{SC}(t)$ by ADC sampling;
$E_{use}(t) \leftarrow \frac{1}{2}CV_{SC}^2(t) - \frac{1}{2}CV_{thd}^2(t)$;
$P_{leak}(t) \leftarrow \frac{V_{SC}^2(t)}{R_3}$;
$E_{con}(t) \leftarrow DP_{max}KT_{node} + (1-D)P_{sleep}KT_{node} + P_{leak}(t)KT_{node}$;
if ($E_{con}(t) > E_{use}(t)$) **then**
  while ($E_{con}(t) > E_{use}(t)$) **do**
    $D \leftarrow D - D_{step}$;
    $E_{con}(t) \leftarrow DP_{max}KT_{node} + (1-D)P_{sleep}KT_{node} + P_{leak}KT_{node}$;
  end while
else
  while ($E_{con}(t) < E_{use}(t)$) **do**
    $D \leftarrow D + D_{step}$;
    $E_{con}(t) \leftarrow DP_{max}KT_{node} + (1-D)P_{sleep}KT_{node} + P_{leak}KT_{node}$;
  end while
end if

2.3.2 Charge redistribution aware task scheduler

A charge redistribution-aware task scheduler is proposed to reduce charge redistribution loss by dispatching tasks in an eager way. The objective of the redistribution-aware task scheduler is to execute tasks as soon as there is enough energy. Also, due to the requirement that the scheduler is invoked every period T_{node}, the overhead of the scheduler needs to be as low as possible.

Since the adaptive duty cycle controller guarantees the ENO condition, D is used to indicate the energy harvesting rate. The estimated harvested power $\hat{P}_{har}$ is derived from Equation (2.18). $\hat{P}_{har}$ is thus utilized to speculate when there will be sufficient harvested

energy for Q_i in the future.

$$\hat{P}_{har} \approx \overline{P}_{node} = P_{max}D + (1 - D)P_{sleep} \tag{2.18}$$

Algorithm 2.2 details the proposed task scheduler. Based on $\hat{P}_{har}$, the scheduler estimates when the incoming harvested energy will be enough for each task Q_i and thus derives the dispatch time t_{sch_i} for task Q_i. Algorithm 2.2 runs in $O(M)$ time (recall that M is the total number of tasks in the workload). The scheduler is invoked once every T_{node} and the calculation is simple. It meets the design requirements of eager scheduling and low overhead.

Algorithm 2.2 Charge redistribution aware task scheduler

1: **Require:** $\{Q_i, i = 1, 2, ...M\}$, P_{max}, D.
2: **for** $i = 1$ to M **do**
3: Update t_{ex_i} based on Equation (2.16);
4: **end for**
5: Update $\hat{P}_{hat}$ based on Equation (2.18);
6: **for** $i = 1$ to M **do**
7: **if** $(i == 1)$ **then**
8: $t_{sch_i} \leftarrow \frac{P_i t_{ex_i}}{\hat{P}_{har}}$;
9: **else**
10: $t_{sch_i} \leftarrow t_{sch_{i-1}} + t_{ex_{i-1}} + \frac{P_i t_{ex_i}}{\hat{P}_{har}}$;
11: **end if**
12: **end for**

2.3.3 Redistribution aware power management framework

Algorithm 2.3 details the overall framework of the redistribution-aware power manager. The adaptive duty cycler is invoked every KT_{node} to adapt the sensor node power consumption to the harvested power by updating D. The task scheduler is invoked at the beginning of every period to eagerly assign task dispatch time t_{sch} to all the tasks by speculating the future harvested power $\hat{P}_{har}$.

However, there might be cases when the actual harvested power deviates significantly from the speculation $\hat{P}_{har}$. For solar energy, the harvesting profile changes rapidly at morn-

ing and dusk. Weather condition can also possibly lead to the fluctuation of the harvested power. If the actual harvested power P_{har} is significantly smaller than the estimated value $\hat{P}_{har}$, at time t_{sch_i}, it is very likely that the system lacks enough energy for the task Q_i. Thus in Algorithm 2.3, the scheduler delays the task Q_i when there is insufficient energy. The $\hat{P}_{har}$ is updated by the instantaneous usable energy $E_{use}(t)$ (line 21 in Algorithm 2.3). The delay time t_{delay} is derived based on the amount of the energy shortage and the updated $\hat{P}_{har}$ (line 22 in Algorithm 2.3). In this way, when there is energy shortage, the task is delayed and the anticipated harvested power $\hat{P}_{har}$ is updated.

For cases when harvested power P_{har} increases significantly during the duty cycler invocation interval, the surplus energy is buffered in the SC for future usage.

The computational complexity of the overall redistribution-aware power manager (Algorithm 2.3) is $O(max\{M, \frac{\mu}{KD_{step}P_{max}}\})$. Under the same system configurations (keeping the same duty cycler resolution D_{step}, Algorithm 2.1 invocation interval K, workload size M and maximum system power P_{max}), when the ambient energy changes drastically, Algorithm 2.1 takes more execution time. On the other hand, when ambient energy is smooth, Algorithm 2.2 becomes critical.

2.4 Performance Evaluation

A series of simulations are performed to evaluate the effectiveness of the redistribution-aware power management. The objective is to test the effectiveness of the proposed power manager in reducing charge redistribution loss. The simulation uses the real world energy harvesting profile [71] and practical configuration to conduct the simulations. The proposed methodology is compared with other power manager which is not specialized for charge redistribution.

Algorithm 2.3 Redistribution Aware Power Management

Initialization:
  $D \leftarrow D_0$;
  task index $j \leftarrow 1$;
while (t) **do**
  if (t mod $KT_{node} == 0$) **then**
    Invoke the duty cycle controller (Alg. 2.1);
  end if
  if (t mod $T_{node} == 0$) **then**
    Initialize the task queue$\{Q_i, i = 1, 2, ...M\}$;
    Invoke the redistribution aware scheduler (Alg. 2.2);
    $j \leftarrow 1$;
  end if
  if (t mode $T_{node} == t_{sch_j}$) **then**
    Get $V_{SC}(t)$ by ADC reading;
    $E_{use}(t) \leftarrow \frac{1}{2}CV_{SC}^2(t) - \frac{1}{2}CV_{thd}^2$;
    $E_{task_j} \leftarrow t_{ex_j}P_j$
    if ($E_{use}(t) \geq E_{task_j}$) **then**
      Dispatch Q_j;
      $j \leftarrow j + 1$;
    else
      $\hat{P}_{har} \leftarrow \frac{E_{use}(t)}{t_{sch_j}}$;
      $t_{delay} \leftarrow \frac{E_{task_j} - E_{use}(t)}{\hat{P}_{har}}$;
      for $i = j$ to M **do**
        $t_{sch_i} \leftarrow t_{sch_i} + t_{delay}$;
      end for
    end if
  end if
  $t \leftarrow t + t_{step}$;
end while

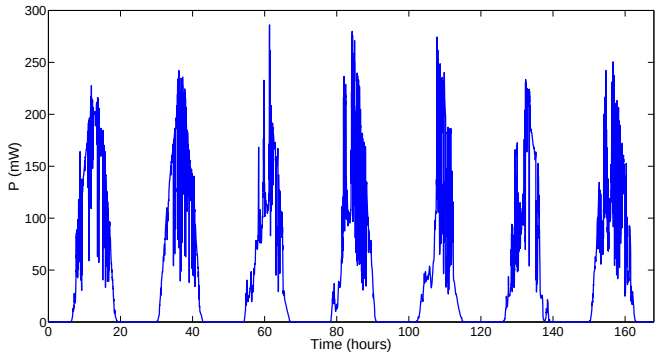

Figure 2.9: 7-day solar harvester profile

2.4.1 Simulation Setup

Solar energy is emulated to be the renewable energy source. Figure 2.9 shows the scaled solar power profiles for one week. The original solar irradiation profile is obtained from Oak Ridge National Lab from Sep. 1st 2014 to Sep. 7th 2014 [71]. Considering the limited physical size of a harvesting aware sensor node and efficiency loss in power transfer and power tracking, the solar trace is scaled. The data is recorded every minute.

An IRIS node is emulated as the sensor node model in the simulation. The node is equipped with a typical low power MCU Atmega $128L$ [72] and CC 2420 [73] as the radio transmission module. The simulated node is connected with a solar harvester. A single $10\,\mathrm{F}$ Maxwell SC is used as the energy buffer. The simulation considers a fixed configuration of the MCU frequency and RF transmission power to simplify the analysis. Considering the need for sensing, three sensors are added into the simulated sensor node, ranging from low power temperature sensor to high power flow control sensor [74]. The simulated sensor node only operates when there is solar energy available, which is approximately from 6:00 A.M. to 7:00 P.M. everyday. This is the same strategy adopted by many of the previous solar harvesting aware researches [34, 36].

The workload is simulated to be a pre-determined periodic task set containing 7 different tasks. The period T_{node} is set to be $100\,\mathrm{s}$. The power consumption P_i of each task is determined by the hardware component the task involves [74]. The deadline d_i is set

Table 2.4: Workload

$\{Q_i, i = 1, 2, ...7\}$	$P_i(mW)$	$t_{max_i}(s)$	Related hardware
Temperature sensing	0.7	12	temperature sensor
Flash read	20.46	4	Flash
MCU processing	26.4	32	Atmega 128L
Flash write	60.72	12	Flash
RF communication	72.6	8	CC 2420
Proximity sensing	420	16	TDA0161
Flow control	1250	16	FCS-GL1

to be the end of the period. Table 2.4 details each workload and its corresponding power consumption and maximum execution time. $\{Q_i, i = 1, 2, ...7\}$ is the work set which needs to be scheduled and dispatched.

2.4.2 Metrics and reference power manager

The SC terminal voltage value V_{SC} and the charge redistribution loss E_{chd} are recorded to evaluate the proposed and referenced methodologies. According to Equation (2.19), $V_{SC}(t)$ is representative of the remaining energy stored in the SC. E_{chd} is derived from Equation (2.20) based on the SC simulator. E_{chd} quantifies the effectiveness of the proposed methodology in terms of reducing recharge redistribution loss.

$$E_{rem}(t) = \frac{1}{2} C V_{SC}^2(t) \tag{2.19}$$

$$E_{chd} = \sum_{one\ week} P_{chd}(t) t_{step} \tag{2.20}$$

In order to evaluate the energy efficiency of the proposed redistribution-aware power management, an existing non-redistribution aware power manager is implemented for comparison. The non-distribution aware power manager uses the adaptive duty cycle controller (Algorithm 2.1) to respond to the variation of the harvesting profile. Due to the lack of redistribution-aware specialization, the task scheduler in the benchmark power manager

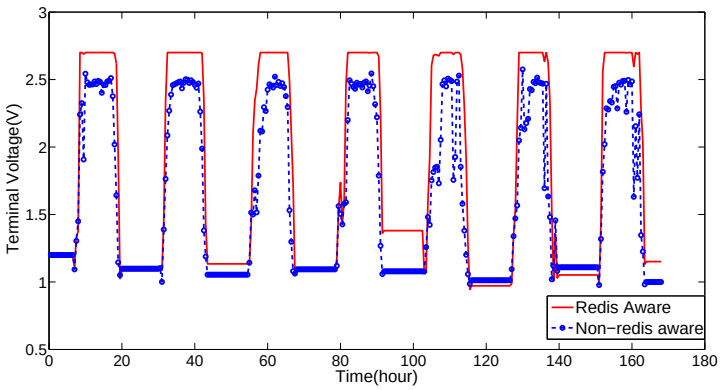

Figure 2.10: $\overline{V}_{SC}$ of a $10\,\mathrm{F}$ Maxwell SC

uses lazy scheduling [70]. The benchmark power manager has been demonstrated and validated in the previous literature [12, 19, 70] to be effective in maintaining ENO and thus is suitable for the comparison.

2.4.3 Results and discussions

Figure 2.10 visualizes the terminal voltage value $\overline{V}_{SC}$ of a $10\,\mathrm{F}$ SC. Due to the long testing time (one week), $\overline{V}_{SC}$ represents the remaining energy level. The $\overline{V}_{SC}$ value at each data point is the average of V_{SC} over a longer period (30 minutes). It shows that the $\overline{V}_{SC}$ values of the proposed methodology are higher than that of the benchmark power manager. The difference becomes more obvious during day time when there is more solar energy available. At night, due to the absence of solar energy, the simulated node is shutdown. Since both methodologies use the same adaptive duty cycler, harvesting profile and workload, the importance of the task scheduling policy is clearly demonstrated. The observation of Figure 2.10 is consistent with the conclusion in Subsection 2.2. At noon, $\overline{V}_{SC}$ of the proposed manager reaches to about $2.65\,\mathrm{V}$ while the average terminal voltage $\overline{V}_{SC}$ with the existing power manager is only $2.5\,\mathrm{V}$. In terms of the remaining energy, the proposed redistribution-aware power manager outperforms the non-redistribution aware power manager.

To further quantify the reduction in charge redistribution loss, Table 2.5 shows the total

Table 2.5: Charge redistribution loss

SC Size (F)	E_{chd} of proposed (J)	E_{chd} of benchmark (J)	Improvement
10	6.479	22.980	71.81%

charge redistribution loss E_{chd} for both methodologies. The proposed redistribution-aware power management reduces the redistribution loss by 71.81%. In one week operation, the proposed methodology can save about $16\,\mathrm{J}$ of charge redistribution loss. On average, the daily redistribution reduction is more than $2\,\mathrm{J}$, which explains the terminal voltage difference between the proposed manager and the benchmark manager.

2.5 Conclusion

In this chapter, an SC-operated energy harvesting sensor node model is presented, in which the SC simulator can capture the redistribution loss. Using the simulator, extensive investigation is conducted on the charge redistribution behavior of SC in an energy-harvesting wireless sensor node, and further study under what circumstances the redistribution power is high. The study shows that the task scheduling policy can make a big difference in terms of charge redistribution loss. The traditional state-of-the-art lazy scheduling is shown to be less optimal than eager scheduling in terms of charge redistribution loss. In order to reduce redistribution loss, a redistribution-aware power management framework is proposed for SC-operated energy harvesting nodes. The specialized power manager consists of an adaptive duty cycler and redistribution aware task scheduling policy that schedules the workload in an eager manner. The proposed power manager is tested using the real world solar profile and task workload. The long-term simulation results demonstrate that the redistribution-aware power manager has higher remaining energy level and less overall redistribution loss when compared with the non-redistribution aware power manager. The reduction of the redistribution loss is 71% for a $10\,\mathrm{F}$ Maxwell SC.

CHAPTER 3
PREDICTIVE POWER MANAGEMENT

In the previous chapter, a customized power manager is designed to reduce charge redistribution loss of the IoBT systems. In addition to the SC charge redistribution, there are other types of energy efficiency loss in IoBT systems, such as the energy dissipation incurred by the DC-DC regulator and wireless transceiver. There is a pressing demand for developing IoBT-specialized power management to enable energy efficient operation for IoBT systems.

The rest of the chapter is organized as follows. The IoBT system model is presented in Section 3.1. Section 3.2 details the proposed Predictive Power Management (PPM) framework. Section 3.3 uses the real-world solar profile to evaluate the proposed PPM framework. Section 3.4 concludes the chapter.

3.1 System Model

3.1.1 IoBT Hardware Model

Figure 3.1 is a typical IoBT system model, consisting of mainly four parts: (1) source unit, including an energy harvester and the corresponding Maximum Power Point Tracking (MPPT) charger; (2) energy storage unit; (3) interface unit; (4) functional unit, including Micro Control Unit (MCU), sensors and wireless transceiver.

An energy harvester is equipped to convert ambient energy to electric energy. This chapter considers the renewable energy source to be predictable (e.g., solar energy or wind energy). An MPPT charger connects the harvester to the energy storage device to stabilize the terminal voltage of the harvester at its Maximum Power Point. Based on the previous studies [75, 76, 77], the MPPT charger enables optimal power transfer from the energy

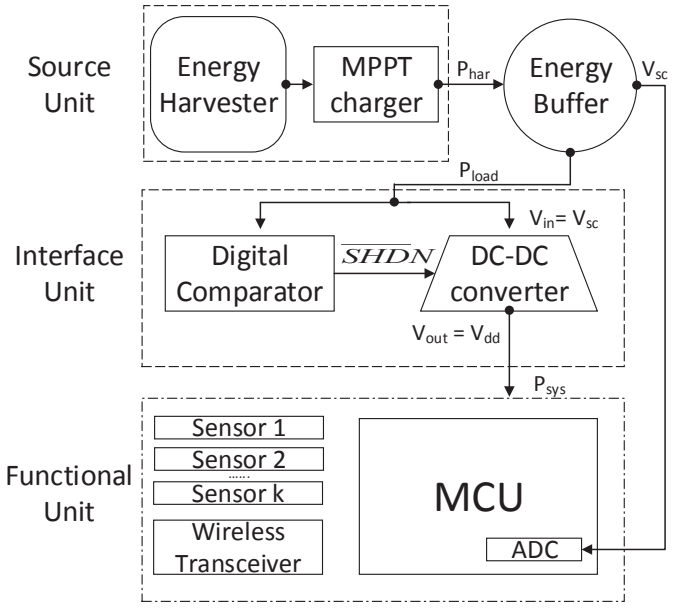

Figure 3.1: IoBT system model

harvester and at the same time, isolates the harvested power P_{har} from the energy buffer and the functional unit. With the MPPT charger, the harvested power P_{har} is proportional to the maximum power P_{mp}, shown in Equation (3.1). The tracking factor F_T is the ratio of the extracted harvested power through the MPPT charger versus the maximum power P_{mp}. Based on the previous study [76], the tracking factor F_T is dependent on the MPPT algorithms[1]. The maximum power P_{mp} depends on ambient environment. Taking Photovoltaic cell as an example, according to [76], the harvested power depends on light intensity and temperature.

$$P_{har} = F_T P_{mp} \tag{3.1}$$

In order to buffer the harvested energy, energy storage device is essential. A single SC is adopted as the energy storage device. The leakage power P_{leak} of the SC is characterized

[1]From [76], the tracking factor F_T ranges from 89% to 98% with different MPPT algorithms.

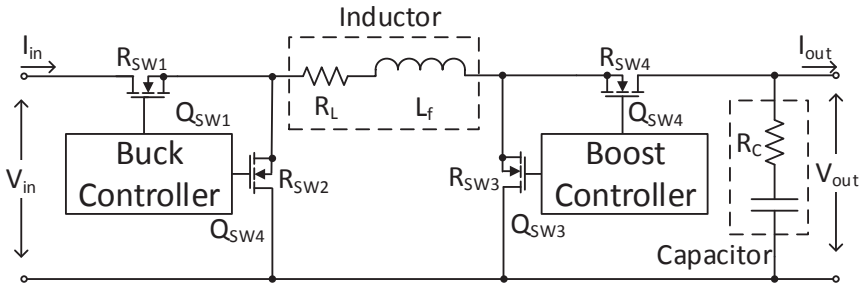

Figure 3.2: Buck-boost DC-DC converter model [25]

by the Variant Leakage Resistance (VLR) model [21, 78], as shown in Equation (3.2).

$$P_{leak} = \frac{V_{sc}^2}{R_{leak}} \tag{3.2}$$

Due to the variation of the SC terminal voltage V_{sc} from $0\,\mathrm{V}$ to the nominal voltage V_{nom} (usually $2.7\,\mathrm{V}$), a buck-boost DC-DC converter is necessary for regulating the output voltage V_{out} to reach V_{dd} (usually $1.8\,\mathrm{V}$ for low power electronics) to power the functional unit. The state-of-the-art uni-directional switching DC-DC converter model [25] is used to analyze the regulator energy loss, as shown in Figure 3.2. Equations (3.3) and (3.4) show the power consumptions of the buck mode ($V_{in} > V_{out}$) and the boost mode ($V_{thd} \leq V_{in} \leq V_{out}$), respectively. V_{thd} is the start-up threshold. A digital comparator is used to disable the voltage regulator when the SC terminal voltage V_{sc} drops below the threshold V_{thd}. I_{ctrl} is the current consumed by the internal buck/boost controller. H is the duty ratio, as shown in Equation (3.5). ΔI is the ripple current caused by the inductor L, as derived in Equation (3.6), where f_s is the switching frequency and L_f is the value of inductor L. R_L and R_C are the Equivalent Series Resistance (ESR) of the off-chip inductor L and capacitor C; R_{swi} and Q_{swi} refer to the turn-on resistance and gate charge of the i-th MOSFET switch, respectively. For both buck and boost cases, the DC-DC power consumption P_{dcdc} is a function of input voltage V_{in}, output voltage V_{out} and output current I_{out}, as shown in

Equation (3.7).

$$P_{buck} = I_{out}^2[R_L + HR_{SW1} + (1-H)R_{SW2} + R_{SW4}] + \frac{(\Delta I)^2}{12}[R_L + HR_{SW1} + (1-H)R_{SW2} + R_{SW4} + R_C] + V_{in}f_s(Q_{SW1} + Q_{SW2}) + V_{in}I_{ctrl} \tag{3.3}$$

$$\begin{aligned} P_{boost} = {} & \frac{I_{out}^2}{H^2}[R_L + HR_{SW4} + (1-H)R_{SW3} + R_{SW1} + H(1-H)R_C] \\ & + \frac{(\Delta I)^2}{12}[R_L + HR_{SW4} + (1-H)R_{SW3} + R_{SW1} + HR_C] \\ & + V_{out}f_s(Q_{SW3} + Q_{SW4}) + V_{in}I_{ctrl} \end{aligned} \tag{3.4}$$

$$H = \frac{min\{V_{in}, V_{out}\}}{max\{V_{in}, V_{out}\}} \tag{3.5}$$

$$\Delta I = \frac{(1-H)min\{V_{in}, V_{out}\}}{L_f f_s} \tag{3.6}$$

$$P_{dcdc} = f(V_{in}, V_{out}, I_{out}) \tag{3.7}$$

The efficiency of the DC-DC regulator, η, is defined as the ratio of the effective IoBT system power P_{sys} versus the overall load power P_{load}, as shown in Equation (3.8).

$$\eta = \frac{P_{sys}}{P_{load}} = \frac{V_{out}I_{out}}{P_{dcdc} + V_{out}I_{out}} \tag{3.8}$$

The previous literature [25] verifies the power model with two commercial DC-DC converters. In this part, another six off-the-shelf DC-DC converters from three different vendors (Linear Technology, Texas Instrument and Maxim Integrated) are used to further study the model fidelity. The DC-DC efficiency provided by the datasheets are used as the ground truth, denoted as η_{ds}. The efficiency estimated by the power model (referred to as

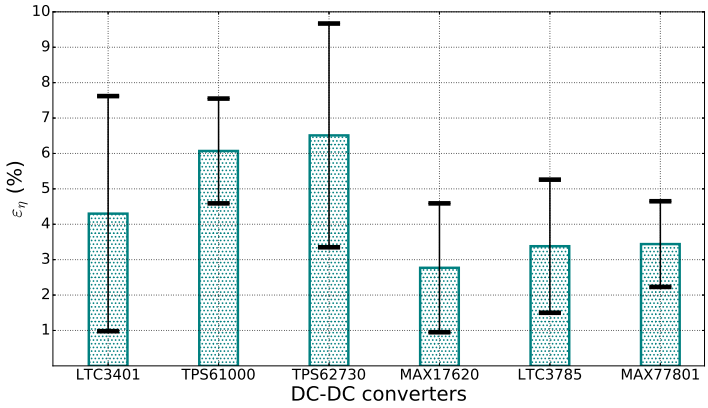

Figure 3.3: Distribution of the DC-DC efficiency estimation error ε_η

η_{em}) is compared with the ground truth. ε_η, defined in Equation (3.9), represents the error of the DC-DC efficiency estimation. The six commercial DC-DC converters are: TPS61000 [79], LTC3401 [80], TPS62730 [81], MAX17620 [82], LTC3785 [83] and MAX77801 [84]. The model parameters are extracted from the datasheets by adopting the approach introduced in [25]. Figure 3.3 illustrates the average and standard deviation of the error ratio of the converter efficiency model. The error ε_η ranges from 2.77% to 6.51% on average. Furthermore, Figure 3.4 demonstrates part of the efficiency comparison from MAX17620 and LTC3875. The efficiency estimated by the DC-DC power model matches well with the curve from the datasheets. Thus, the DC-DC power dissipation model is verified to be accurate in analyzing real DC-DC regulators.

$$\varepsilon_\eta = \frac{|\eta_{em} - \eta_{ds}|}{\eta_{ds}} \tag{3.9}$$

The MCU is responsible for the overall IoBT power management. With its on-chip Analog-to-Digital Converter (ADC), the MCU can measure the SC terminal voltage V_{sc} and thus calculate the remaining energy E_{rem}, as shown in Equation (3.10).

$$E_{rem} = \frac{1}{2} C V_{sc}^2 \tag{3.10}$$

IoBT system uses a wireless transceiver to exchange information. The transceiver has

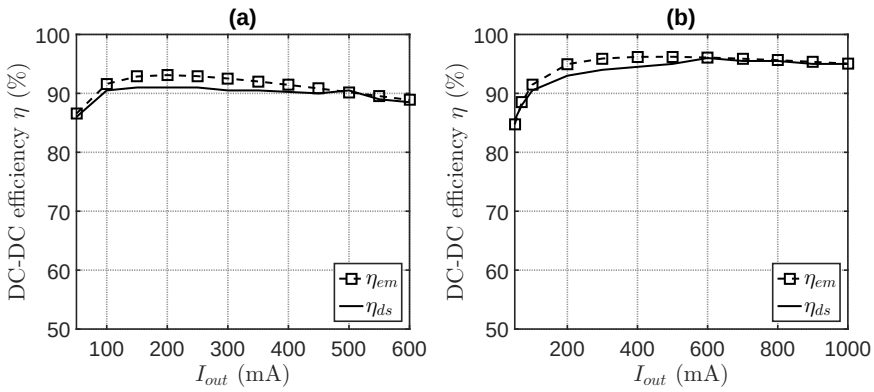

Figure 3.4: DC-DC converter efficiency validation: (a) MAX17620, $V_{in} = 2.7\,\mathrm{V}$, $V_{out} = 1.8\,\mathrm{V}$; (b) LTC3875, $V_{in} = 2.7\,\mathrm{V}$, $V_{out} = 5\,\mathrm{V}$

a list of available transmission power levels $\{P_{tk}\}$ and corresponding current consumption $\{I_{tk}\}$.

3.1.2 Wireless Link Model

The path-loss based model [85] is used to setup the wireless link. In radio propagation, the signal needs to overcome path loss to reach the receiver. Equation (3.11) shows the relationship between the received signal strength P_r and the transmission power P_t. The path loss PL is related to the distance between the sender and the receiver, d, and ambient environment (obstacles, transmission medium and etc).

$$P_r = P_t - PL(d) \tag{3.11}$$

At the receiver side, the wireless transceiver measures the received signal strength P_r by converting the RSSI register value into decibel based signal strength. Thus, the Signal to Noise Ratio (SNR) γ is expressed in Equation (3.12), where P_n is the noise strength which is usually measured when the wireless channel is idle. The receiver can piggy-back the RSSI value through the hand-shake packets. In this way, the sender can track the variation

of the path loss and select an efficient transmission power level.

$$\gamma = P_r - P_n \tag{3.12}$$

With each selected modulation scheme, the bit error rate is expressed as a function of SNR. Quadrature Phase Shift Keying (QPSK) is considered as the modulation scheme with Direct Sequence Spread Spectrum (DSSS). Equation (3.13) [86] derives the bit error rate ϵ_b. The $Q(\cdot)$ function is defined in Equation (3.14). $\left(\frac{E_b}{N_0}\right)_{DS}$ is a function of the energy per bit to noise spectral density $\frac{E_b}{N_0}$, representing the average received signal strength at the receiver, shown in Equation (3.15). N is the number of chips per bit and K is the number of simultaneously transmitting ends. Considering that 802.15.4 is a widely used wireless communication standard for IoBT systems, a collision avoidance medium access protocol, such as the state-of-the-art Carrier Sense Multiple Access with Collision Avoidance (CSMA/CA), is used to avoid multiple user contention. Thus, $K = 2$ in Equation (3.15).

$$\epsilon_b = Q\Big(\sqrt{(\frac{E_b}{N_0})_{DS}}\Big) \tag{3.13}$$

$$Q(x) = \frac{1}{\sqrt{2\pi}} \int_x^{\infty} e^{-\frac{u^2}{2}} du \tag{3.14}$$

$$\Big(\frac{E_b}{N_0}\Big)_{DS} = \frac{2N\frac{E_b}{N_0}}{N + \frac{4}{3}\frac{E_b}{N_0}(K-1)} \tag{3.15}$$

Based on the assumption that the bit errors are randomly and independently distributed, Equation (3.16) shows the packet error rate ϵ_p, where l is the packet size.

$$\epsilon_p = 1 - (1 - \epsilon_b)^l \tag{3.16}$$

When a packet is not acknowledged, the sender will resend the packet. The average

retransmissions of a packet, $\bar{k}$, is described in Equation (3.17).

$$\bar{k} = \sum_{i=1}^{\infty} i(1-\epsilon_p){\epsilon_p}^{i-1} = \frac{1}{1-\epsilon_p} \tag{3.17}$$

3.1.3 Power Consumption Model

In this chapter, IoBT systems are considered to adopt cyclic workload with period T. The power consumption is determined by both the power mode of the hardware (e.g. wireless transmission power) and the active operation time in that mode. Duty cycle D is defined to be the ratio of the active time t_{act} in a period, which is defined in Equation (3.18). By duty cycling, the load power consumption $\bar{P}_{load}$ is scaled, as indicated in Equation (3.19). P_{act} and P_{slp} are the active power and sleep power of the system, respectively. The active power consumption P_{act} is a variable subject to the wireless transmission power level, which will be determined by the wireless transmission control module in Subsection 3.2. η_{act} and η_{slp} are the regulator efficiency during the active mode and the sleep mode, respectively. The active power P_{act} is determined by the radio activity.

$$D = \frac{t_{act}}{T} \tag{3.18}$$

$$\bar{P}_{load} = D\frac{P_{act}}{\eta_{act}} + (1-D)\frac{P_{slp}}{\eta_{slp}} + P_{leak} \tag{3.19}$$

3.2 Predictive Power Manager for IoBT

In this subsection, a novel predictive power management framework is introduced. PPM contains three part: (1) optimal working point; (2) Deviation aware Predictive Energy Allocation (D-PEA), and (3) Energy efficient Transmission Power Control (ETPC).

3.2.1 Optimal Working Point

From the previous sections, the total power loss in IoBT system operation, P_{loss}, comes from two parts: DC-DC dissipation P_{dcdc} and SC leakage P_{leak}. The DC-DC power P_{dcdc} relates to the input voltage V_{sc}, the output voltage V_{dd} and the output current I_{out}. V_{dd} is a constant and I_{out} is task-specific. The SC leakage power P_{leak} is determined by the SC terminal voltage V_{sc}. To achieve energy efficient operation, an optimal working point V^* is desired to minimize the total power loss, as formulated in Equation (3.20).

$$\min_{V_{thd} \leq V_{sc} \leq V_{nom}} P_{loss} = (P_{dcdc} + P_{leak}) \tag{3.20}$$

To derive the optimal working point for IoBT systems, Lemma 3.1 and Lemma 3.2 are first presented, which are proven in Appendix A. Then, Lemmas 3.1 and 3.2 are used to further derive Theorem 3.1.

Lemma 3.1. In the buck mode ($V_{dd} < V_{sc} \leq V_{nom}$), the total power loss P_{loss} increases monotonically with the SC terminal voltage V_{sc}.

Lemma 3.2. In the boost mode ($V_{thd} \leq V_{sc} \leq V_{dd}$), the total power loss P_{loss} decreases monotonically with SC terminal voltage V_{sc}.

Theorem 3.1. For an IoBT system with a given supply voltage V_{dd} and SC nominal voltage V_{nom}, if $V_{nom} > V_{dd}$, then the overall system power loss P_{loss} achieves minimum value when $V^* = V_{dd}$.

If the SC nominal voltage V_{nom} is larger than the supply voltage V_{dd}, the working mode of the DC-DC converter depends on the SC terminal voltage V_{sc} (Recall that the SC terminal voltage ranges from $0\,\mathrm{V}$ to the nominal voltage V_{nom}). When $V_{dd} < V_{sc} \leq V_{nom}$, the DC-DC works at the buck mode. Based on Lemma 3.1, a low SC terminal voltage V_{sc} is preferred for reducing the system power loss. When $V_{thd} \leq V_{sc} \leq V_{dd}$, the DC-DC converter works in the boost mode. Lemma 3.2 indicates that a high SC terminal voltage improves the energy efficiency. Theorem 3.1 is proven by combining Lemma 3.1 and

Lemma 3.2. $V^* = V_{dd}$ is chosen as the optimal working point. Theorem 3.1 decouples the IoBT system power loss P_{loss} from the load current I_{out}. Thus, for arbitrary configuration of system workload, as long as the SC terminal voltage V_{sc} is maintained at the optimal working point V^*, the system power loss P_{loss} is minimized.

The optimal working point serves as a set-point for the online energy allocation algorithm. In real deployment, due to the variation of the ambient energy source, it is inevitable for the SC terminal voltage V_{sc} to deviate from the optimal point V^*. To achieve high energy efficiency, it is crucial for the power manager to minimize the voltage deviation.

3.2.2 Deviation-aware Predictive Energy Allocation (D-PEA)

In order to respond to the ambient energy variation, energy allocation algorithms adaptively assign workload in a cyclic manner, with a period of every kT ($k \geq 1$, recall that T is the period of the workload). Energy predictor is available to envision the future energy generation rate with invocation interval akT ($a \geq 1$). Considering that the energy predictors incur more computational cost than the lightweight energy allocation algorithms, the energy predictors are invoked with a longer period to reduce energy overhead (In previous literatures [11, 12, 34], predictors are usually evoked every 30, 60 minutes or even longer time while the invocation time of energy allocation algorithms range from 1 to 10 minutes.).

As demonstrated by the previous literatures [12, 34], online energy allocation algorithm enables ENO by matching the average system power consumption $\bar{P}_{load}$ to the average ambient energy generation rate $\bar{P}_{har}$, shown in Equation (3.21). Equation (3.22) explains the evolving process of the SC terminal voltage V_{sc} in an interval $[t_i, t_i + kT]$ ($t_i > 0$) with the average load power $\bar{P}_{load}$[2]. The SC terminal voltage is influenced by both charging power and system load power. $\bar{P}_{har}(t_i, t_i + kT)$ and $\bar{P}_{load}(t_i, t_i + kT)$ refer to the average harvested power and system load power in the invocation interval $[t_i, t_i + kT]$, respectively.

[2]Due to the overcharge protection, V_{sc} cannot exceed the SC nominal voltage V_{nom}. If V_{sc} drops below the threshold V_{thd}, the IoBT system will fail due to the shutdown of the DC-DC regulator.

By further looking into Equations (3.21) and (3.22), the following proposition is obtained.

$$\bar{P}_{har} \approx \bar{P}_{load} \tag{3.21}$$

$$\frac{1}{2}CV_{sc}^2(t_i + kT) = \frac{1}{2}CV_{sc}^2(t_i) + kT[\bar{P}_{har}(t_i, t_i + kT) - \bar{P}_{load}(t_i, t_i + kT)] \tag{3.22}$$

Proposition 3.1. For any $t_i > 0$, if the IoBT system operates under the ENO condition during the time interval $[t_i, t_i + kT]$, then $V_{sc}(t_i) \approx V_{sc}(t_i + kT)$.

Proposition 3.1 is proved by plugging Equation (3.21) into Equation (3.22). Proposition 3.1 shows that with the ENO condition, it is feasible to maintain a relatively stable SC terminal voltage at the runtime despite varying ambient energy generation. Thus, the optimal working point V^* can be used as a set-point in the energy allocation algorithm to maximize IoBT energy efficiency. Meanwhile, considering that system power failure is caused by depletion of the SC remaining energy to a point when the terminal voltage V_{sc} drops below the DC-DC start-up threshold V_{thd}, a stable SC terminal voltage V_{sc} can effectively reduce the system power failure time.

Due to the causality restriction, the future energy generation rate $\bar{P}_{har}$ is a priori unknown. Thus, PEA uses the future incoming energy prediction P_{pred} to derive the energy budget E_{bgt}, shown in Equation (3.23). V_s is the set-point value to derive the SC remaining energy[3]. $E_{bgt}(t_i, t_i + kT)$ refers to the assigned energy budget in the incoming interval $[t_i, t_i + kT]$ (Recall that PEA is triggered every kT), where t_i is arbitrary time that PEA is invoked for energy allocation. The average load power $\bar{P}_{load}$ is assigned based on Equation (3.24) so that the energy consumption equals to the energy budget. Note that E_{bgt} only includes the SC remaining energy above the set-point at the time t_i and the predicted energy in the next kT interval. The calculation of the energy budget E_{bgt} does not take

[3] Due to the restriction of the DC-DC start-up threshold and the SC nominal voltage, $V_s \in [V_{thd}, V_{nom}]$.

into account of the system loss. In the existing PEAs [4, 11, 12], the set-point V_s is set as low as possible (usually the DC-DC start-up threshold V_{thd} is used as the set-point V_s) to maximize the energy budget E_{bgt} because E_{bgt} quantifies the maximum energy that can be used in the next kT interval, as shown in Equation (3.24).

Based on the previous discussion in Subsection 3.2.1, the optimal working point $V^* = V_{dd}$ is significantly higher than the set-point V_s used in previous works. Equation (3.23) indicates that a higher set-point V_s seems to decrease the energy budget E_{bgt} in the interval $[t_i, t_i + kT]$. It remains unclear whether a high set-point value compromises the energy budgeting of PEA in the long term. This question is answered by Proposition 3.2.

$$E_{bgt}(t_i, t_i + kT) = \frac{1}{2}C[V_{sc}^2(t_i) - {V_s}^2] + kTP_{pred}(t_i, t_i + kT) \tag{3.23}$$

$$E_{bgt}(t_i, t_i + kT) = kT\bar{P}_{load}(t_i, t_i + kT) \tag{3.24}$$

Proposition 3.2. For any set-point value $V_1, V_2 \in [V_{thd}, V_{nom}]$ and $V_1 \neq V_2$, if the IoBT system uses predictive energy allocation, then there exists a finite time $t_s \in (0, +\infty)$, for any $t \geq t_s$, $E_{bgt}(t, t + kT)\big|_{V_s=V_1} = E_{bgt}(t, t + kT)\big|_{V_s=V_2}$.

Proof: For any $t_i \in (0, +\infty)$, Equation (3.25) is obtained by plugging Equation (3.24) into Equation (3.23).

$$kT\bar{P}_{load}(t_i, t_i + kT) = \frac{1}{2}C[V_{sc}^2(t_i) - {V_s}^2] + kTP_{pred}(t_i, t_i + kT) \tag{3.25}$$

Equation (3.26) is derived by combining Equations (3.22) and (3.25).

$$\frac{1}{2}C[V_{sc}^2(t_i + kT) - V_s^2] = kT[\bar{P}_{har}(t_i, t_i + kT) - P_{pred}(t_i, t_i + kT)] \tag{3.26}$$

Equation (3.27) shows the energy budget assigned by PEA in the interval of $[t_i+kT, t_i+$

$2kT]$ on the basis of Equation (3.23).

$$E_{bgt}(t_i + kT, t_i + 2kT) = \frac{1}{2}C[V_{sc}^2(t_i + kT) - {V_s}^2] + kTP_{pred}(t_i + kT, t_i + 2kT) \quad (3.27)$$

With Equations (3.26) and (3.27), the energy budget for the interval $[t_i + kT, t_i + 2kT]$ is derived:

$$\begin{aligned} E_{bgt}(t_i + kT, t_i + 2kT) = kT[&\bar{P}_{har}(t_i, t_i + kT) - P_{pred}(t_i, t_i + kT) \\ &+ P_{pred}(t_i + kT, t_i + 2kT)] \end{aligned} \quad (3.28)$$

Recall that the harvested power $\bar{P}_{har}$ and the energy prediction P_{pred} are independent of the set-value V_s. Thus, it is straight forward that $t_s = t_i + kT$, for any $t \geq t_s$, $E_{bgt}(t, t + kT)\big|_{V_s=V_1} = E_{bgt}(t, t + kT)\big|_{V_s=V_2}$. Proposition 3.2 is proved.

Proposition 3.2 demonstrates that after finite times of predictive energy allocation, the assigned energy budget E_{bgt} is actually irrelevant to the set-point V_s. This property indicates that a high set-point value, such as $V_s = V^*$, will not affect the long-term energy budgeting for PEAs.

During the energy allocation, the energy budget E_{bgt} is assigned to two parts: (1) energy that will be used by the functional unit, which is referred as E_{fun}; and (2) energy that will be dissipated by the SC leakage and the DC-DC regulator, which is referred as E_{dis}. Proposition 3.1 provides a feasible condition for IoBT systems to use the optimal working point V^* as the set-point to minimize the IoBT system power loss. Thus the dissipated energy E_{dis} is also minimized. Proposition 3.2 validates that for predictive energy allocation, using the optimal working point V^* as the set-point does not compromise the long term energy budget E_{bgt} compared to the state-of-the-art PEAs that use a much lower set-point V_s. By combining Propositions 3.1 and 3.2, it is guaranteed that the proposed online energy

allocation algorithm achieves better energy efficiency compared to the existing strategies [4, 11, 12].

Observation 3.1. For predictive energy allocation, the fluctuation of the SC terminal voltage is caused by the inaccuracy of the predictor.

Observation 3.1 is obtained by Equation (3.26). This observation demonstrates that by tracking the voltage deviation of the SC, the fidelity of the energy predictor can be inferred. A time-varying coefficient is added to adjust the weight for the energy predictor in the predictive energy allocation.

As detailed in Algorithm 3.1, the Deviation aware Predictive Energy Allocation (D-PEA) is derived on the basis of Proposition 3.1, Proposition 3.2 and Observation 3.1. D-PEA contains mainly two parts: (1) energy neutralization from line 12 to 24; (2) deviation-aware prediction weight adjustment from line 5 to 11.

The energy neutralization process is designed to respect the ENO condition. This method is widely adopted in previous energy harvesting systems [4, 12] and has been validated to be effective in maintaining the ENO condition by matching the load power to the harvested power. This approach is specialized with regard to the IoBT system model discussed in Subsection 3.1. The energy budget E_{bgt} calculated in line 12 is a combination of the remaining SC energy and prediction of future incoming energy, where $\rho(t)$ is a time-varying coefficient used to mitigate prediction errors. Justified by Proposition 3.1 and Proposition 3.2, the optimal working point V^* is used in line 12 of Algorithm 3.1 as a set-point for energy budgeting to achieve the minimum system power loss. As shown in line 13 of Algorithm 3.1, E_{con} represents the expected system energy consumption in the next kT interval, which is based on the IoBT power consumption model, including the power incurred by the wireless transceiver, DC-DC converter and SC leakage. P_t^* is the optimal wireless transmission power updated by the energy efficient transmission power control module, where I_t^* is the corresponding current consumption. After comparing the energy consumption E_{con} with the energy budget E_{bgt}, the duty cycle D is incremented

(line 15 to 18) or decremented (line 20 to 23) accordingly until E_{con} approximates E_{bgt}. In this way, the ENO condition is ensured and at the same time, the IoBT system operates with the most energy-efficient transmission power level.

Inspired by Observation 3.1, the deviation-aware prediction weight adjustment is used to mitigate the prediction errors. D-PEA keeps track of the voltage difference between the SC terminal voltage V_{sc} and the optimal working point V^*. A large deviation ($|V_{sc} - V^*|$ exceeds the threshold ζ) indicates that the predictor is either over-predicting or under-predicting. Thus, the coefficient ρ is incremented or decremented with a step size ρ_s (line $5 \sim 8$ in Algorithm 3.1). If the voltage deviation is small, then the coefficient ρ equals to the default value 1. The state-of-the-art PEAs [4, 11, 12] use static coefficient $\rho = 1$ in the predictive allocation. Once the predictor loses fidelity, the prediction error retains in the energy allocation module until the predictor recovers its accuracy. In this way, the conventional PEAs are more likely to suffer from the power failure caused by the error-prone harvesting predictors.

The time complexity of D-PEA is determined by the ambient energy variation and the duty cycle step size δ. Equation (3.29) defines μ to represent the average changing rate of harvested power, where n is the total time slots of the harvesting profile. Considering that the active transceiver power consumption $I_t^* V_{dd}$ is significantly larger than the sleep power P_{slp} and the SC leakage power P_{leak}, the Algorithm 3.1 runs in $O(\frac{\mu}{\delta I_t^* V_{dd}})$ on average.

$$\mu = \frac{1}{n} \sum_{i=1}^{n} [P_{har}(i+1) - P_{har}(i)] \tag{3.29}$$

3.2.3 Energy Efficient Transmission Power Control (ETPC)

D-PEA solves the problem of varying ambient energy source by predictively matching workload to ambient energy generation. Another problem is how to achieve energy efficient wireless communication. As stated in Section 3.1, it is desired to use dynamic wireless transmission power to optimize energy efficiency. Algorithm 3.2 describes Energy efficient

Algorithm 3.1 Deviation-aware Predictive Energy Allocation

1: **Require:** P_{pred}, ρ_s, V^*, ζ, P_t^*, I_t^*, δ.
2: $V_{sc} \leftarrow$ ADC measuring;
3: $P_{leak} \leftarrow$ Equation (3.2);
4: η_{slp} and $\eta_{act} \leftarrow$ Equation (3.8);
5: **if** $V_{sc} - V^* > \zeta$ **then**
6: $\quad \rho \leftarrow \rho + \rho_s$;
7: **else if** $V^* - V_{sc} > \zeta$ **then**
8: $\quad \rho \leftarrow \rho - \rho_s$;
9: **else**
10: $\quad \rho \leftarrow 1$
11: **end if**
12: $E_{bgt} \leftarrow \frac{1}{2}C[V_{sc}^2 - (V^*)^2] + \rho kTP_{pred}$;
13: $E_{con} \leftarrow D\frac{I_t^* V_{dd}}{\eta_{act}}kT + (1-D)\frac{P_{slp}}{\eta_{slp}}kT + P_{leak}kT$;
14: **if** ($E_{con} > E_{bgt}$) **then**
15: $\quad$ **while** ($E_{con} > E_{bgt}$) **and** ($D \geq \delta$) **do**
16: $\quad\quad D \leftarrow D - \delta$;
17: $\quad\quad E_{con} \leftarrow D\frac{I_t^* V_{dd}}{\eta_{act}}kT + (1-D)\frac{P_{slp}}{\eta_{slp}}kT + P_{leak}kT$;
18: $\quad$ **end while**
19: **else**
20: $\quad$ **while** ($E_{con} < E_{bgt}$) **and** ($D \leq 1 - \delta$) **do**
21: $\quad\quad D \leftarrow D + \delta$;
22: $\quad\quad E_{con} \leftarrow D\frac{I_t^* V_{dd}}{\eta_{act}}kT + (1-D)\frac{P_{slp}}{\eta_{slp}}kT + P_{leak}kT$;
23: $\quad$ **end while**
24: **end if**

Transmission Power Control (ETPC). The main objective of ETPC is to dynamically select an energy efficient transmission power level based on the wireless link quality.

ETPC updates the wireless link quality in a periodic manner. Once a connection is established, the receiver measures the RSSI value for the link every mT ($m \geq 1$) and piggy-backs it to the sender. According to the transceiver datasheets [87], the RSSI value can be converted into the received signal strength P_r through a linear equation, as shown in line 4 of Algorithm 3.2, where a and b are hardware related empirical values.

When the sender derives the signal strength P_r, the wireless path loss PL is inferred based on line 5 of Algorithm 3.2. Thus, a linear equation is established between the transmission power P_t and the SNR γ. In line 7 of Algorithm 3.2, ETPC uses the linear relation to estimate the SNR values for each available wireless transmission power level.

In order to find the optimal wireless transmission power, ETPC uses energy per useful received bit E_u to evaluate the energy efficiency of transmission power level P_t, where E_u is defined in Equation (3.30). I_t is the corresponding current consumption of the transceiver. When calculating the energy consumption of transmitting a packet, the DC-DC power consumption P_{dcdc} is taken into consideration (Recall that the SC leakage power P_{leak} is not affected by the load current I_{out}, which makes P_{leak} irrelevant to the wireless transmission power level. So the SC leakage power is excluded in the transmission power control module). According to Equation (3.7), P_{dcdc} is a function of the output current I_{out} and input voltage V_{in}. To select the transmission power with highest energy efficiency, ETPC uses an holistic approach by considering the overall IoBT system power consumption during wireless transmission.

The time complexity of Algorithm 3.2 is $O(M)$, where M is the number of programmable transmission power levels provided by the wireless transceiver.

$$E_u = \frac{(P_{dcdc} + I_t V_{dd})\frac{l}{R}\bar{k}}{l} = \frac{(P_{dcdc} + I_t V_{dd})\bar{k}}{R} \tag{3.30}$$

Algorithm 3.2 Energy efficient Transmission Power Control

1: **Require:** $\{P_{tk}\}$, $\{I_{tk}\}$, R, V_{dd}, a, b.
2: $V_{sc} \leftarrow$ ADC measuring;
3: $RSSI \leftarrow$ piggy-backed message from the receiver;
4: $P_r \leftarrow a \cdot RSSI + b$;
5: $PL \leftarrow P_t - P_r$;
6: **for** $P_{ti} \in \{P_{tk}\}$ **do**
7: $\quad \gamma_i \leftarrow P_{tk} - PL - P_n$;
8: $\quad \epsilon_{bi} \leftarrow Q(\sqrt{(\frac{E_b}{N_0})_{DS}})$;
9: $\quad \bar{k}_i \leftarrow \frac{1}{(1-\epsilon_{bi})^l}$;
10: $\quad E_{ui} \leftarrow \frac{\bar{k}_i}{R}(P_{dcdc} + I_{ti} V_{dd})$;
11: **end for**
12: $P_t^* = \min\{E_{uk}\}$;

3.3 Evaluation

A series of simulations are performed to evaluate the effectiveness of PPM. An IoBT system-based simulator is implemented in MATLAB. The emulated system uses a single SC as the energy storage device.

A $2.5\,\mathrm{cm}^2$ photovoltaic cell is used as the energy harvester. Its conversion efficiency is set to be 10%. The real world outdoor solar irradiance profile [71] from May. 1st 2015 to Aug. 31st 2015 is used to generate the harvested power. According to the previous literature [36, 75], the maximum solar power P_{mp} is proportional to the irradiance level, as shown in Equation (3.31). A is the size of the photovoltaic cell. G is the solar irradiance (W/m^2) from [71]. φ is the conversion efficiency, which stands for the percentage of the solar energy shining on a PV device that can be converted into usable electricity. The MPPT charger is assumed to use Perturb and Observe (P&O) algorithm and the tracking factor F_T is set to be 96.3% based on the experimental evaluation in [76].

$$P_{mp} = \varphi A G \tag{3.31}$$

3.3.1 Optimal Working Point

Figure 3.5[4] shows the variation of the overall IoBT system power loss P_{loss} with the SC terminal voltage V_{sc} and load current I_{out}. Figure 3.5(a) validates Lemma 3.1, Lemma 3.2 and Theorem 3.1. By stabilizing the SC terminal voltage V_{sc} close to $V^* = V_{dd}$, the IoBT energy loss is minimized. Figure 3.5(b) shows that, for higher output current I_{out}, the IoBT system has higher power loss P_{loss}.

[4]The parameters of the emulated regulator are extracted from [79, 81] with the output voltage $V_{dd} = 1.8\,\mathrm{V}$, the start-up threshold $V_{thd} = 0.9\,\mathrm{V}$ and the SC nominal voltage $V_{nom} = 2.7\,\mathrm{V}$.

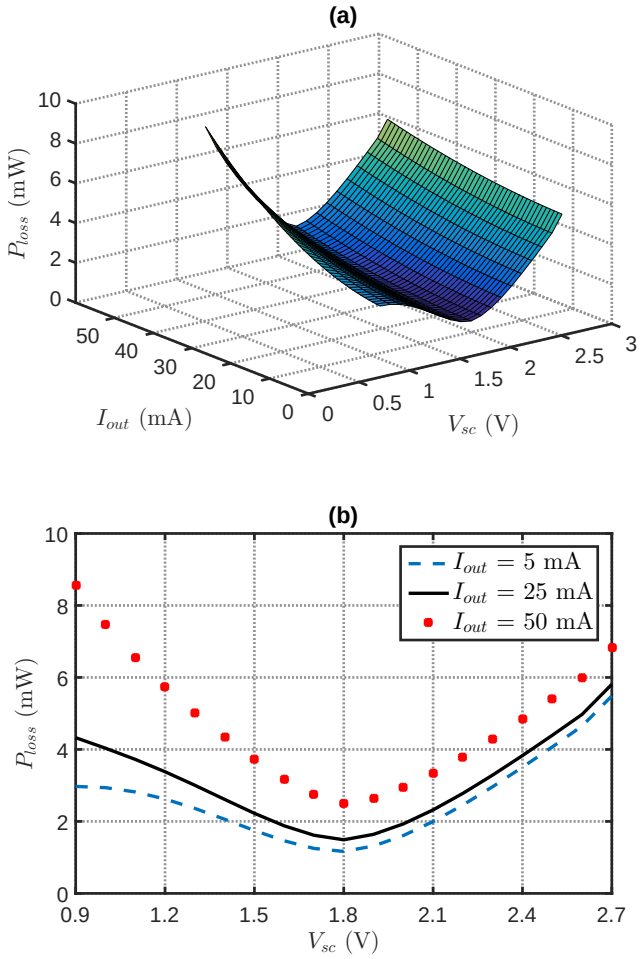

Figure 3.5: IoBT power loss P_{loss}: (a) P_{loss} with V_{sc} and I_{out}; (b) P_{loss} with load current I_{out} of $5\,\mathrm{mA}$, $25\,\mathrm{mA}$ and $50\,\mathrm{mA}$

3.3.2 Predictive Energy Allocation

In this subsection, the proposed D-PEA is evaluated. A well-established predictor, Weather Conditioned Moving Average[5] (WCMA) [30], is used to provide envision for future energy generation rate. Figure 3.6 demonstrates a sample of the solar power trace and the corresponding WCMA predictions. Three metrics are used to evaluate energy allocation algorithms: (1) energy utilization rate U; (2) system power failure time t_f; (3) IoBT system power loss P_{loss}. For comparison, several state-of-the-art energy allocation algorithms

[5]WCMA is a state-of-the-art solar energy predictor with capability of capturing both current and previous-day weather conditions. Please refer to [30] for the details of WCMA. In this part, the WCMA predictions were obtained using the following settings: $\alpha = 0.3$, $D_{day} = 4$, $K_{slot} = 3$.

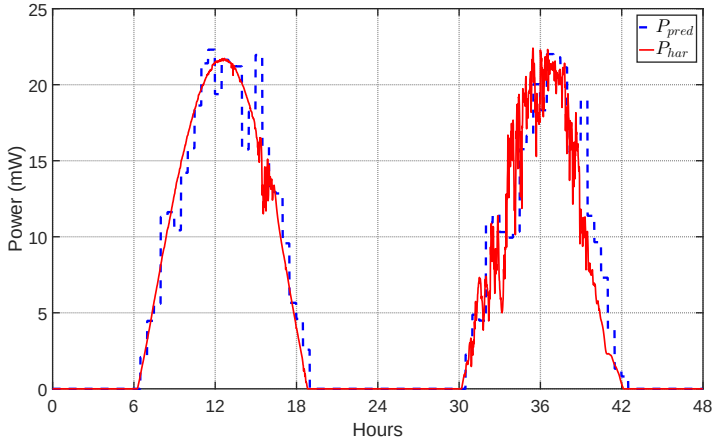

Figure 3.6: Solar power P_{har} and WCMA prediction P_{pred} for May. 15 and May. 16, 2015

are also implemented, including Progressive Filling (PF) [33], Lower-Bound based allocation [29] (referred to as *Scheme-LB*) and the state-of-the-art predictive energy allocation [4] (denoted by *sta-PEA*). These benchmark algorithms are not combined with wireless transmission control. To make a fair comparison, this subsection uses a fixed transmission power and the corresponding power consumption is $20\,\mathrm{mW}$.

$$U = \frac{\sum_{i=1}^{n} E_{con}(i)}{E_{init} + \sum_{i=1}^{n} E_{har}(i)} \tag{3.32}$$

The energy utilization rate U is defined to be the ratio between the total consumed energy E_{con} and the total energy (including the harvested energy E_{har} and the initial energy E_{init}) over all the simulation time slots, shown in Equation (3.32). A high energy utilization is desired for IoBT systems. Figure 3.7 shows the comparison of different energy budgeting algorithms in terms of utilization[6]. PF serves as an upper bound of the energy utilization as it reaches perfect utilization rate. PF is infeasible in real world applications due to the strict requirement of full knowledge of future energy generation. Scheme-LB has the lowest energy utilization rate. It follows a non-predictive energy allocation. To prevent over-draining the energy storage device, Scheme-LB always allocates a lower bound (the lower value between the current harvested power and the average harvested power) as the spending rate.

[6]The performance evaluation of D-PEA is obtained using the following parameters: $T = 100\,\mathrm{s}$, $a = 3$, $k = 6$, $\delta = 0.01$, $\rho_s = 0.1$, $\zeta = 0.3\,\mathrm{V}$.

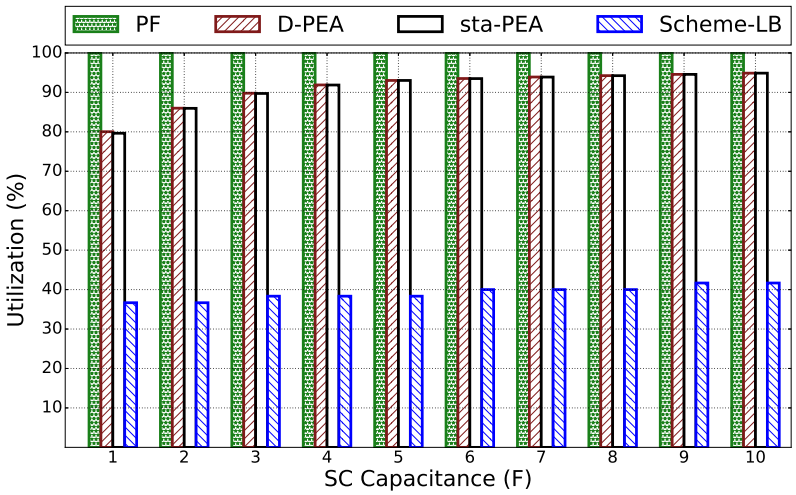

Figure 3.7: Harvesting Energy Utilization

Its conservative energy budgeting leads to a substantial amount of energy overflow. The proposed D-PEA (uses the optimal working point V^* as the set-point) achieves comparable utilization as sta-PEA (uses $1.2\,\mathrm{V}$ as the set-point). For D-PEA and sta-PEA, their utilization rates increase monotonically with SC capacitance. This result verifies Proposition 3.2 that for predictive energy allocation, a higher set-point value, such as $V^* = V_{dd}$, does not compromise the long term energy budgeting. The predictive energy budgeting algorithms (D-PEA and sta-PEA) achieve twice of the energy utilization rate as the non-predictive budgeting algorithm (Scheme-LB). It demonstrates that predictive power management is an enabler of high energy utilization.

On the other hand, predictive allocation algorithms have risks of over-assigning energy which potentially leads to power shortage. It is essential to consider the system power failure time t_f. In this part, the unexpected system power failure is considered to be caused by over-budgeting. Other cases, such as lack of energy harvesting opportunities, are excluded from t_f. Figure 3.8 compares the proposed D-PEA and sta-PEA in terms of power failure time t_f. PF and Scheme-LB can avoid over-budgeting, so they are not included in Figure 3.8 (PF is aware of the exact future energy generation rate. Scheme-LB uses non-predictive energy allocation.). D-PEA achieves consistently lower t_f compared with sta-PEA. The improvement of D-PEA ranges from 21.95% to 93.88%. The performance margin increases

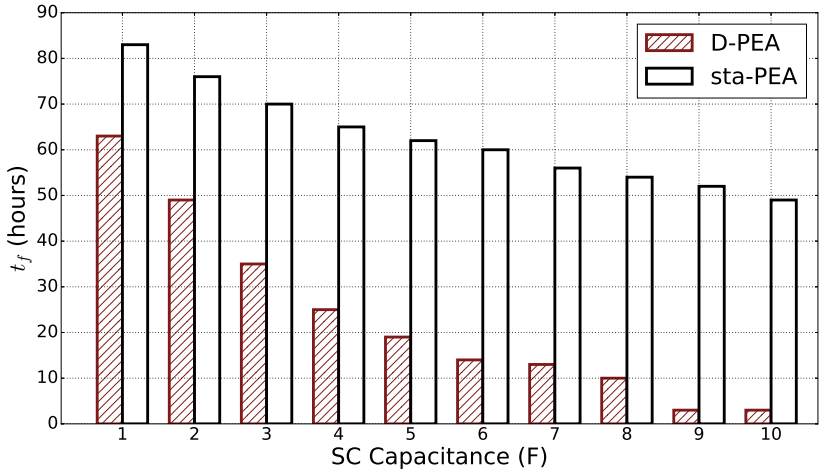

Figure 3.8: Power failure time t_f

with the SC capacitance. It demonstrates that the deviation awareness and coefficient adaptation of D-PEA can better respond to the prediction errors and avoid depleting the energy storage device. For both predictive budgeting algorithms, with a larger size of the energy storage device, the power failure time t_f drops due to the increased capability of energy buffering against predictor errors.

The results from Figures 3.7 and 3.8 show that compared with sta-PEA, D-PEA achieves high energy utilization rate and at the same time, maintains low system power failure time.

As stated earlier, another important aspect of IoBT power management is to reduce system power loss P_{loss}. Figure 3.9 shows a comparison of P_{loss} from different energy allocation algorithms. D-PEA achieves the lowest power loss. Compared with sta-PEA, D-PEA achieves 5.63% to 17.49% reduction in the system power loss. The terminal voltage deviance ΔV is used to explain the effectiveness of D-PEA in reducing system power loss P_{loss}. ΔV represents the runtime voltage deviation from the optimal working point V^*, defined in Equation (3.33). Figure 3.10 shows a bar plot of the average voltage deviance ΔV and its standard deviation. The system power loss P_{loss} is directly correlated to the voltage difference ΔV. On average, the proposed D-PEA achieves the lowest ΔV compared with the other three algorithms. Scheme-LB has the highest deviation. Due to its conservative energy allocation, the SC quickly accumulates energy so that the terminal

voltage V_{sc} is high, which causes a large voltage deviation ΔV. Even though PF has accurate information of future energy, it incurs the second highest voltage deviation. In order to achieve temporal fair allocation, PF requires the system to hold the surplus energy to make up for the future deficit. Thus, the variation of the SC terminal voltage is significant. The proposed D-PEA can recognize the terminal voltage difference by comparing V_{sc} with the optimal working point V^* and then make adjustment accordingly. Figures 3.9 and 3.10 validate that D-PEA is effective in reducing system power loss.

$$\Delta V = |V_{sc} - V^*| \tag{3.33}$$

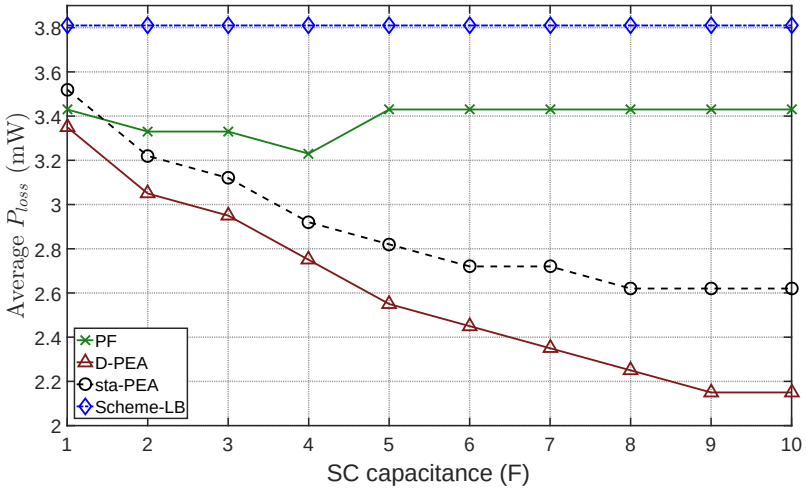

Figure 3.9: Overall IoBT power loss P_{loss}

3.3.3 Energy efficient Transmission Power Control

In this subsection, the proposed ETPC is evaluated. This part considers an IoBT system serving as a sender. A sink is responsible for receiving messages and piggy-backing the RSSI data every 10 minutes ($m = 6$). The minimum received signal strength P_r at the sink is set to be $-100\,\mathrm{dBm}$. The energy per useful bit, E_u, is used to evaluate ETPC. The wireless channel is emulated to be outdoor environment with the log-shadowing model [85], whose attenuation factor is 4 and the variation is $6\,\mathrm{dB}$. The noise P_n is considered to be

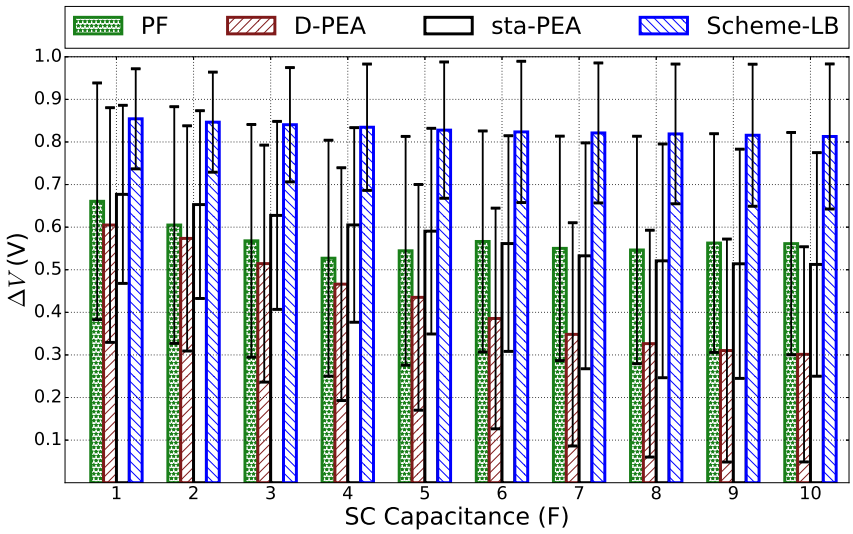

Figure 3.10: Distribution of the terminal voltage deviation ΔV

Gaussian white noise with mean of $-105\,\mathrm{dBm}$ and standard deviation of $1.5\,\mathrm{dBm}$. The packet size l is $32\,\mathrm{bytes}$. The transmission rate R is set to be $19.2\,\mathrm{kbps}$. By varying the distance between the sender and the receiver, different channel fading conditions are emulated. CC2500 is emulated as the wireless transceiver. Its programmable transmission power P_t ranges from $-30\,\mathrm{dBm}$ to $0\,\mathrm{dBm}$ with a step size of $2\,\mathrm{dBm}$. The power consumption of the transceiver comes from the datasheet [87]. For comparison, the fixed received signal strength based scheme [43, 44] (referred to as P_r*-scheme*) and the fixed packet receive rate based scheme [45] (referred to as *PRR-scheme*) are also implemented.

Figure 3.11 demonstrates the performance from different transmission power control schemes with the distance d from $1\,\mathrm{m}$ to $20\,\mathrm{m}$. Figure 3.11(a) and Figure 3.11(b) compare ETPC with P_r-scheme and PRR-scheme, respectively. In both comparisons, ETPC achieves consistently lower energy per received bit E_u. Table 3.1 demonstrates the maximum energy efficiency improvement by ETPC. Compared with P_r schemes and PRR schemes, ETPC brings an energy reduction up to 23.22% and 21.62%, respectively.

To improve the energy efficiency E_u, the tradeoff between transmission reliability and power consumption needs to be considered. A high received signal strength P_r improves the packet receive rate PRR. But at the same time, it incurs more power consumption

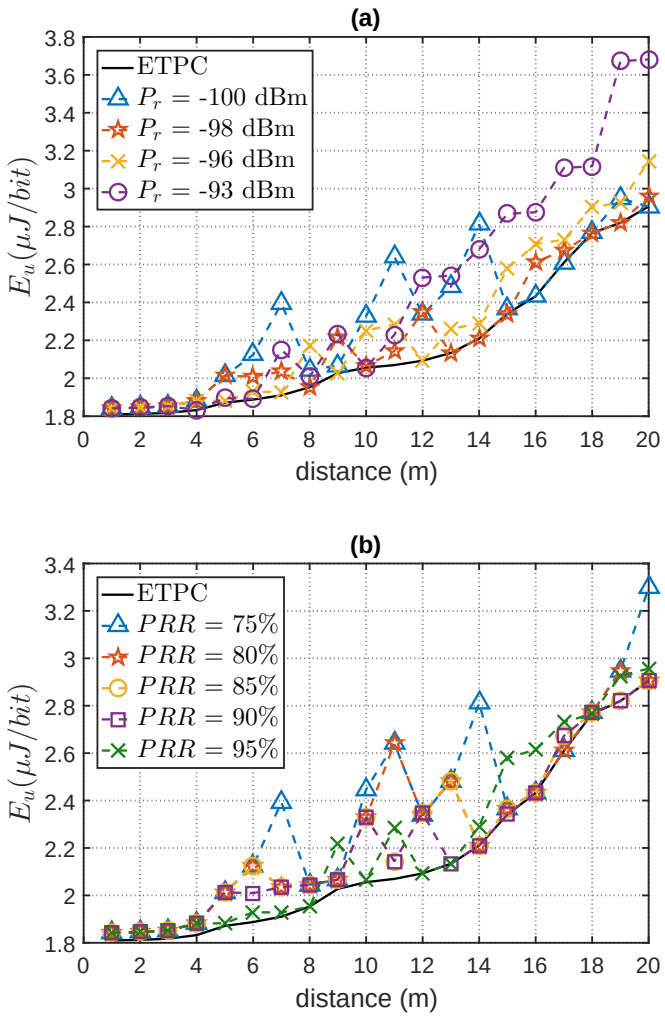

Figure 3.11: Energy per useful bit E_u : (a) ETPC and fixed P_r scheme; (b) ETPC and fixed PRR scheme

both from the transceiver and DC-DC regulator. On the other hand, a low received signal strength P_r cannot guarantee high energy efficiency either. A low P_r compromises the packet receive rate PRR and thus lead to more retransmissions. Figure 3.12 explains the problem by showing the optimal selection of P_r and PRR from ETPC. It shows that a general trend is, in the cases of short distance, a high P_r is energy efficient. This is because that the low path loss value does not require a high transmission power P_t to achieve transmission reliability. On the other hand, when the distance d is large, a high received signal strength P_r is energy consuming due to the high path loss. The benefit of using low transmission power outweighes the drawback of more retransmissions $\bar{k}$. Figures 3.11 and 3.12

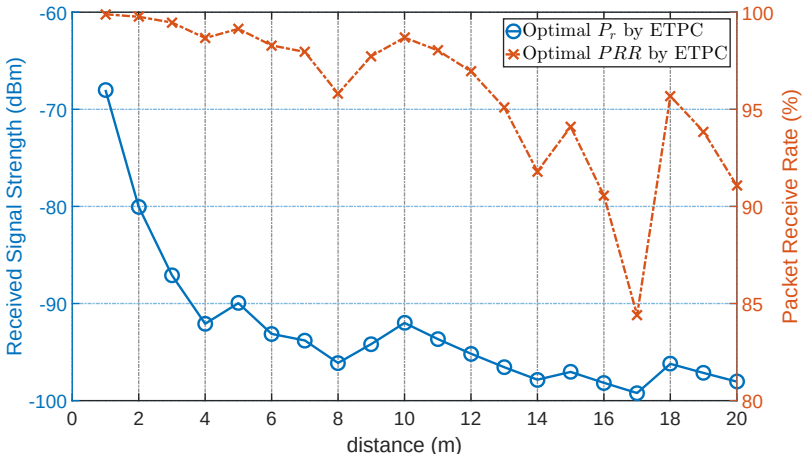

Figure 3.12: Optimal P_r and PRR selected by ETPC

Table 3.1: Maximum transmission energy efficiency improvement of ETPC

Schemes		Maximum Improvement (%)
P_r schemes	$P_r = -100\,\text{dBm}$	21.42
	$P_r = -98\,\text{dBm}$	10.88
	$P_r = -96\,\text{dBm}$	10.16
	$P_r = -93\,\text{dBm}$	23.22
PRR schemes	$PRR = 75\%$	21.62
	$PRR = 80\%$	21.53
	$PRR = 85\%$	14.09
	$PRR = 90\%$	11.69
	$PRR = 95\%$	9.4

validate the optimal energy efficiency of ETPC compared with the state-of-the-art schemes. For IoBT systems, set-point-based transmission power controllers cannot achieve optimal energy efficiency over varying wireless channel quality.

3.4 Conclusion

Enabled with unbounded lifetime, IoBT systems provides a low-cost and environment-friendly solution to the energy bottleneck. Power management plays an important role in the operation of IoBT systems. In this chapter, a novel predictive power management, PPM, is proposed to achieve energy efficient and reliable operation of IoBT. PPM takes into account three major aspects of IoBT systems, including system power loss, dynamic

energy allocation and energy efficient wireless transmission.

Based on the IoBT system model, optimal working point is derived to minimize the system power loss. D-PEA tracks the runtime SC voltage deviation from the optimal working point and dynamically adjust energy allocation to mitigate the prediction errors. D-PEA minimizes the power failure time and the system power loss while maintaining a high energy utilization. ETPC selects optimal transmission power based on the wireless channel condition. Extensive simulations are conducted to demonstrate the effectiveness of PPM. Compared with the state-of-the-art power managers, PPM achieves up to 93% reduction of power failure time and 15% of less system power loss. At the same time, PPM maintains a high energy utilization rate, which is close to the theoretical upper bound. Compared with the conventional transmission power control schemes, PPM also achieves up to 23% of improved transmission energy efficiency.

PPM lays a theoretical foundation for the efficient operation of IoBT systems, which can be utilized to develop novel management schemes. Based on the mathematical proof, the optimal working point is applicable to SC-operated systems with DC-DC regulators, which can be used as a set-point to achieve optimal energy efficiency over varying DC-DC efficiency and SC leakage. Furthermore, two propositions and one observation are derived from the ENO condition and the IoBT energy dynamics, which can serve as a basis to design adaptive resource allocation algorithms for energy harvesting systems. In addition, ETPC is applicable to a wide variety of wireless communication systems, where transmission power is desired be optimized to improve the energy efficiency.

CHAPTER 4

CLUSTERED DATA COLLECTION

Due to the limited sensing coverage and constrained hardware resources, a single IoBT system is not sufficient for the future 5G applications that require dense deployment of self-sustained systems. It is desired to design network-level power management strategies to enable high-throughput and collaborative data collection for multiple IoBT nodes. In this chapter, a novel clustered data collection framework is designed to achieve optimal data collection rate for IoBT networks with low overhead.

The rest of the chapter is organized as follows. Section 4.1 presents IoBT-operated cluster. Section 4.2 details the proposed adaptive clustering mechanism. Section 4.3 presents the simulation results for evaluation and Section 4.4 concludes the chapter.

4.1 IoBT-operated Cluster

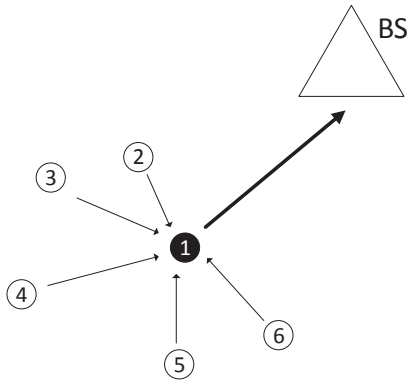

Figure 4.1: IoBT cluster model

This chapter considers IoBT system as a low-power IoT system (such as a wireless sensor node) equipped with a small-sized energy harvesting module, such as a stamp-sized solar cell. The operation of IoBT systems is divided into *rounds*. Each round has a time length of T seconds. The energy generation in the tth round, $E_{har}(t)$, is time-varying and

affected by the ambient environment. $B(t)$ quantifies the usable energy stored in the SC at the beginning of the tth round, which can be measured by the MCU of the system. A wireless transceiver is responsible for data transmission and reception. The energy evolution of the IoBT system is formulated in function (4.1), where C is the maximum energy capacity of the SC. $S(t)$ stands for the energy spending in the tth round. The energy budget is based on the remaining energy in the SC. Thus, the energy expenditure $S(t)$ is in the range of $[0, B(t)]$. The energy consumption $S(t)$ depends on the role of the IoBT node in the tth round.

$$B(t) = min\{B(t-1) + E_{har}(t-1) - S(t-1), C\}. \tag{4.1}$$

According to [54], an IoBT cluster consists of n IoBT nodes deployed in a field. V is defined to be the set of all the nodes in the cluster. Each IoBT node can individually perform transmission power control to reach the BS as well as the other peer nodes in the cluster. There are two types of nodes in a cluster. A CH node is responsible for data collection, data aggregation and data forwarding back to the BS. The remaining nodes are CM nodes, whose main duty is to collect and transmit data to the CH node. V_{CM} is defined to be the set containing all the CM nodes[1]. Figure 4.1 gives an example of an IoBT cluster. Node 1 is a CH node while Nodes 2, 3, 4, 5 and 6 are CM nodes.

$$S_k(t) = \lambda^{tx}_{k,CH} R_k(t) T, \quad k \in V_{CM} \tag{4.2}$$

In the tth round, if node k is a CM node, then its energy consumption $S_k(t)$ depends on the data it reports to the CH node, which is described in Equation (4.2). CH is the node ID of the CH node. Considering that a wireless transceiver has much higher power consumption comparing with MCU and micro sensors, the transceiver power consumption is used to approximate the overall IoBT node power consumption. $\lambda^{tx}_{k,CH}$ is the transmission

[1]For each cluster, there is exactly one CH node so that the number of the CM nodes is $(n-1)$. Thus, $V = V_{CM} \cup \{CH\}$. This chapter focuses on the operation of a single IoBT cluster.

energy cost from node k to the CH node, which stands for joule per bit. $R_k(t)$ is the transmission rate from the CM node k to the CH node.

$$S_k(t) = T \sum_{j \in V_{CM}} \lambda^{rx}_{k,j} R_j(t) + T\lambda^{DA} \frac{R_k(t)}{\rho} + T\lambda^{tx}_{k,BS} R_k(t), \qquad CH = k \tag{4.3}$$

$$R_k(t) = \rho \sum_{j \in V_{CM}} R_j(t), \qquad CH = k \tag{4.4}$$

On the other hand, if node k is a CH node in the tth round ($CH = k$), then its energy expenditure is illustrated in Equation (4.3). $R_{CH}(t)$ is referred to as the *data collection rate* of the cluster, shown in Equation (4.4), where ρ stands for the data aggregation ratio. For practical consideration, ρ is restrained in the range of $[0, 1]$. $\lambda^{rx}_{k,j}$ stands for the energy consumption per received bit in the receiver node k from the sender node j. For Equation (4.3), the first term stands for the data collection cost from all the $(n-1)$ CM nodes. The second term is to derive the energy overhead incurred by data aggregation, where λ^{DA} is the energy per bit for data aggregation. The last term is the energy cost of forwarding the aggregated data back to the BS. $\lambda^{tx}_{k,BS}$ refers to the transmission energy cost per bit from the CH node k to the BS.

4.2 Data Collection for Clustered IoBT

Due to the dynamics of the renewable energy source, IoBT based adaptive clustering contains two major problems: (1) CH selection; and (2) rate assignment for each node. For a conventional battery-operated cluster, a CH node is first elected and then each CM node follows a fixed reporting rate to communicate with the CH node. However, for an IoBT cluster, the CH selection will affect the throughput of the cluster. These two problems are interweaved for IoBT-based clusters. The existing CH selection schemes, based on either probabilistic CH re-election [54, 58, 56], or optimal location search [88], focus on balanc-

ing the energy consumption of the clustered nodes so that the overall network lifetime is prolonged for conventional battery-operated systems. These methods cannot guarantee an optimal data collection rate for an IoBT cluster.

In this section, a lexicographic optimal rate assignment algorithm is first presented assuming a given CH node. Then, two CH selection schemes are designed, including an optimal CH selection scheme and an approximation-based CH selection scheme that achieves comparable data collection rate as that of the optimal CH selection scheme with a much lower computational cost.

4.2.1 Lexicographic Rate Assignment for IoBT Cluster

This subsection seeks to derive the lexicographic optimal rate assignment with a given CH node. The definition for lexicographic order and lexicographic optimality is as follows:

Definition 4.1 Let $\boldsymbol{R} = [R_1, ..., R_n]$ and $\boldsymbol{R'} = [R'_1, ..., R'_n]$ be two feasible rate assignments that are sorted in nondecreasing order. (1) if $R_i = R'_i$ for any $i = 1, 2, ...n$, then the rate assignment $\boldsymbol{R}$ is lexicographically equal to $\boldsymbol{R'}$; (2) if there exists a node i such that $R_i > R'_i$ and $R_j = R'_j$ for any $1 \leq j \leq i-1$, then the rate assignment $\boldsymbol{R}$ is lexicographically greater than $\boldsymbol{R'}$; (3) $\boldsymbol{R}$ is lexicographically optimal if it is lexicographically greater than all the other feasible rate assignments.

The problem of Lexicographic Rate Assignment for IoBT Cluster (LRIC) is formulated as follows:

For the tth round, given CH as the CH node ID and the energy budget vector $\boldsymbol{B}(t) \triangleq [B_1(t), ..., B_n(t)]$ for all the IoBT cluster nodes:

$$Lexicographically\ maximize : \{R_k(t)\}, k \in V_{CM} \tag{4.5}$$

$$s.t. :\ 0 \leq S_k(t) \leq B_k(t), \qquad k \in V \tag{4.6}$$

$$0 \leq R_k(t) \leq R_{k_{max}}, \qquad k \in V \tag{4.7}$$

The remaining energy stored in the SC is used as the energy budget. Equation (4.6) represents the energy restraints for each node. Equation (4.7) illustrates the link capacity restriction for the nodes, which is imposed by the wireless channel.

Algorithm 4.1 (LRIC) is developed to solve the lexicographic optimization problem. The LRIC algorithm follows a principle of "fair increment until saturated". It starts with a zero rate vector for all the CM nodes (line 4 in Algorithm 4.1). A_{CM} is defined to be the set containing all the CM nodes with saturated rate. Initially, A_{CM} is set to be an empty set. LRIC iterates through all the CM nodes, increasing the rate over all the CM nodes fairly with a step size of s. $\tilde{\boldsymbol{r}}(t) \triangleq [\tilde{r}_1(t), ..., \tilde{r}_n(t)]$ and $\tilde{\boldsymbol{S}}(t) \triangleq [\tilde{S}_1(t), ..., \tilde{S}_n(t)]$ stand for the rate vector and energy consumption vector with the rate increment of step size s, respectively. The function *rate_check* (lines 24 to 32 in Algorithm 4.1) verifies whether the incremented data rate $\tilde{R}_i(t)$ will result in energy deficit either for the node i itself or for the CH node. The lexicographic optimal rate $\boldsymbol{r}(t) \triangleq [r_1(t), ..., r_n(t)]$ is finalized when all the CM nodes have saturated their rates. $\boldsymbol{S}(t) \triangleq [S_1(t), ..., S_n(t)]$ represents the corresponding energy expenditure vector.

In order to prove the lexicographic optimality of Algorithm 4.1, several useful terms are first introduced in Definition 4.2. Then, Propositions 4.1 and 4.2 demonstrate the inherent properties of Algorithm 4.1, which will be further utilized to verify the lexicographic optimality.

Definition 4.2 In the tth round, for an IoBT node k with the usable energy $B_k(t)$ and an allocated energy expenditure $S_k(t)$: (1) if $S_k(t) \in [B_k(t) - \epsilon, B_k(t)]$ for arbitrary $\epsilon > 0$, then node k is *energy throttled* in the tth round. Q_t is defined to be the set containing all the nodes that are energy throttled in the tth round ; (2) if there exists an $e > 0$, $S_k(t) \in [0, B_k(t) - e]$, then node k is *energy sufficient* in the tth round. Similarly, $\bar{Q}_t$ is the set of the energy sufficient nodes in the tth round.

Algorithm 4.1: Lexicographic Rate for IoBT Cluster (LRIC)

Input : $\boldsymbol{B}(t), CH$;
Output: $\boldsymbol{r}(t)$;
Init : $\boldsymbol{r}(t)$, $\boldsymbol{S}(t)$, $\tilde{\boldsymbol{R}}(t)$, $\tilde{\boldsymbol{S}}(t) \leftarrow \mathbf{0}$;
$A_{CM} \leftarrow \varnothing$;
while $A_{CM} \neq V_{CM}$ **do**
  for $i = 1; i \leq n; i++$ **do**
    if $i \notin A_{CM}$ **and** $i \neq CH$ **then**
      $\tilde{\boldsymbol{R}}(t) \leftarrow \boldsymbol{r}(t)$;
      $\tilde{\boldsymbol{S}}(t) \leftarrow \boldsymbol{S}(t)$;
      $\tilde{R}_i(t) \leftarrow \tilde{R}_i(t) + s$;
      $\tilde{R}_{CH}(t) \leftarrow \tilde{R}_{CH}(t) + \rho s$;
      $\tilde{S}_i(t) \leftarrow \tilde{S}_i(t) + sT \cdot \lambda^{tx}_{CH,i}$;
      $\tilde{S}_{CH}(t) \leftarrow \tilde{S}_{CH}(t) + sT(\lambda^{rx}_{CH,i} + \lambda^{DA} + \rho\lambda^{tx}_{CH,BS})$;
      if *rate_check*$\big(\tilde{R}_i(t), \tilde{S}_i(t), B_i(t), \tilde{R}_{CH}(t), \tilde{S}_{CH}(t), B_{CH}(t)\big) == TRUE$ **then**
        $\boldsymbol{r}(t) \leftarrow \tilde{\boldsymbol{R}}(t)$;
        $\boldsymbol{S}(t) \leftarrow \tilde{\boldsymbol{S}}(t)$;
      else
        $A_{CM} \leftarrow A_{CM} \cup \{i\}$;
      end
    end
  end
end
Function *rate_check*$\big(\tilde{R}_i(t), \tilde{S}_i(t), B_i(t), \tilde{R}_{CH}(t), \tilde{S}_{CH}(t), B_{CH}(t)\big)$
  valid $\leftarrow$ TRUE;
  if $\tilde{S}_{CH}(t) > B_{CH}(t)$ **or** $\tilde{R}_{CH}(t) > R_{CH_{max}}$ **then**
    valid $\leftarrow$ FALSE;
  end
  if $\tilde{S}_i(t) > B_i(t)$ **or** $\tilde{R}_i(t) > R_{i_{max}}$ **then**
    valid $\leftarrow$ FALSE;
  end
  return *valid;*

Considering that the step size s can be arbitrarily small, Propositions 4.1 and 4.2 are obtained. Based on the propositions, the proposed LRIC can be proven to be lexicographically optimal, as shown in Theorem 4.1. The detailed proof of Propositions 4.1, 4.2 and Theorem 4.1 are in Appendix B.

Proposition 4.1 Let $\boldsymbol{r}(t) = [r_1(t), ..., r_n(t)]$ be the rate vector assigned by Algorithm 4.1 for the tth round. If $CH \in \bar{Q}_t$, then for any CM node j, $j \in Q_t$.

Proposition 4.2 Let $\boldsymbol{r}(t) = [r_1(t), ..., r_n(t)]$ be the rate vector assigned by Algorithm 4.1 for the tth round. If $Q_t \neq \varnothing$ and $\bar{Q}_t \neq \varnothing$, then: (1) for any CM nodes j and k, if $j \in Q_t$, $k \in \bar{Q}_t$, then $r_k(t) \geq r_j(t)$; (2) for any CM nodes a and b, if $a, b \in \bar{Q}_t$, then $r_a(t) = r_b(t)$; (3) for any CM node j, if $j \in \bar{Q}_t$, then $r_j(t) = \max\limits_{k \in V_{CM}} r_k(t)$.

Theorem 4.1 Algorithm 4.1 (LRIC) computes the optimum lexicographic rate assignment for the IoBT cluster.

The function *rate_check* has complexity of $O(1)$. For any CM node k, the energy budget is based on its remaining energy $B_k(t)$ and $B_k(t) \in [0, C]$. The maximum number of operations it takes to saturate the rate of node k is $\frac{C}{sT\lambda^{tx}_{k,CH}}$. Thus, for Algorithm 4.1, the time complexity is $O([n-1]\frac{C}{sT\hat{\lambda}})$, where $\hat{\lambda} = \min\limits_{k \in V_{CM}} \lambda^{tx}_{k,CH}$.

4.2.2 Cluster Setup

At the beginning of each round, the cluster is initialized by every IoBT node reporting to the BS. For each IoBT node, a short message containing the node ID and the remaining energy level is sent to the BS.

Once the BS is informed of the remaining energy of all IoBT nodes, it will select a CH node based on a certain criteria. The CH selection is formulated as the data collection rate maximization problem shown in Equation (4.8), where $r_{CH=i}(t)$ is the CH data collection rate if node i serves as a CH node in the tth round.

$$CH^* = \arg\max_{i \in V} \; r_{CH=i}(t) \tag{4.8}$$

In this section, two CH selection algorithms are proposed, namely, Exhausted Search (ES) and Approximated Search (AS).

ES is detailed in Algorithm 4.2. For each node, lexicographic rate assignment is called for each node to derive the optimal rate if it is elected as a CH node. Algorithm 4.2 selects the node with the highest data rate (line 8 in Algorithm 4.2) and outputs the CH node ID. The corresponding lexicographic rate vector will be the assignment for the incoming round (line 9 in Algorithm 4.2). ES traverses all the possible CH candidates and derives the optimal CH rates to guarantee that the selected node has the highest data rate. $\dot{\boldsymbol{r}}(t) \triangleq \{r_j^{(i)}(t)\}_{i=1,...,n;j=1,...,n}$ is defined to be an $n \times n$ matrix in which each element $r_j^{(i)}(t)$ denotes the data collection rate of node j when node i serves as the CH node in the tth round. $\dot{\boldsymbol{r}}^{(i)}(t) \triangleq [r_1^{(i)}(t), ..., r_n^{(i)}(t)]$ denotes the rate vector for the clustered nodes when node i serves as the CH node. Despite the optimality, ES incurs high computational complexity. The total complexity of Algorithm 4.2 is $O(n^2)$.

The CH selection is based on the maximum CH data collection rate. It is not necessary to derive the entire lexicographic rate vector for all the nodes. Thus, AS is proposed to save the unnecessary computations by approximation, which is detailed in Algorithm 4.3. $\tilde{\boldsymbol{r}}_{CH}(t) \triangleq [\tilde{r}_{CH=1}(t), ..., \tilde{r}_{CH=n}(t)]$ is denoted to be the vector that contains the CH data collection rate of all the possible CH candidates. AS still traverses all the CH candidate nodes but the unnecessary lexicographic rate computation is saved. According to Proposition 4.1, with the lexicographic rate assignment, if the CH node is energy sufficient, then all the CM nodes must be energy throttled. This case is checked in Algorithm 4.3 from line 9 to 10. If the case is true, AS uses line 10 to update the data collection rate for the candidate node i. For the other case wherein the CH node is energy throttled, AS uses the upper bound r_{max} and the lower bound r_{min} to approximate the data collection rate for node i. Finally, the CH is elected based on a highest data collection rate. The time complexity of AS is $O(n)$.

Proposition 4.3. For an IoBT cluster, if $\lambda_{i,j}^{rx} = \lambda_{i,k}^{rx}$ with any $i, j, k \in V$ and $j \neq k \neq i$,

then Algorithm 4.3 is optimum.

The proof of Proposition 4.3 is in Appendix B.4. Proposition 4.3 shows that if the receiving costs from different senders are the same, AS is optimal. In real deployment, each IoBT node performs wireless transmission power control [89] to maintain stable wireless link quality[2]. Thus, AS provides a close approximation to the optimal ES.

After the CH node is elected and the optimal rate assignment is derived, the BS informs the selected node with a control packet containing the optimal rate vector. Then the CH node broadcasts an Advertisement message (ADV) containing the optimal rate assignment. Once all the CM nodes receive the ADV message, each of them sends a join-request message back to the CH node. When the CH node acknowledges the join requests from all the CM nodes, a Time Division Multiple Access (TDMA) schedule is established to enable clustered data collection for the coming round.

Algorithm 4.2: Exhausted Search (ES)

Input : $\boldsymbol{B}(t)$;
Output: CH^*;
$\boldsymbol{r}(t)$;
Init : $\dot{\boldsymbol{r}}(t) \leftarrow \mathbf{0}$;
for $i = 1$; $i \leq n$; $i++$ **do**
  $\dot{\boldsymbol{r}}^{(i)}(t) \leftarrow$ LRIC($\boldsymbol{B}(t)$, i);
end
$CH^* \leftarrow \arg\max_{i \in V} \{\rho \sum_{j \neq i}^{j \in V} r_j^{(i)}(t)\}$;
$\boldsymbol{r}(t) \leftarrow \dot{\boldsymbol{r}}^{(CH^*)}(t)$;

In an IoBT-operated cluster with n nodes, the message complexity of each round is studied. Due to the fact that the transmission cost inside the cluster is different from the cost from the clustered nodes to the BS, two kinds of message overhead are considered: (1) node-to-node overhead; and (2) node-to-BS overhead. The node-to-BS overhead is mainly incurred by the initial reporting process that every node informs the BS about the remaining

[2]It has been demonstrated that the existing wireless transmission power controllers [45, 89] are capable of maintaining a stable Packet Error Rate between 10% to 20%.

Algorithm 4.3: Approximated Search (AS)

Input : $\boldsymbol{B}(t)$;
Output: CH^*;
Init : $\tilde{\boldsymbol{r}}_{CH}(t) \leftarrow \mathbf{0}$;
$\Lambda^{rx}_{max},\ \Lambda^{rx}_{min},\ r_{max},\ r_{min},\ \check{r} \leftarrow 0$;
for $i = 1;\ i \leq n;\ i++$ **do**
  $\check{r} \leftarrow \sum_{\substack{j \in V \\ j \neq i}}^{j \in V} \frac{B_j(t)}{T\lambda^{tx}_{j,i}}$;
  $\Lambda^{rx}_{max} \leftarrow \max_{\substack{j \in V \\ j \neq i}} \{\lambda^{rx}_{i,j}\}$;
  $\Lambda^{rx}_{min} \leftarrow \min_{\substack{j \in V \\ j \neq i}} \{\lambda^{rx}_{i,j}\}$;
  if $B_i(t) > T\Lambda^{rx}_{max}\check{r} + (T\lambda^{DA} + \rho T\lambda^{tx}_{i,BS})\check{r}$ **then**
    $\tilde{r}_{CH=i}(t) \leftarrow \rho\check{r}$;
  else
    $r_{max} \leftarrow \frac{\rho \cdot B_i(t)}{T(\Lambda^{rx}_{min} + \lambda^{DA} + \rho\lambda^{tx}_{i,BS})}$;
    $r_{min} \leftarrow \frac{\rho \cdot B_i(t)}{T(\Lambda^{rx}_{max} + \lambda^{DA} + \rho\lambda^{tx}_{i,BS})}$;
    $\tilde{r}_{CH=i}(t) \leftarrow \frac{1}{2}(r_{max} + r_{min})$;
  end
end
$CH^* \leftarrow \arg\max_{i \in V} \{\tilde{r}_{CH=i}(t)\}$;

energy. When the BS notifies the selected CH node, the CH node needs to acknowledge its role. Thus, the node-to-BS complexity is roughly $n + 1 = O(n)$. The node-to-node complexity is due to the following: (1) the CH node broadcasts ADV; (2) the CM nodes send join requests; and (3) the CH node acknowledges the join requests. The overall node-to-node overhead is $1 + (n-1) + (n-1) = 2n - 1$. The node-to-node overhead is also $O(n)$.

4.3 Evaluation

4.3.1 Simulation Setup

A MABLAB-based simulation framework is developed to evaluate the proposed clustered data collection framework. The IoBT node positions are randomly generated following the

uniform distribution within the deployment field. The simulation parameters are listed in Table 4.1.

4.3.1.1 IoBT cluster

A $20\,\mathrm{m} \times 20\,\mathrm{m}$ square is emulated as the field where the IoBT nodes are deployed as a cluster. The BS is deployed in the position ($x = 10$, $y = 35$). Each round time T is 10 minutes. Each IoBT node has an energy capacity $C = 10\,\mathrm{J}$. Initially, each IoBT node has $0.5\,\mathrm{J}$ of usable energy.

Table 4.1: Simulation Parameters

Parameters	**Description**
Field Area for cluster Deployment	$20\,\mathrm{m} \times 20\,\mathrm{m}$
Node Distribution	Generated Randomly based on Uniform Distribution
BS position	$x = 10\,\mathrm{m}$, $y = 35\,\mathrm{m}$
Initial Energy of Each Node	$0.5\,\mathrm{J}$
Energy Capacity	$C = 10\,\mathrm{J}$
Round Time	$T = 10\,\mathrm{min}$
Wireless Communication Standard	IEEE 802.15.4
Frequency Band	$2.4\,\mathrm{GHz}$
Modulation	Quadratic Phase Shift Keying
Control Packet Size	$200\,\mathrm{bits}$
Data Packet Size	$4000\,\mathrm{bits}$
Data aggregation cost	$5\,\mathrm{nJ/bit}$
Photovoltaic Cell Size	$A = 2.5\,\mathrm{cm}^2$
Photovoltaic Cell Conversion Efficiency	η =10%

4.3.1.2 Wireless Communication

The state-of-the-art log-shadowing model [85] is used to establish the wireless channel. The attenuation factor is 4 and the variation is $5.7\,\mathrm{dB}$ to emulate an outdoor channel [90]. The log-shadowing model is verified with hardware experiments in the existing literatures [85, 91]. The noise is considered to be Gaussian white noise with a mean of $-105\,\mathrm{dBm}$ and a standard deviation of $1.5\,\mathrm{dBm}$ based on [44].

The emulated IoBT nodes use IEEE 802.15.4 as the communication standard with the frequency band of $2.4\,\mathrm{GHz}$. TI CC2500 [87] is emulated as the wireless transceiver providing a tunable wireless transmission power from $-30\,\mathrm{dbm}$ to $1\,\mathrm{dbm}$. Each IoBT node performs transmission power control described in [89] to maintain stable link quality. The transmission cost $\{\lambda^{tx}\}$ and the reception cost $\{\lambda^{rx}\}$ are derived based on the method presented in [85].

4.3.1.3 Energy Harvesting

The simulation uses a $2.5\,\mathrm{cm}^2$ photovoltaic cell with 10% efficiency to convert the light irradiance trace into the energy harvesting trace using the method introduced in [36]. A 30-day real world outdoor solar irradiance trace [71] (From May. 1, 2015 to May. 30, 2015) is used to generate the energy harvesting profile. This kind of trace-driven simulation is widely used in the previous energy harvesting research works [4, 92, 38] and has been experimentally validated to be effective in providing close estimation of the energy harvested from a photovoltaic cell.

To account for the harvested power deviation caused by the node position, the harvested power is varied by a random amount between -15% to 15% of the baseline for each IoBT node. The IoBT cluster is assumed to operate from 8:00 AM to 5:00 PM when solar energy is available[3].

4.1.3.4 Referenced Algorithms

Some widely adopted heuristic CH selection strategies [54, 88, 57] are also implemented for comparisons. The proposed methods are referred to as *ES* scheme and *AS* scheme, respectively. The benchmark strategies are:

(1) CH is selected based on the maximum remaining energy (referred to as *Max Energy*

[3]During the night time when there is no energy harvesting opportunity, the IoBT-operated cluster is similar to the traditional clustered WSNs with finite energy. Please refer to the conventional clustering algorithms [54, 58] for lifetime extension.

scheme);

(2) CH is randomly selected from the candidates which have not been CH for the past n rounds (referred to as *Round Robin* scheme);

(3) CH is selected based on the minimum transmission cost from the CM nodes to the CH node (referred to as *Min CM-CH cost* scheme);

(4) CH is selected based on the minimum transmission cost from CH to the BS (referred to as *Min CH-BS cost* scheme);

(5) CH is selected based on the minimum listening cost (referred to as *Min Listen cost* scheme)

Due to the absence of adaptive rate assignment module in the related works, these CH selection schemes are combined with the proposed lexicographic rate assignment algorithm in the evaluation.

4.3.2 A Four-node Test Case

A 4-node test case is first investigated. The corresponding topology is shown in Figure 4.2. The daily data collection rate of the CH, $\bar{R}_{CH}$, is used to quantify the throughput the cluster. Figure 4.3 shows that the proposed methods (ES and AS) achieve almost the same data collection rate and outperform all the other schemes over the data aggregation ratio ρ. Figure 4.3 demonstrates that the CH selection policy makes a significant difference to the data collection rate that the cluster can provide to the BS.

To further investigate the performance gap, a statistical analysis is conducted based on the 30-day CH selection results of the four-node test case. Figure 4.4 shows a normalized histogram of the probability that each node is selected as a CH node. The results display notable distinction between different CH selection policies. For minimum cost based CH selection schemes (*Min CM-CH cost*, *Min CH-BS cost* and *Min Listen cost*), the CH role usually falls into one or two nodes. According to the topology shown in Figure 4.2, the CH selection from the minimum cost based schemes is closely associated with the position of

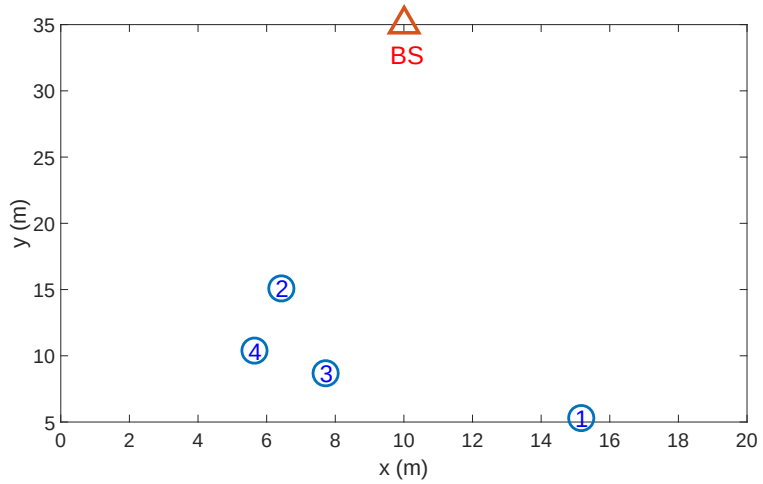

Figure 4.2: Topology of the four-node cluster test case

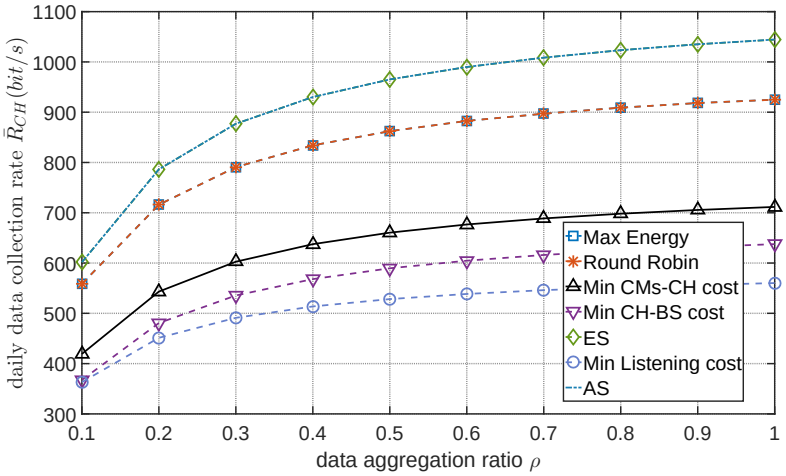

Figure 4.3: Daily average CH rate $\bar{R}_{CH}$ of the four-node test case

the IoBT nodes. The node with the shortest distance to the BS is mainly chosen as a CH node by the *Min CM-CH cost* scheme. The node in the central position is mostly selected as a CH node by the *Min CH-BS cost* and *Min Listen cost* schemes. However, the minimum cost based CH selection schemes overlook the dynamics of the energy harvesting, which leads to a relatively low data collection rate.

On the other hand, the *Max Energy* scheme fails to consider the wireless communication cost. Thus, the *Max Energy* scheme cannot achieve optimal data collection rate either. The *Max Energy* scheme selects node 1 with a probability of 46.73%., whereas the proposed *ES* and the *AS* schemes only have a chance of 3.38% in using node 1 as a CH node, considering

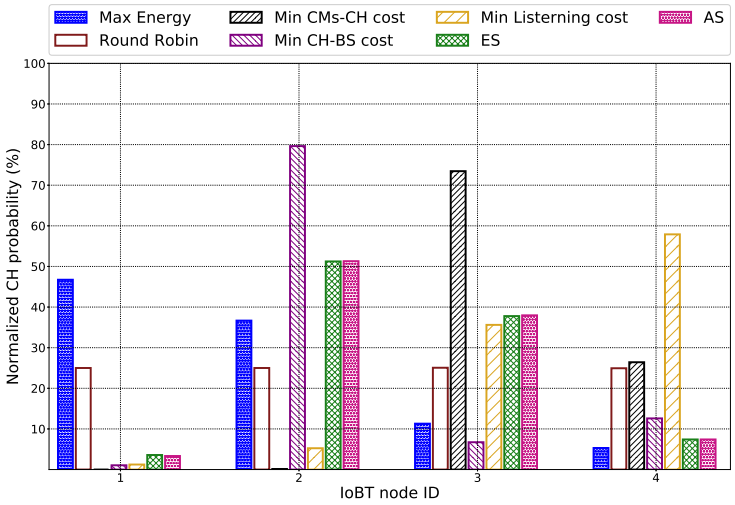

Figure 4.4: Histogram of CH selection ($\rho = 0.5$)

that node 1 has a high transmission cost to the BS[4].

During the selection of the CH node, it is desired to comprehensively consider both the remaining energy level and wireless transmission cost. ES traverses all the possible CH candidates and then chooses the one with the highest transmission rate. AS utilizes the inherent features of the lexicographic rate assignment and uses the approximation-based method to select the CH node. Figure 4.3 shows that these two schemes achieve very close data collection rate. The performance difference is only 0.0082% on average.

4.3.3 Densely Deployed Test Cases

More densely deployed test cases are evaluated. Figure 4.5 demonstrates performance improvement with the number of nodes, n, ranging from 4 to 40. The performance improvement Imp is defined in Equation (4.9). For each cluster size n, 20 randomly generated cluster topologies are tested based on uniform distribution. For each topology, a full range of the data aggregation ratio $\rho \in [0, 1]$ is investigated. The results shown in this subsection are the average values. Figures 4.5(a)-(e) show that the proposed ES scheme achieves

[4]From Figure 4.2, node 1 has the longest distance to the BS. Therefore, the transmission cost from node 1 to the BS is high.

higher data collection rate than the other schemes.

$$Imp = \frac{\bar{R}_{CH}(ES) - \bar{R}_{CH}(other\ scheme)}{\bar{R}_{CH}(other\ scheme)} \times 100\% \tag{4.9}$$

The ES scheme has similar improvement (ranging from 5% to 43%) over the *Max Energy* and the *Round Robin* schemes, which is consistent with the daily average collection rate results shown in Figure 4.3. The CH node has much higher power consumption compared with the CM nodes. After serving as a CH node for a round, the node no longer has the maximum remaining energy. It needs to accumulate harvested energy for several rounds to be re-elected as a CH node by the *Max Energy* scheme. Thus, the *Max Energy* scheme shows a similar throughput performance as the *Round Robin* scheme. However, due to the absence of the transmission cost, the *Max Energy* or the *Round Robin* schemes cannot achieve the highest data collection rate.

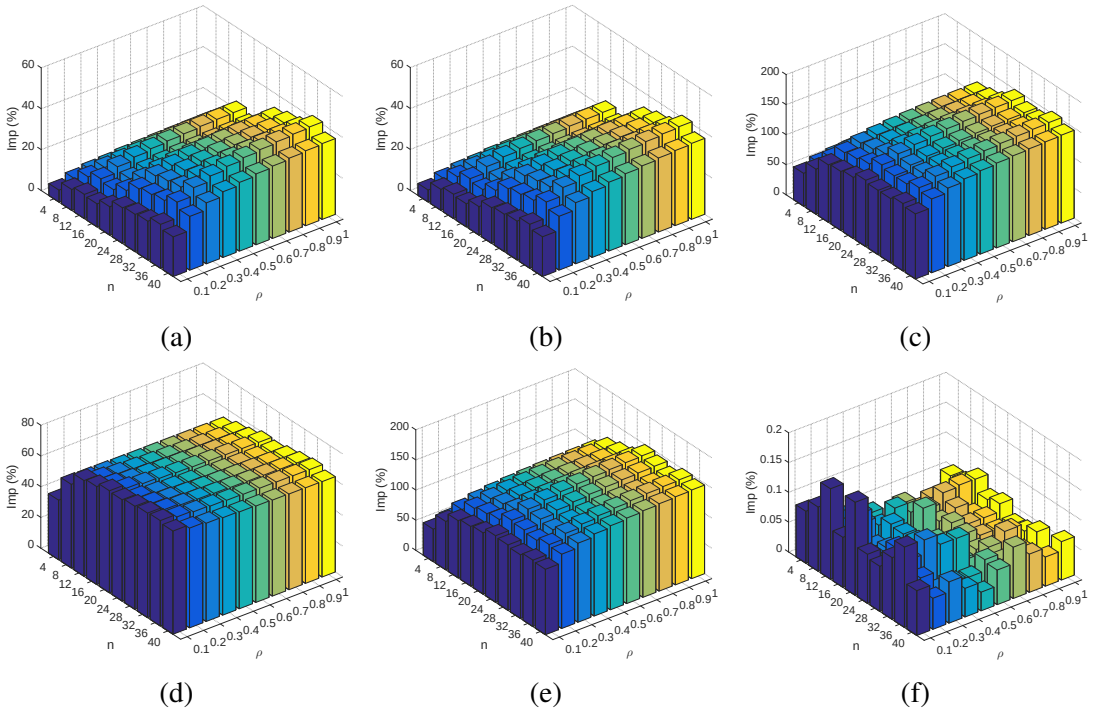

Figure 4.5: Improvement of *ES* scheme over: (a) *Max Energy* scheme; (b) *Round Robin* scheme; (c) *Min CM-CH* scheme; (d) *Min CH-BS* scheme; (e) *Min Listen cost* scheme; (f) *AS* scheme

Compared with the minimum cost based CH selection schemes, the proposed ES scheme achieves a higher improvement. From Figures 4.5(c) and (e), the performance of the *Min CM-CH* scheme is close to the *Min Listen cost* scheme because both schemes focus on intra-cluster cost. The minimum cost-base schemes overlook the energy harvesting dynamics of the IoBT-operated cluster. Though the node with the minimum transmission cost (listening cost, CM-to-CH cost or CH-to-BS cost) is selected as the CH node, due to a lack of sufficient energy, the data collection rate is low.

Figure 4.5(f) demonstrates that the AS scheme achieves almost the same performance compared with the ES scheme. The maximum difference is less than 0.15%. According to Algorithm 4.3 and Proposition 4.3, AS is based on the approximation of the receiving cost. Due to the assumption that each IoBT node individually performs transmission power control, the wireless links between the CH node and CM nodes have stable quality with low Packet Error Rate (PER). The receiving costs have small variation for different links. Thus, AS is validated to be a close approximation to ES in the IoBT-operated cluster.

4.3.4 Overhead

Overhead is an important factor for the IoBT-operated cluster. This subsection considers two kinds of overhead: control message overhead and computational cost.

4.3.4.1 Control Message Overhead

According to Subsection 4.2.2, two types of control message overhead are investigated: node-to-BS and node-to-node overhead.

Node-to-BS overhead is measured as the overall node-to-BS control messages versus the total amount of data the CH node transmits to the BS at each round (Recall that only the CH node transmits the data back to the BS. The CM nodes report the data to the CH). Figure 4.6(a) shows that the node-to-BS overhead ranges from 0.14% to 1.73% with different sizes of the cluster and the data aggregation ratio ρ. Due to the fact that a higher ρ contributes to

a high data collection rate, which can be observed in Figure 4.3, a higher ρ will reduce the node-to-BS overhead.

Node-to-node overhead is measured as the overall node-to-node control messages versus the total amount of data the CM nodes report to the CH node at each round. Figure 4.6(b) indicates that a higher aggregation ratio ρ causes a higher node-to-node overhead. For a given IoBT-operated cluster, a higher aggregation ratio will reduce the data rate of each CM node. Thus, the node-to-node overhead increases monotonically with the aggregation ratio ρ.

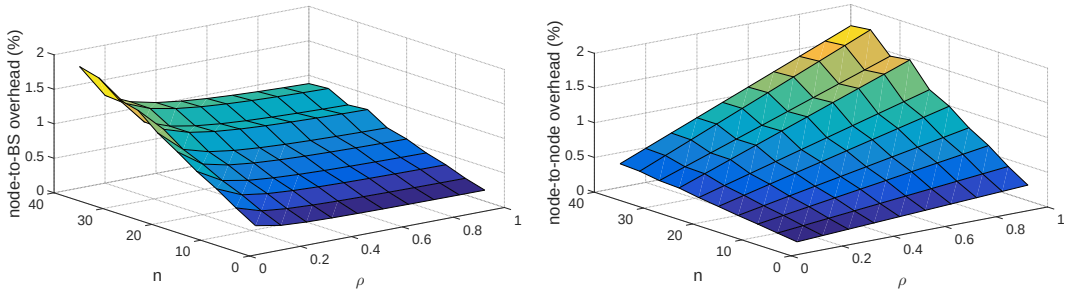

(a) (b)

Figure 4.6: Average control message overhead: (a) node-to-BS overhead; (b) node-to-node overhead

From Figure 4.6, both the node-to-BS and the node-to-node overheads are maintained in an acceptable range (less than 2%). Thus, the proposed methodology achieves low message overhead for an IoBT-operated cluster.

4.3.4.2 Computational Cost

The computational cost is incurred by the CH selection and the lexicographic rate assignment algorithms. In each round, the simulation time cost by the CH selection scheme and the lexicographic rate assignment algorithm is counted. Two CH selection schemes, ES and AS, are evaluated. For comparison, the simulation time of the *Max Energy* and *Round Robin* schemes is also tested. The simulation is performed using MATLAB. A desktop with $3.4\,\mathrm{GHz}$ clock frequency and $16\,\mathrm{GB}$ memory is used for simulation. In order to re-

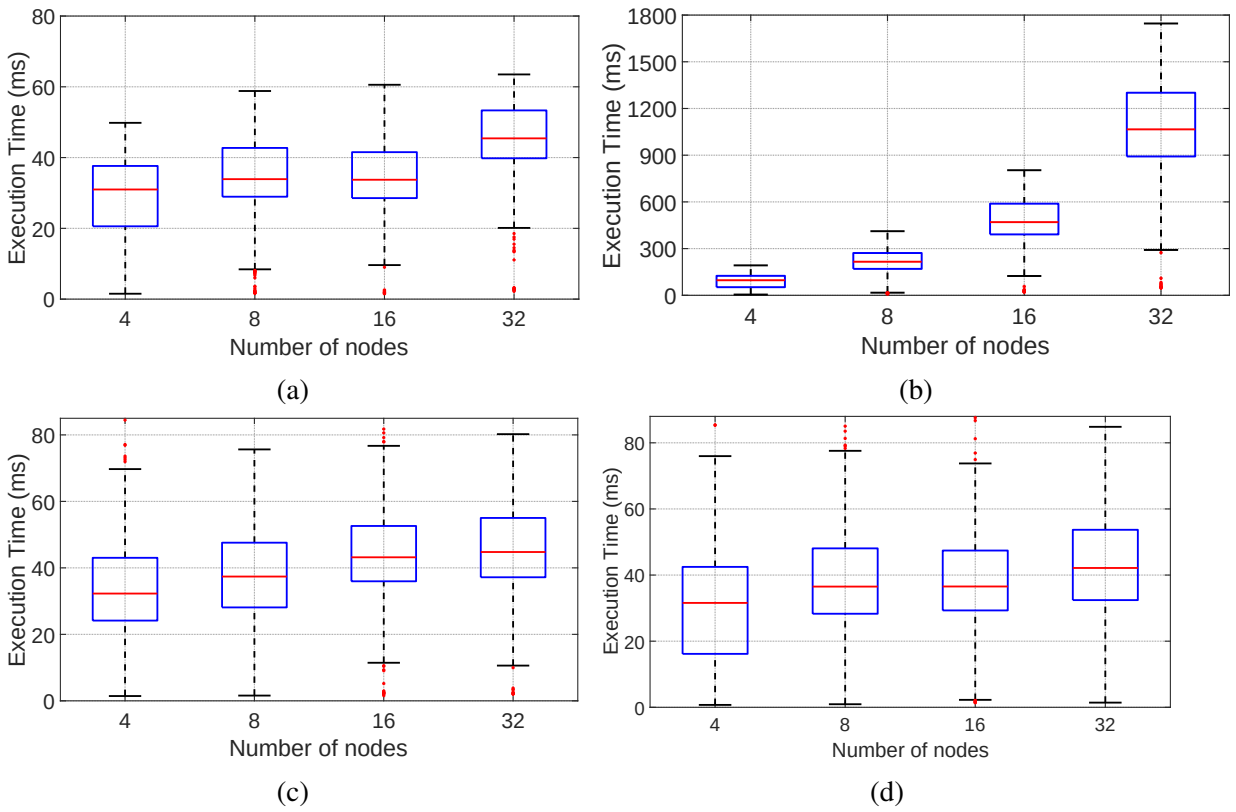

Figure 4.7: Execution time statistics: (a) AS; (b) ES; (c) *Max Energy* scheme; (d) *Round Robin* scheme

duce the impact of background threads, the simulation is repeated for 500 times to conduct statistical analysis.

Figure 4.7 demonstrates the box plot of the ES, AS, *Max Energy* and *Round Robin* schemes in terms of computational cost. AS incurs much less computational cost than ES. The speedup achieved by AS ranges from $3.24X$ to $24.1X$ with different sizes of the cluster. The simulation results are consistent with the computational complexity discussion in Subsection 4.2.2. Compared to the $O(n)$ complexity of AS, ES has $O(n^2)$ complexity so that the simulation time increases dramatically with the cluster size. Compared with ES, AS has much less computational cost and at the same time, achieves almost the same data collection rate.

Figures 4.7(c) and (d) show the execution time of the existing *Max Energy* and *Round Robin* schemes, respectively. The proposed AS has similar average execution time. This is

due to the fact that they all share a similar average complexity of $O(n)$. Compared with the existing CH selection schemes, AS achieves higher data collection rate with comparable computational cost.

From the analysis of computational cost, AS is suitable for IoBT-operated clusters to achieve high data collection rate with restrained computational power.

4.4 Conclusion

In this chapter, a novel adaptive clustering strategy is proposed for IoBT-operated cluster to achieve optimal throughput with varying ambient energy generation. Lexicographic optimal rate assignment is developed to enable each of the clustered IoBT nodes to fully utilize its collected energy. Two CH selection policies, ES and AS, are developed to maximize the cluster throughput by choosing the CH node with the highest data collection rate. The real world solar traces are used to verify the effectiveness of the proposed strategy. Compared with the other schemes, the proposed IoBT-based adaptive clustering achieves consistently higher throughput over all the data aggregation ratio. The data collection rate improvement ranges up to 43%. Compared with ES, AS achieves almost the same throughput but at the same time, incurs much less computational cost. The message overhead of the proposed IoBT-operated clustering is also demonstrated to be low.

CHAPTER 5
COLLABORATIVE IN-NETWORK PROCESSING

With the rapid growth of data being generated in the big data era, in-network processing becomes an important application for networked systems. Empowered with extended lifetime and sustainable operation, IoBT has huge capability in data processing that is not yet fully exploited. To efficiently utilize the computational power of IoBT networks, this chapter focuses on collaborative in-network processing framework to achieve minimized data processing latency.

The rest of the chapter is organized as follows. Section 5.1 introduces in-network processing in IoBT networks. Section 5.2 presents the proposed collaborative in-network processing framework. Section 5.3 details the numeric evaluation results. Section 5.4 concludes the chapter.

5.1 System Overview

Figure 5.1 shows the IoBT network model, which is composed of a Base Station (BS) and n IoBT nodes. $\mathcal{V}$ is defined to be the set of all nodes in the IoBT network. Each IoBT node is within one-hop communication range to the BS. The operation time is divided into slots with a slot size of τ.

5.1.1 Computational Model

A task is represented by $J(L, t_d)$, where L stands for the input data size (in the unit of bits) of the task and t_d is the processing deadline. In this chapter, each task J can be divided into multiple parts and the multiple parts can be processed in parallel at the same time. At the beginning of each slot, a task $J(L, t_d)$ is generated at the BS, as shown in Figure 5.1. The BS will partition the input data L into multiple segments and distribute them to the

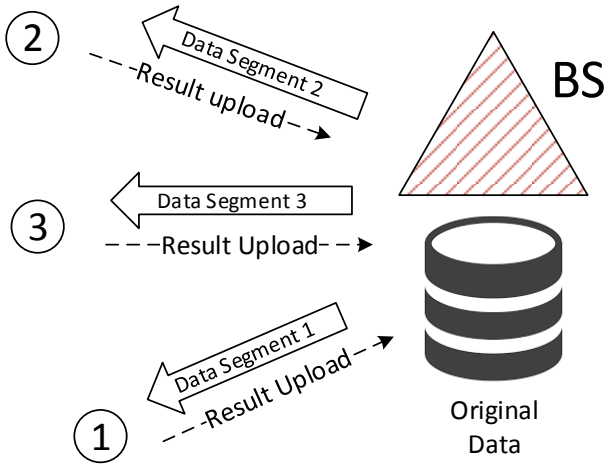

Figure 5.1: IoBT network model

IoBT nodes, as shown in Equation (5.1). $l_k(t)$ denotes the size of the data segment that is assigned to node k in the tth slot.

$$L = \sum_{k \in \mathcal{V}} l_k(t) \tag{5.1}$$

C denotes the average cycles it takes the MCU to process one bit data. C is application dependent and can be measured by off-line profiling [93]. Therefore, for node k, the MCU computing latency d_k^p is shown in Equation (5.2), where f_k stands for the MCU clock frequency. $\mathcal{F}$ denotes the list of tunable frequency of an MCU. When node k finishes data processing, it needs to return the computation result to the BS. ρ is defined to be the ratio between the processed result and the original data segment. ρ depends on the application requirements and is within the range of $[0, 1]$. As shown in Equation (5.3), when node k finishes computing, l'_k is the size of the result that it needs to be transmitted back to the BS.

$$d_k^p(t) = \frac{l_k(t)C}{f_k(t)} \tag{5.2}$$

$$l'_k(t) = \rho l_k(t) \tag{5.3}$$

For node k, the overall latency for processing the data segment includes the time to

receive the segment from the BS, MCU computing time and the time to transmit the result back to the BS, as shown in Equation (5.4). $d_k(t)$ is defined to be the nodal latency for node k in the tth slot. $d_k^r(t)$ and $d_k^u(t)$ refer to the segment download and the result upload latencies, respectively.

$$d_k(t) = d_k^r(t) + d_k^p(t) + d_k^u(t) \tag{5.4}$$

The in-network processing latency d_Σ is defined to be the latency that it takes the IoBT network to finish the data processing. Considering that the BS needs to collect all the results of the processed data segments from the IoBT nodes, the in-network processing latency $d_\Sigma(t)$ in the tth slot is illustrated in Equation (5.5).

$$d_\Sigma(t) = \max_{k \in \mathcal{V}} d_k(t) \tag{5.5}$$

5.1.2 Wireless Communication Model

During the operation of IoBT network, wireless communication is required to distribute the data segments and feedback the computation results. The wireless channel is assumed to be independent and identically distributed (i.i.d) block fading. The wireless channel is static within each time slot but displays variation among different slots. It is assumed that IoBT systems use Frequency Division Multiple Access (FDMA) to communicate with the BS. Based on the Shannon-Hartley function [62], the transmission rate from the sender i to the receiver j at the t slot is illustrated in Equation (5.6). ω stands for the bandwidth and σ is the noise power at the receiver. For the wireless channel between i and j, $h_{i,j}(t)$ represents the channel power gain at the tth slot. p_i^{tx} is the wireless transmit power of the sender i. For a wireless transceiver, a list of discrete transmit power levels are available for

dynamic selection. $\mathcal{P}$ is defined to be the list of available transmit power levels.

$$r_{i,j}(t) = \omega log_2\Big(1 + \frac{h_{i,j}(t)p_i^t(t)}{\sigma}\Big) \tag{5.6}$$

$d_k^r(t)$ denotes the time that it takes node k to receive its data segment from the BS at the tth slot, as shown in Equation (5.7). Similarly, $d_k^u(t)$ refers to the time it takes node k to upload its processing result back to the BS, as shown in Equation (5.8).

$$d_k^r(t) = \frac{l_k(t)}{r_{BS,k}(t)} \tag{5.7}$$

$$d_k^u(t) = \frac{l_k'(t)}{r_{k,BS}(t)} \tag{5.8}$$

5.1.3 Energy Model

A supercapacitor (SC) is used to buffer the harvested energy due to its extremely long cycle life [64]. $s_k(t)$ stands for the energy harvested in the *t*th slot for node k. The maximum capacity of the SC is defined to be B. In the *t*th slot, the usable energy stored in node k is quantified by $b_k(t)$. Due to the SC capacity limitation, $b_k(t)$ is in the range $[0, B]$. $e_k(t)$ denotes the energy expenditure of node k in the tth slot. In order to prevent energy depletion, the energy expenditure $e_k(t)$ is required to be within the range $[0, b_k(t)]$. The energy evolution of an IoBT system is formulated in Equation (5.9).

$$b_k(t) = min\Big\{b_k(t-1) + s_k(t-1) - e_k(t-1), B\Big\} \tag{5.9}$$

During the data processing, the power consumption of the IoBT system depends on the MCU frequency f_k. Dynamic Voltage and Frequency Scaling (DVFS) [36] is a technique that reduces energy dissipation by lowering the processor frequency. According to [62], the power incurred by the MCU processing is illustrated by Equation (5.10), where ϵ refers to the effective switched capacitance of the MCU. For node k, the energy consumption of

MCU computation at the tth slot is quantified by Equation (5.11).

$$p_k^p(t) = \epsilon f_k^3(t) \tag{5.10}$$

$$e_k^p(t) = p_k^p(t) d_k^p(t) \tag{5.11}$$

For node k, the energy consumed by the wireless transceiver is shown in Equation (5.12). The first term stands for the energy consumed by receiving the data segment from the BS, where $p_k^r(t)$ is the power consumption of the transceiver at the receiver mode. The second term accounts for the energy consumed by transmitting the result back to the BS. For node k, the overall energy consumption in the tth slot $e_k(t)$ is a summation of the MCU and the transceiver energy consumption, as shown in Equation (5.13).

$$e_k^t(t) = p_k^r(t) d_k^r(t) + p_k^t(t) d_k^u(t) \tag{5.12}$$

$$e_k(t) = e_k^p(t) + e_k^t(t) \tag{5.13}$$

5.2 Collaborative In-network Processing for IoBT networks

Due to the time-varying nature of ambient energy generation and wireless fading channel, IoBT-operated collaborative in-network processing contains three major problems: 1) task capacity planning; 2) input data partition; and 3) optimal MCU frequency and wireless transmit power selection. The capacity planning provides an upper bound of the feasible input data size for the IoBT network.

Since the selection of the MCU frequency and wireless transmit power will affect the data partition. An iterative optimization framework is proposed to determine the data partition and select the MCU frequency and transmit power. In this framework, a latency-aware data partition algorithm is first presented with a given MCU frequency and wireless trans-

mit power; and then an optimization framework is presented to iteratively optimize the data partition, MCU frequency and transmit power.

5.2.1 Task Capacity Planning

At the beginning of a time slot, each IoBT node needs to perform task capacity planning to derive the maximum feasible data size with a given deadline t_d.

In the tth slot, for each node $k \in \mathcal{V}$, given the usable energy budget $b_k(t)$, the task capacity planning problem is formulated as follows:

$$\hat{l}_k(t) = \max_{f_k(t)\in\mathcal{V}, p_k^t(t)\in\mathcal{P}} l_k(t) \tag{5.14}$$

$$s.t.: \ 0 \leq e_k(t) \leq b_k(t) \tag{5.15}$$

$$0 \leq d_k(t) \leq t_d \tag{5.16}$$

The remaining energy $b_k(t)$ is used as the energy budget. Equations (5.15) and (5.16) represent the energy and latency constraints, respectively.

By combining Equations (5.2), (5.3), (5.7), (5.8), Equation (5.4) is rewritten as:

$$d_k(t) = \frac{l_k(t)}{r_{BS,k}(t)} + \frac{l_k(t)C}{f_k(t)} + \frac{\rho l_k(t)}{r_{k,BS}(t)} \tag{5.17}$$

$g_k(t)$ stands for the equivalent data processing latency for node k with the unit of second per bit, as shown in Equation (5.18). By combining Equations (5.16), (5.17) and (5.18), $l_k^d(t)$ is obtained as the feasible data size limited by the latency constraint, as shown in Equation (5.19).

$$g_k(t) = \frac{1}{r_{BS,k(t)}} + \frac{C}{f_k(t)} + \frac{\rho}{r_{k,BS}(t)} \tag{5.18}$$

$$l_k^d(t) = \frac{t_d}{g_k(t)} \tag{5.19}$$

Similarly, $m_k(t)$ stands for the equivalent energy cost for in-network processing with the unit of joule per bit, as shown in Equation (5.20). By combining Equations (5.11), (5.12), (5.13) and (5.20), $l_k^e(t)$ is derived as the feasible data size limited by the energy constraint, as shown in (5.21).

$$m_k(t) = \epsilon f_k^2(t) C + \frac{p_k^r(t)}{r_{BS,k}(t)} + \frac{\rho p_k^t(t)}{r_{k,BS}(t)} \tag{5.20}$$

$$l_k^e(t) = \frac{b_k(t)}{m_k(t)} \tag{5.21}$$

Since both $l_k^e(t)$ and $l_k^d(t)$ are dependent on the MCU frequency and transmit power, for each pair of MCU frequency $f_k(t)$ and transmit power $p_k^t(t)$, the feasible data size $N_k^t\Big(f_k(t), p_k^t(t)\Big)$ is defined in Equation (5.22).

$$N_k^t\Big(f_k(t), p_k^t(t)\Big) = min\Big\{l_k^d(t), l_k^e(t)\Big\} \tag{5.22}$$

In the tth slot, the maximum feasible data size $\hat{l}_k$ for node k is derived from Equations (5.19) and (5.21). By traversing a two-dimensional searching space of the available MCU frequencies $\mathcal{F}$ and the tunable transmit power levels $\mathcal{P}$, each IoBT system can individually calculate its feasible data size with the computational complexity of $O(|\mathcal{P}||\mathcal{F}|)$, where the operator $|\cdot|$ stands for the number of elements. $F_k(t)$ and $P_k^t(t)$ refer to the MCU frequency and transmit power to achieve maximum data size $\hat{l}_k(t)$ for node k, respectively.

$$\hat{l}_k(t) = \max_{f_k(t)\in\mathcal{V}, p_k^t(t)\in\mathcal{P}} \Big\{N_k^t\Big(f_k(t), p_k^t(t)\Big)\Big\} \tag{5.23}$$

In the tth slot, the overall maximum feasible input data size $\hat{L}(t)$ is shown in Equation (5.24). If the BS has a task whose input data size is larger than $\hat{L}(t)$, it is infeasible for the

IoBT network to finish the data processing within the deadline t_d.

$$\hat{L}(t) = \sum_{k \in \mathcal{V}} \hat{l}_k(t) \tag{5.24}$$

5.2.2 Latency-aware Data Partition

Once the task capacity planning module determines that the task $J(L, t_d)$ is feasible for the IoBT in the tth slot, the BS will partition the input data and dispatch the data segments to the IoBT nodes. This subsection seeks to derive an optimal data partition $\boldsymbol{l}(t) = [l_1(t), ..., l_n(t)]$ to minimize the total in-network processing delay d_Σ. In the tth slot, $\boldsymbol{g}(t) = [g_1(t), ..., g_n(t)]$ and $\boldsymbol{m}(t) = [m_1(t), ..., m_n(t)]$ are defined to be the unit timing cost and unit energy cost for all IoBT nodes, respectively. $\boldsymbol{b}(t) = [b_1(t), ..., b_n(t)]$ refers to the usable energy for all nodes. $\hat{\boldsymbol{l}}(t) = [\hat{l}_1(t), ..., \hat{l}_n(t)]$ represents the maximum feasible segment size derived in the previous subsection. The Latency-aware Data Partition (LDP) problem is formulated as follows:

$$\min_{\boldsymbol{l(t)}} d_\Sigma \tag{5.25}$$

$$s.t.: \ 0 \leq e_k(t) \leq b_k(t) \quad \forall k \in \mathcal{V} \tag{5.26}$$

$$0 < d_\Sigma \leq t_d \tag{5.27}$$

$$l_k(t) \leq \hat{l}_k(t) \quad \forall k \in \mathcal{V} \tag{5.28}$$

$$\sum_{k \in \mathcal{V}} l_k(t) = L \tag{5.29}$$

The objective is to minimize the in-network processing latency within the energy and timing constraints, as shown in Equations (5.26) and (5.27), respectively. Equations (5.28) and (5.29) shows the constraints of the data segment sizes.

Algorithm 5.1: Latency-aware Data Partition (LDP)

Input : $\boldsymbol{b}(t)$, $\boldsymbol{g}(t)$, $\boldsymbol{m}(t)$, $\hat{\boldsymbol{l}}(t)$;
L, t_d;
Output: $\boldsymbol{l}(t)$;
Init : $\boldsymbol{l}(t)$, $\boldsymbol{d}(t)$, $\tilde{\boldsymbol{l}}(t)$, $\tilde{\boldsymbol{d}}(t) \leftarrow \mathbf{0}$;
$\mathcal{A} \leftarrow \varnothing$;
$L_{rem} \leftarrow L$;
while $\mathcal{A} \neq \mathcal{V}$ **do**
  for $i = 1; i \leq |\mathcal{V}|; i++$ **do**
    if $i \notin \mathcal{A}$ **then**
      $\tilde{l}_i(t) \leftarrow l_i(t)$;
      $\tilde{d}_i(t) \leftarrow \tilde{d}_i(t) + \delta$;
      $\Delta l_i(t) \leftarrow \min\left\{\frac{\delta}{g_i(t)}, L_{rem}\right\}$;
      $\tilde{l}_i(t) \leftarrow \tilde{l}_i(t) + \Delta l_i(t)$;
      if *check*($\tilde{l}_i(t)$, $\tilde{d}_i(t)$, L_{rem}) == *TRUE* **then**
        $l_i(t) \leftarrow \tilde{l}_i(t)$;
        $d_i(t) \leftarrow \tilde{d}_i(t)$;
        $L_{rem} \leftarrow L_{rem} - \Delta l_i(t)$
      else
        $\mathcal{A} \leftarrow \mathcal{A} \cup \{i\}$;
      end
    end
  end
end
Function *check*($\tilde{l}_i(t)$, $\tilde{d}_i(t)$, L_{rem})
  valid $\leftarrow$ TRUE;
  if $L_{rem} == 0$ **or** $\tilde{d}_i(t) > t_d$ **or** $\tilde{l}_i(t) > \hat{l}_i(t)$ **then**
    valid $\leftarrow$ FALSE;
  end
  return *valid;*

Algorithm 5.1 is developed to solve the latency minimization problem. In Algorithm 5.1, $\mathcal{A}$ denotes the set containing all the IoBT nodes with saturated data segment size, and L_{rem} refers to the remaining number of bits that can be assigned to the data segments. Equations (5.5) and (5.25) show that the latency minimization problem is essentially an

minmax fairness problem. Initially, $\mathcal{A}$ is an empty set. L_{rem} is initialized to be the original data size L. LDP starts with a zero data size for each data segment, and then iterates through all the IoBT nodes, fairly incrementing the processing latency of all the nodes with a step size of δ. $\Delta l_i(t)$ stands for the data size increase for node i at the tth slot, which varies with the processing time. For the tth slot, $\tilde{\boldsymbol{l}}(t) = [\tilde{l}_1(t), ..., \tilde{l}_n(t)]$ refers to the segment sizes that will be incremented with $\Delta l_i(t)$ in each iteration, as shown in line 13 of Algorithm 5.1. $\tilde{\boldsymbol{d}}(t) = [\tilde{d}_1(t), ..., \tilde{d}_n(t)]$ denotes the corresponding latency vector.

The *check* function (line 24-29) detects whether any of the following conditions occur with the augmentation of data size.

1) The data segment size exceeds the maximum feasible size.

2) The nodal latency is not within the deadline.

3) The remaining data size L_{rem} is zero.

If any of these three conditions is satisfied, then the data segment size for node i, $l_i(t)$, is saturated. It is not valid to further increment the data segment.

In order to prove the optimality of Algorithm 5.1, some useful terms are first defined. Then, Proposition 5.1 demonstrates the inherent properties of Algorithm 5.1, which will be further utilized to validate Theorem 5.1.

Definition 5.1 In the tth slot, for an IoBT node k with the usable energy $b_k(t)$ and an allocated energy expenditure $e_k(t)$: (1) if $e_k(t) \in [b_k(t) - \zeta_e, b_k(t)]$ for arbitrary $\zeta_e > 0$, then node k is *energy throttled* in the tth slot; (2) if there exists an $\xi_e > 0$, $e_k(t) \in [0, b_k(t) - \xi_e]$, then node k is *energy sufficient* in the tth round.

Definition 5.2 In the tth slot, for an IoBT node k with the nodal latency $d_k(t)$ and the task deadline t_d: (1) if $d_k(t) \in [t_d - \zeta_d, t_d]$ for arbitrary $\zeta_d > 0$, then node k is *latency throttled* in the tth slot; (2) if there exists an $\xi_d > 0$, $d_k(t) \in [0, t_d - \xi_d]$, then node k is *latency sufficient* in the tth round.)

Definition 5.3 For a partition $\boldsymbol{l}$, $Q_t^{\boldsymbol{l}}$ is defined to be the set containing all the nodes that are either energy throttled or latency throttled in the tth round. These nodes in the set $Q_t^{\boldsymbol{l}}$

are considered to be *resource throttled* for the partition $\boldsymbol{l}$. Similarly, $\bar{Q}_t^{\boldsymbol{l}}$ denotes the set of the *resource sufficient* nodes that are both energy sufficient and latency sufficient.

Considering the step size δ can be arbitrarily small, Proposition 5.1 is obtained. Proposition 5.2 is derived by combing Definitions 5.1-5.3. Based on the propositions, the proposed Algorithm 5.1 is verified to be optimal. The detailed proof of Proposition 5.1 and Theorem 5.1 are in Appendix C.

Proposition 5.1: Let $\boldsymbol{l}(t) = [l_1, ..., l_n(t)]$ be a data segment partitioned by Algorithm 5.1 in the tth slot. $\boldsymbol{d}(t) = [d_1, ..., d_n(t)]$ is the corresponding nodal latency for each IoBT system. If $Q_t^{\boldsymbol{l}} \neq \varnothing$ and $\bar{Q}_t^{\boldsymbol{l}} \neq \varnothing$, then: 1) for any nodes j and k, if $j \in Q_t^{\boldsymbol{l}}$ and $k \in \bar{Q}_t^{\boldsymbol{l}}$, then $d_k(t) \geq d_j(t)$; 2) for any nodes x and y, if $x, y \in \bar{Q}_t^{\boldsymbol{l}}$, then $d_k(t) = d_j(t)$; and 3) for any node k, if $k \in \bar{Q}_t^{\boldsymbol{l}}$, then $d_k(t) = \max_{j \in \mathcal{V}} d_j(t)$.

Proposition 5.2: Let $\boldsymbol{l}(t) = [l_1(t), ..., l_n(t)]$ be a data segment partitioned by Algorithm 5.1 in the tth slot. For any node $k \in \mathcal{V}$, if there exists another feasible data partition $\dot{\boldsymbol{l}}(t) = [\dot{l}_1(t), ..., \dot{l}_n(t)]$ and $l_k(t) \leq \dot{l}_k$, then node $k \in \bar{Q}_t^{\boldsymbol{l}}$.

Theorem 5.1: Algorithm 5.1 derives the optimum partition for the LDP problem.

For each IoBT node, the maximum steps of increment in Algorithm 5.1 is $\frac{t_d}{\delta}$, which refers to augmenting the latency until the deadline t_d is reached. For an IoBT network with n nodes, the maximum time complexity of Algorithm 5.1 is $O(\frac{nt_d}{\delta})$.

5.2.3 Joint Computation and Transmission Optimization

In the previous subsection, the optimal data partition is derived with a given MCU frequency and transmit power. This part seeks to select an optimal combination of MCU frequency and transmit power with the data partition given by Algorithm 5.1.

In the tth slot, for any node $k \in \mathcal{V}$ with its data segment size of $l_k(t)$, nodal latency of $d_k(t)$, energy expenditure $e_k(t)$ and usable energy $b_k(t)$, the optimal MCU frequency and

transmit power selection is formulated as follows:

$$\min_{f_k \in \mathcal{F}, p_k^t(t) \in \mathcal{P}} d_k(t) \tag{5.30}$$

$$s.t.: \ 0 \leq e_k(t) \leq b_k(t) \quad \forall k \in \mathcal{V} \tag{5.31}$$

According to Equation (5.17), with a given segment size $l_k(t)$ in the tth slot, the nodal latency $d_k(t)$ and energy consumption $e_k(t)$ of node k depend on the MCU frequency $f_k(t)$ and wireless transmit power $p_k^t(t)$. By traversing all the feasible combinations of the MCU frequency $f_k(t)$ and wireless transmit power $p_k^t(t)$, the optimal solution can be found. $f_k^*(t)$ and $p_k^{t*}(t)$ stands for the optimal MCU frequency and wireless transmit power, respectively. $\boldsymbol{f^*}(t) = [f_1^*(t), ..., f_n^*(t)]$ and $\boldsymbol{p^{t*}}(t) = [p_1^{t*}(t), ..., p_n^{t*}(t)]$ represent the optimal MCU frequency and transmit power vectors, respectively.

For an IoBT node, the maximum time complexity to solve Equation (5.30) is $O(|\mathcal{F}||\mathcal{P}|)$. Considering an IoBT network with n nodes, the complexity to find optimal MCU frequency and transmit power for the entire IoBT network is $O(n|\mathcal{F}||\mathcal{P}|)$.

5.2.4 Iterative Optimization Framework

Figure 5.2 is an overview of the iterative optimization framework. At the beginning of the tth slot, each IoBT node performs capacity planning and report the results to the BS, which provides the BS the maximum feasible data size $\hat{\boldsymbol{l}}(t) = [\hat{l}_1(t), ..., \hat{l}_n(t)]$. With the received the information, the BS iteratively performs LDP and Joint Computation and Transmission Optimization (JCTO) for u iteration.

During the iteration, both LDP and JCTO modules are capable of reducing the latency. Therefore, the overall in-network processing latency d_Σ decreases monotonically with the iteration number u. The proposed iteration framework minimizes the overall latency considering the iteration number u can be arbitrarily large.

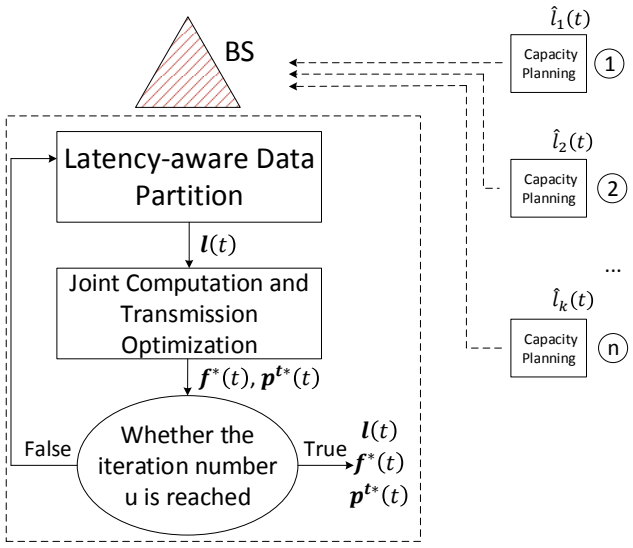

Figure 5.2: An overview of the iterative optimization framework

During the optimization process, each IoBT node performs capacity planning in parallel. Thus, in each slot, the computational complexity for every IoBT node is $O(|\mathcal{P}||\mathcal{F}|)$. The rest of the computation is performed in the BS. The computational overhead in the BS is $O\big(un(\frac{t_d}{\delta} + |\mathcal{P}||\mathcal{F}|)\big)$.

5.3 Evaluation

5.3.1 Simulation Setup

A MATLAB-based simulation is implemented to evaluate the proposed collaborative in-network processing framework. The simulation parameters are detailed in Table 5.1. A 48-hour energy harvesting trace [71] is used to emulate the ambient energy generation. All the evaluation results are the average values of the 48-hour operation.

1) IoBT Network: A circle with radius R is emulated as the deployment field of the IoBT network. The BS is located at the center of the circle. The IoBT node positions are randomly generated within the circle.

2) Wireless Communication: The channel power gain between the sender i and the receiver j, $h_{i,j}$, is emulated using Equation (5.32), where the small-scale fading channel

Table 5.1: Simulation Parameters

Parameters	**Description**
Field radius R	$150\,\mathrm{m}$
Initial energy of each node	$0.5\,\mathrm{J}$
Energy capacity	$B = 10\,\mathrm{J}$
Slot time	$\tau = 10\,\mathrm{s}$
Deadline	$t_d = 10\,\mathrm{s}$
Bandwidth	$\omega = 1\,\mathrm{MHz}$ [94]
Path-loss constant	$g_0 = 10^{-4}$ [85]
Path-loss exponent	$\theta = 4$ [91]
Reference distance	$\chi_0 = 1\,\mathrm{m}$
Average MCU cycles to process one bit	$C = 738\,\mathrm{cycles/bit}$ [94]
MCU effective switch capacitance	$\epsilon = 10^{-28}$ [94]
Noise power	$\sigma = -105\,\mathrm{dBm}$ [44]
Photovoltaic cell size	$H = 2.5\,\mathrm{cm}^2$
Photovoltaic cell conversion efficiency	$\eta =$10% [36]

power gain $\gamma_{i,j}$ is exponentially distributed with a mean of 1. g_0 and θ represent the path-loss constant and the path-loss exponent, respectively. χ_0 refers to the reference distance. $\chi_{i,j}$ denotes the distance between the sender i and the receiver j. This wireless channel model and the corresponding simulation parameters come from the existing literature [94]. The available transmit power list $\mathcal{P}$ ranges from $5\,\mathrm{dBm}$ to $30\,\mathrm{dBm}$ with a step size of $5\,\mathrm{dBm}$.

$$h_{i,j} = \gamma_{i,j} 10^{\frac{g_0}{10}} \left(\frac{\chi_0}{\chi_{i,j}}\right)^{\theta} \tag{5.32}$$

3) MCU Computation: The tunable MCU frequency $\mathcal{F}$ ranges from $200\,\mathrm{MHz}$ to $1\,\mathrm{GHz}$ with a step size of $200\,\mathrm{MHz}$.

4) Energy Harvesting: The simulation emulates a PV cell with size H and conversion efficiency η to convert the light irradiance to the electrical energy using the method introduced in [36]. Real world solar irradiance trace [71] is used to generate the energy harvesting profile. To account for the deviation of harvested power caused by the node physical location, the harvested power is adjusted by a randomly generated amount between -15%

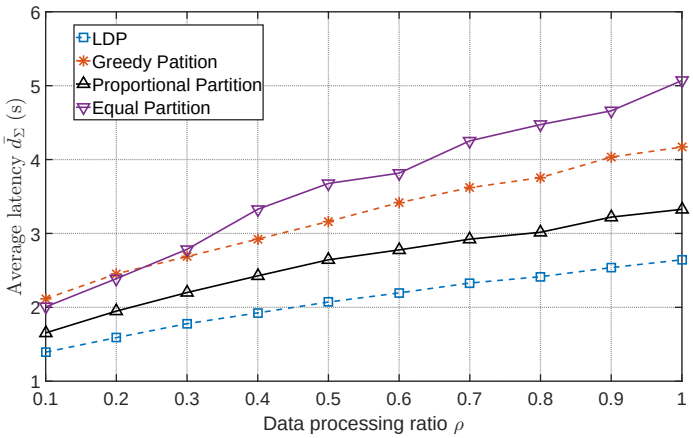

Figure 5.3: Average latency with different data processing ratio ρ ($L = 10\,\mathrm{Mbits}$ and $n = 10$)

and 15% of the baseline. The IoBT network is assumed to operate from 8:00 A.M. to 5:00 P.M. when solar energy is available.

5) Benchmark Algorithms: To compare with the proposed latency-aware data partition, several data partition algorithms are introduced below. The following algorithms are widely used in the area of distributed and parallel computing [63].

(1) Input data is partitioned to greedily fill the capacity of the IoBT nodes with higher usable energy (referred to as *greedy partition* scheme).

(2) Input data is equally partitioned to n segments, wherein n refers to the number of nodes in the IoBT network (referred to as *equal partition* scheme).

(3) The partitioned data segments are proportional to the remaining energy of each IoBT system (referred to as *proportional partition* scheme).

5.3.2 Data Partition

In this subsection, the performance of data partition schemes is evaluated. To make fair comparison, all the schemes stick to a fixed pair of MCU frequency ($800\,\mathrm{MHz}$) and transmit power ($15\,\mathrm{dBm}$) for each IoBT node in the simulations. For each tested data partition algorithm, capacity planning is performed at the beginning of each slot. If a task is rejected by the capacity check, the latency of that task is considered to be the deadline t_d.

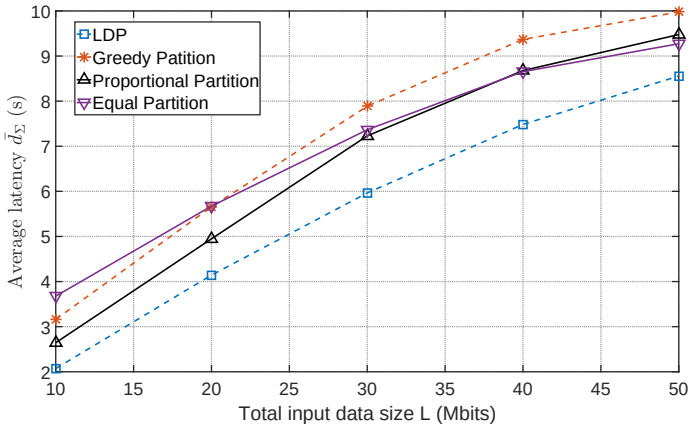

Figure 5.4: Average latency with different input data size L ($\rho = 0.5$ and $n = 10$)

First, investigation is conducted on the performance of the proposed LDP scheme and the other reference schemes with different data processing ratio ρ. The results are quantified in Figure 5.3. Figure 5.3 shows that the proposed LDP achieves the lowest average latency $\bar{d}_\Sigma$ over all the range of the data processing ratio ρ. Compared with the greedy partition scheme, LDP reduces the overall latency by 33.79% to 37.09%. Compared with the proportional partition scheme, the latency reduction achieved by LDP ranges from 15.75% to 21.63%. Compared with the equal partition scheme, LDP lowers the latency by 30.53% to 47.86%.

Then, the focus is on the variation of the overall latency with regard to the total input data size L. Figure 5.4 shows the overall in-network processing latency with different input size L, in which the proposed LDP achieves the lowest latency with different input size L ranging from $10\,\mathrm{Mbits}$ to $50\,\mathrm{Mbits}$. With a larger input size L, a relatively longer time is required for the IoBT network to finish the collaborative in-network processing, leading to a higher latency. Compared with the greedy partition scheme, the latency reduction achieved by the proposed LDP ranges from 14.26% to 34.47%. Compared with the proportional partition scheme, the improvement of LDP is from 9.71% to 21.63%. Compared with the equal partition scheme, LDP reduces the overall latency by 7.73% to 43.65%.

Another important factor is the IoBT network size n. Figure 5.5 focuses on the overall latency performance with different IoBT network size n. Compared with the benchmark

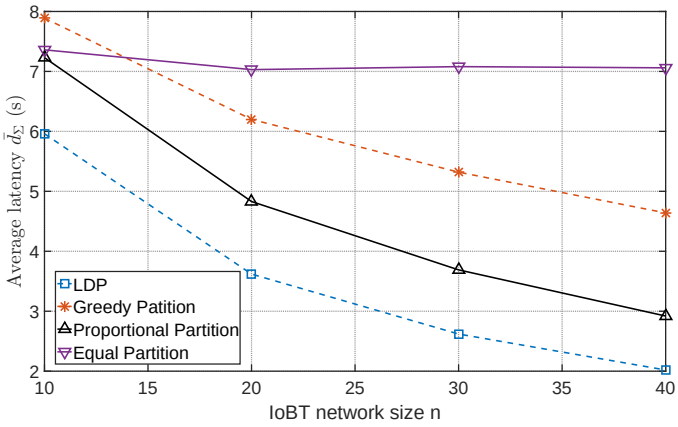

Figure 5.5: Average latency with different IoBT network size n ($\rho = 0.5$ and $L = 30\,\text{Mbits}$)

schemes, the proposed LDP achieves the lowest latency with different network size n. With more IoBT nodes participating the collaborative in-network processing, the overall latency is reduced.

According to the simulation results in Figures 5.3, 5.4 and 5.5, the proposed LDP achieves consistently lower latency with various configurations (data processing ratio ρ, overall input data size L and IoBT network size n). In the greedy partition scheme, the high-energy nodes are assigned with data segments of larger size. However, higher remaining energy does not guarantee larger capacity of data processing. It is likely that a node far-away from the BS may have high energy budget but low data processing capacity in some time slots due to the high transmission cost required. Therefore, the greedy partition scheme cannot maintain low overall latency for IoBT networks. The equal partition scheme splits the data fairly and each data segment has the same size. It does not consider energy budget, or IoBT power consumption. However, for nodes with low energy budget, it is not preferable for them to process data segments with the same size as that of the other nodes with high remaining energy. This explains the high latency of the equal partition scheme with a large IoBT network size n in Figure 5.5. In the proportional partition scheme, the size of each data segment is proportional to the energy budget of the designated IoBT node. Energy budget alone cannot determine the data processing capability. The wireless transmission cost and MCU power consumption also impacts the data segment size that an

IoBT node can process. Therefore, it fails to achieve the optimal latency for collaborative in-network processing. For IoBT networks, it is desired to take into account both energy budget and energy cost (incurred by wireless transceiver and MCU) when partitioning the input data. The proposed LDP is capable of segmenting the data based on the ambient energy generation, wireless fading channel and MCU power consumption. Figures 5.3, 5.4 and 5.5 verify that the proposed LDP achieves the lowest overall latency with various configuration in data processing ratio, total input data size and network size.

5.3.3 Iterative Optimization Framework

In this subsection, the performance of the proposed iterative optimization framework is investigated. Figure 5.6 demonstrates the average latency $\bar{d}_{\Sigma}$ of the proposed iterative optimization framework with the iteration number $u = 3$. The latency of two fixed configurations are also measured for comparison. The first configuration, referred to as the *fixed-1 scheme*, has the transmit power $p^t = 15\,\mathrm{dBm}$ and the MCU frequency $f = 800\,\mathrm{MHz}$. Similarly, the second setup has the transmit power $p^t = 25\,\mathrm{dBm}$ and the MCU frequency $f = 400\,\mathrm{MHz}$ which is referred to as the $fixed-2$ scheme. For fair comparison, LDP is used as the partition algorithm in all the test cases. Figure 5.6 shows that the proposed iterative optimization framework achieves the lowest average latency. Compared with the fixed-1 scheme, the improvement ranges from 14.16% to 29.51%. Compared with the fixed-2 scheme, the latency reduction ranges from 17.15% to 34.41%.

Imp is defined to be the improvement achieved by the proposed iterative optimization framework over the other schemes, as shown in Equation (5.33). Figure 5.7[1] details the improvement achieved by the iterative optimization framework over various configuration of input data size L and data processing ratio ρ. Compared with the fixed-1 scheme, the improvement ranges from 7.27% to 33.40%. Compared with the fixed-2 scheme, the latency reduction ranges from 17.15% to 37.16%. The evaluation results shown in Figures

[1] In Figure 5.7, the IoBT network size n is 20.

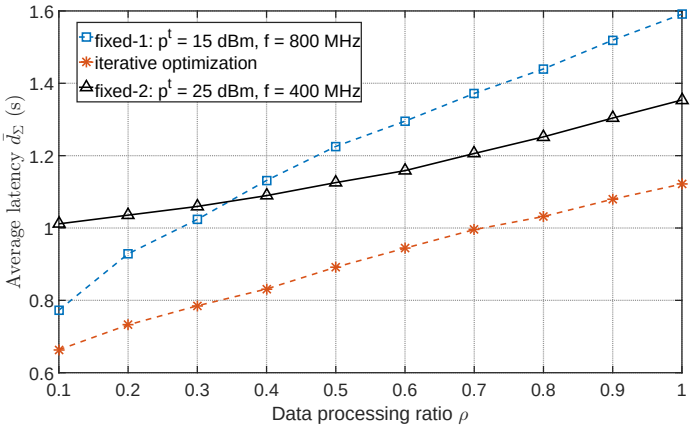

Figure 5.6: Average latency $\bar{d}_\Sigma$ with different schemes ($n = 20$, $u = 3$ and $L = 10\,\mathrm{Mbits}$)

5.6 and 5.7 verify the effectiveness of the proposed iterative optimization framework. By iteratively performing LDP and JCTO, the proposed method minimizes the overall latency by deriving the optimal data segment size, MCU frequency and transmit power for each IoBT node.

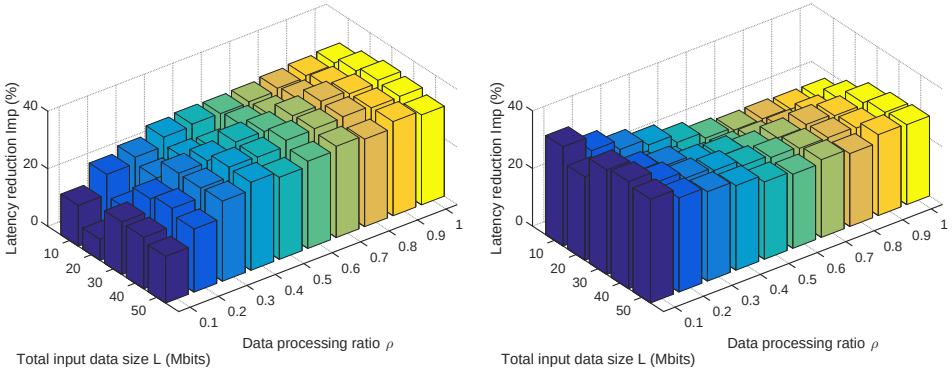

(a) (b)

Figure 5.7: Improvement of the iterative optimization framework over: (a) fixed-1 scheme ($p^t = = 15\,\mathrm{dBm}$ and $f = 800\,\mathrm{MHz}$); (b) fixed-2 scheme ($p^t = = 25\,\mathrm{dBm}$ and $f = 400\,\mathrm{MHz}$)

$$Imp = \frac{\bar{d}_\Sigma(other\ scheme) - \bar{d}_\Sigma(iterative\ optimization)}{\bar{d}_\Sigma(other\ scheme)} \tag{5.33}$$

The iteration number u plays a vital role in the proposed method. Theoretically, a large u can guarantee the optimality of the algorithm. However, high computational cost will be incurred with a large u. According to the complexity analysis in Subsection 5.2.4, the

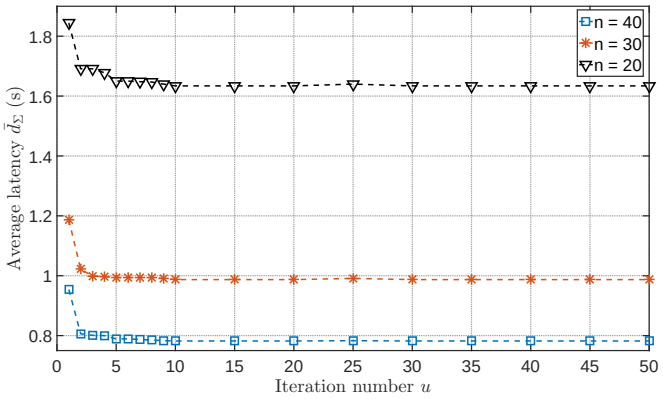

Figure 5.8: Average latency $\bar{d}_\Sigma$ with different iteration number u ($\rho = 0.5$ and $L = 30\,\mathrm{Mbits}$)

overall computational cost of the proposed method is proportional to the iteration number u. To determine the appropriate number of iteration, the change of average latency $\bar{d}_\Sigma$ with iteration number u is first plotted in Figure 5.8 for three different network sizes with an input data size of $30\,\mathrm{Mbits}$ and a data processing ratio ρ of 0.5. Figure 5.8 shows that the average latency $\bar{d}_\Sigma$ drops rapidly with the increase of the iteration number u at the beginning. After 10 iterative optimizations, the average latency $\bar{d}_\Sigma$ converges to an asymptotically minimum value. To take into account of the potential variation of a wide range of simulation setup, the average latency at 50 iterations is used as the asymptotically minimum latency $\hat{d}_\Sigma$ for a more thorough simulation described below.

To further investigate the performance variation with iteration number u for different data sizes and processing ratios, latency ratio λ is defined to be the average latency at iteration number u versus the asymptotically minimum latency $\hat{d}_\Sigma$. When the latency ratio λ is close to 1, it indicates that the latency $\bar{d}_\Sigma(u)$ with u iterative optimization is approaching the minimum latency $\hat{d}_\Sigma$.

$$\lambda = \frac{\bar{d}_\Sigma(u)}{\hat{d}_\Sigma} \tag{5.34}$$

Figure 5.9[2] demonstrates the variation of latency ratio λ with the total input data size

[2]In Figure 5.9, the network size n is 20.

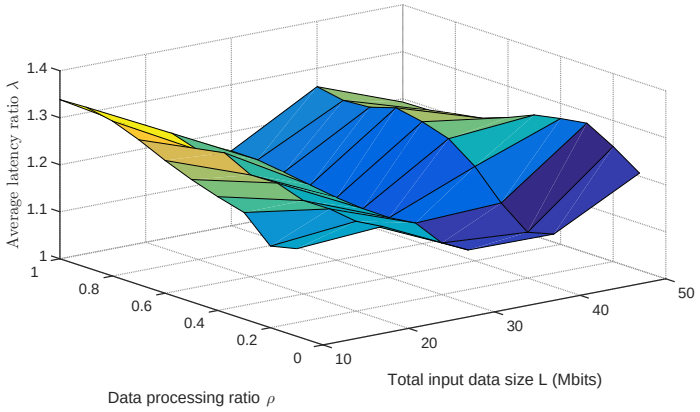

(a)

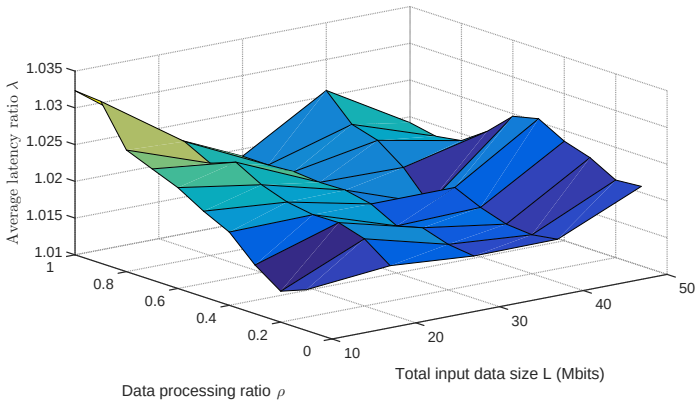

(b)

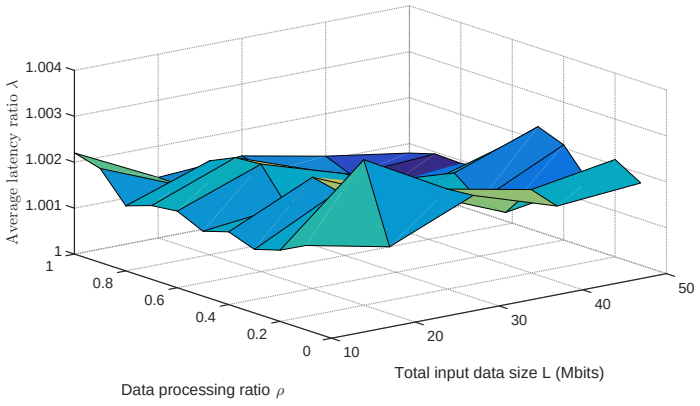

(c)

Figure 5.9: Latency ratio λ with different iteration numbers: (a) $u = 1$; (b) $u = 2$; (c) $u = 3$

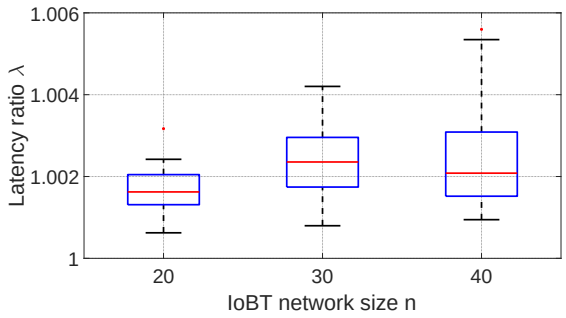

Figure 5.10: Latency ratio λ with 3 iterative optimization ($u = 3$)

L and the data processing ratio ρ. Figures 5.9(a)-(c) show that, with the initial increase of iteration number u, the latency ratio λ drops significantly. When the iteration number u is 3, the maximum latency ratio λ is less than 1.003, which means the latency with 3 iterative optimizations is very close to the minimum latency.

Figure 5.10 shows a statistical analysis of the latency ratio λ with different network size n. The box plot of Figure 5.10 covers the test configurations with different data processing ratio ρ, which ranges from 0 to 1 with a step size of 0.1, and a total input data size L from $10\,\text{Mbits}$ to $50\,\text{Mbits}$ with a step size of $10\,\text{Mbits}$. Figure 5.10 reveals that, with three iterative optimizations, the overall latency is sufficiently close to the optimal latency. The maximum latency ratio λ is less than 1.006. Therefore, it does not need a larger iteration number u to further reduce latency.

5.4 Conclusion

In this chapter, a collaborative in-network processing framework is proposed for IoBT networks to achieve minimum latency with dynamic ambient energy generation. Capacity planning is performed at the beginning of each slot to quantify the maximum feasible input data size for the IoBT network to finish within the deadline. A Latency-aware Data Partition (LDP) scheme is developed to split the input data into small-sized segments and enable collaborative in-network processing. Then, a Joint Computation and Transmission Optimization algorithm is developed to reduce latency by dynamically selecting the op-

timal MCU frequency and transmit power. By iteratively performing the latency-aware data partition and the joint optimization algorithm, the proposed in-network processing framework minimizes the overall latency. The real world solar traces are used to evaluate the proposed method. Compared with the existing schemes, the proposed collaborative in-network processing framework achieves consistently lower latency over different data processing ratios, input data sizes and network sizes. The latency reduction achieved by the proposed method is about 30%. The simulation results also show that after three iterative optimizations, the overall latency is almost the same as the optimal latency. The proposed method provides a viable collaborative in-network processing framework for the IoBT networks with renewable energy source.

CHAPTER 6
CONCLUSIONS AND FUTURE WORK

6.1 Conclusions

This thesis focuses on energy efficient operation in IoBT systems and IoBT-operated networks. Several resource management frameworks are presented to provide sustainable operation over the varying ambient energy and fading wireless channels at the both node and network levels.

At the node level, power managers are designed to minimize the internal energy loss of energy storage devices and improve energy efficiency of IoBT systems. In Chapter 2, a charge redistribution-aware power manager is developed to minimize the redistribution loss of SCs. The power manager comprises an SC simulator that can be used to quantify the long term charge redistribution loss in the SC-operated energy harvesting systems and an eager scheduling based task scheduler to maintain a relatively balanced internal voltage between the main branch and the delay branch of an SC. Compared with the existing strategies, the redistribution-aware power manager lowers the charge redistribution loss by 71%.

Then, in Chapter 3, a novel Predictive Power Management (PPM) framework is proposed. The PPM framework consists of optimal working point, Deviation-aware Predictive Energy Allocation (D-PEA) and Energy efficient Transmission Power Controller (ETPC). The optimal working point captures the hardware features of IoBT system and guarantees minimum power loss. By predictively budgeting the usable energy and using the optimal working point as a set-point, PPM mitigates the prediction error so that both power failure and system power loss are minimized. The ETPC module improves energy efficiency by dynamically choosing optimal transmit power with minimum energy consumption. Compared with the previous power managers, PPM achieves 15% reduction in system power

loss.

At the network level, resource managers are developed to enable collaborative operation for IoBT networks. In Chapter 4, a clustered data collection framework is developed to achieve high and fair data collection rate for IoBT networks. In the data collection framework, a lexicographic rate allocation algorithm is designed so that each IoBT node can fully utilize the scavenged energy and achieve optimal data collection rate, and a CH selection scheme is presented to select the optimal CH by traversing all the possible CH candidates in the cluster. Both theoretical proof and numeric evaluation are provided to validate the optimality of the proposed clustered data collection framework. Compared with the existing strategies, the proposed method enables up to 43% higher data collection rate. Moreover, an approximation-based CH selection scheme is developed based on the inherent power consumption features of the lexicographic rate assignment, which has been demonstrated to have similar data collection rate as that of the optimal CH selection scheme at a much lower computational cost.

In addition, in Chapter 5, a collaborative in-network processing framework is developed to utilize the computational power of IoBT networks. A Latency-aware Data Partition (LDP) algorithm is designed to split the input data into small-sized segments and then distribute the segments to the IoBT nodes. Then, a Joint Computation and Transmission Optimization (JCTO) algorithm is proposed to reduce the nodal latency of each IoBT node by selecting the optimal MCU frequency and transmit power. By iteratively perform LDP and JCTO, the overall in-network processing latency is minimized. Compared with the existing methods, the proposed in-network processing framework reduces the data processing latency by 30%.

6.2 Future Work

In this subsection, potential future work related to IoBT and IoBT-operated networks is discussed.

To begin with, it is important to design power management strategies for IoBT systems powered by novel renewable energy sources. With the development of energy harvesting technology and low power electronics, energy can be harvested from almost everywhere, such as human kinetic [95, 96] and Radio Frequency (RF) signal [18]. It is essential to characterize the novel renewable energy sources and then design customized power managers to fully utilize the harvested energy.

In addition, it is desired to incorporate emerging communication and computation technologies into the design of IoBT systems and design novel power managers. For example, Non-Volatile Random Access Memory (NVRAM) [97] is an alternative to the existing volatile memory. Compared with the existing Dynamic Random Access Memory (DRAM), NVRAM provides similar read latency and at the same time, is capable of persistent data storage. In contrast, the existing DRAM loses all the data when it is shutdown. With NVRAM, IoBT systems is enhanced with data persistency, even in the sleep and shutdown modes. Considerable energy is saved by skipping the unnecessary data migration. The advanced communication technologies in 5G [1] (such as spectrum sharing [98], Software Defined Networking [99], and so on) enable high transmission rate and low latency for IoBT systems. Novel power managers can be developed to achieve high energy efficiency with the emerging communication and computation technologies.

At the network-level, resource management needs to be extended to hybrid networks where IoBT nodes co-exist with conventional battery-operated nodes. IoBT nodes have prolonged lifetime but unstable energy budget from time to time. On the other hand, battery-operated nodes have finite operation time but countable energy budget. To achieve long-term and sustainable operation of hybrid networks, many factors need to be considered to design an efficient resource management frameworks, such as the node type (IoBT node or battery-operated node), application requirements, network topology and so on.

Appendices

APPENDIX A

PROOF FOR CHAPTER 3

A.1 Proof of Lemma 3.1

It is shown in the previous literature [100] that the MOSFET resistance R_{SW1} and R_{SW2} have the same value. Thus, the DC-DC power consumption of the buck mode is simplified to Equation (A.1). In the buck mode, the ripple current ΔI, shown in Equation (A.2), increases monotonically with V_{sc}. Thus, the DC-DC power consumption P_{buck} shares the same monotonicity. Equation (3.2) shows that the SC leakage power P_{leak} also increases with the terminal voltage V_{sc}. Overall, the entire system power loss P_{loss} increases monotonically with the terminal voltage V_{sc} in the buck mode.

$$\begin{aligned} P_{buck} = I_{out}^2[R_L + R_{SW1} + R_{SW4}] + \frac{(\Delta I)^2}{12}[R_L + R_{SW1} + R_{SW4} + R_C] \\ + V_{in} f_s (Q_{SW1} + Q_{SW2}) + V_{in} I_{ctrl} \end{aligned} \tag{A.1}$$

$$\Delta I = \frac{V_{out}(1 - \frac{V_{out}}{V_{in}})}{L_f f_s} \tag{A.2}$$

A.2 Proof of Lemma 3.2

According to the previous research [101], the power consumption of the boost-mode DC-DC regulator is approximated to Equation (A.3).

$$P_{boost} = (\frac{I_{out} V_{out}}{V_{in}})^2 (R_L + R_{SW1} + R_{SW3}) + V_{out} f_s (Q_{SW3} + Q_{SW4}) + V_{in} I_{ctrl} \tag{A.3}$$

When the input voltage ($V_{in} = V_{sc}$) is low, the power consumption of the boost controller $V_{in}I_{ctrl}$ is low (Based on the datasheet of the off-the-shelf boost DC-DC regulator [79], when the output current is lower than $50\,\mathrm{mA}$, $V_{in}I_{ctrl} < 100\,\mu\mathrm{W}$, while the overall DC-DC power consumption ranges from 1 to $10\,\mathrm{mW}$). In Equation (A.3), $V_{in}I_{ctrl}$ can be dropped. Moreover, the SC leakage power P_{leak} is negligible when V_{sc} is low. For a Maxwell $10\,\mathrm{F}$ SC, when $V_{sc} = 1.8\,\mathrm{V}$, the leakage power is $0.6\,\mu\mathrm{W}$[1]. The overall IoBT system power consumption is simplified to Equation (A.4), which shows that P_{loss} decreases monotonically with SC terminal voltage V_{sc}.

$$P_{loss} = (\frac{I_{out}V_{out}}{V_{in}})^2(R_L + R_{SW1} + R_{SW3}) + V_{out}f_s(Q_{SW3} + Q_{SW4}) \tag{A.4}$$

To validate the approximation, Figure A.1 compares the original IoBT system power loss model with the approximation model in the boost mode ($V_{thd} \leq V_{sc} \leq V_{dd}$, $V_{dd} = 1.8\,\mathrm{V}$). The parameters of the DC-DC converter come from [79] with the start-up threshold $V_{thd} = 0.9\,\mathrm{V}$. Figure A.1 shows that with different output current I_{out}, the approximation model (solid lines) matches well with the original model (dotted lines). Moreover, the trend of the curves in Figure A.1 verifies that the approximated model retains the same monotonicity as the original model.

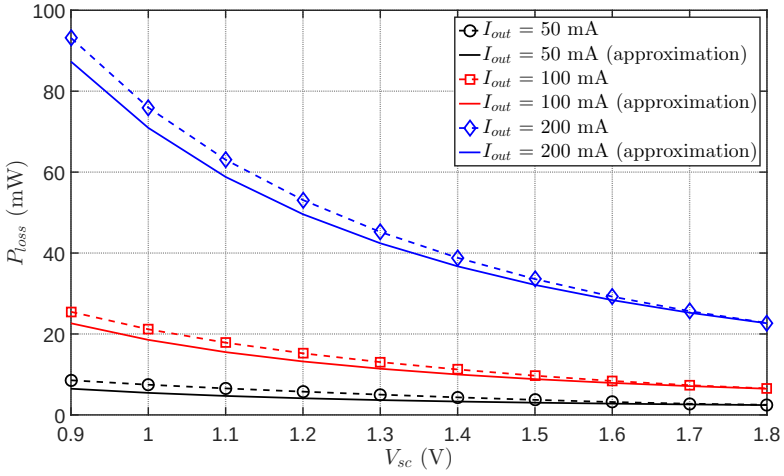

Figure A.1: Validation of the approximated IoBT power loss model in the boost mode

[1]The SC model parameters come from [64]

APPENDIX B

PROOF FOR CHAPTER 4

B.1 Proof of Proposition 4.1

According to Algorithm 4.1, the finalized rate vector $\boldsymbol{r}(t) = [r_1(t), ..., r_n(t)]$ indicates that all the CM nodes are saturated. For arbitrary CM node j, at least one of the Equations (B.1) and (B.2) needs to hold so that the rate $r_j(t)$ is saturated.

$$\begin{aligned} &S_{CH}(r_1(t), ..., r_j(t), ..., r_n(t)) \leq B_{CH}(t) \\ &\leq S_{CH}(r_1(t), ..., r_j(t) + s, ..., r_n(t)) \end{aligned} \tag{B.1}$$

$$S_j(r_j(t)) \leq B_j(t) \leq S_j(r_j(t) + s) \tag{B.2}$$

Considering that the step size s in Algorithm 4.1 can be arbitrarily small, Equations (B.1) and (B.2) are formulated to be Equations (B.3) and (B.4), respectively.

$$\lim_{s \to 0^+} S_{CH}(r_1(t), ..., r_j(t), ..., r_n(t)) = B_{CH}(t) \tag{B.3}$$

$$\lim_{s \to 0^+} S_j(r_j(t)) = B_j(t) \tag{B.4}$$

If $CH \in \bar{Q}_t$, then based on Definition 4.1, there exists an $e > 0$ that $S_{CH}(r_1(t), ..., r_n(t)) \in [0, B_{CH}(t) - e]$. Equation (B.3) does not hold when $CH \in \bar{Q}_t$. Consequently, Equation (B.4) holds for any CM node j. Thus, all the CM nodes are energy throttled.

B.2 Proof of Proposition 4.2

Part (1) of Proposition 4.2 can be directly proven by analyzing Algorithm 4.1. In Algorithm 4.1, if a CM node j becomes energy throttled in the tth round, then its data collection rate $r_j(t)$ is saturated. At the same time, for other energy sufficient CM nodes, their transmission rates are still available for increment until either themselves or the CH node becomes energy throttled. Thus, Equation (B.5) is valid for any CM nodes $k, j \in V_{CM}$.

$$r_k(t) \geq r_j(t), \quad k \in \bar{Q}_t,\ j \in Q_t \tag{B.5}$$

For any arbitrary CM nodes a and b, if $a, b \in \bar{Q}_t$, Equation (B.10) is obtained based on the fair rate increment of Algorithm 4.1. Part (2) of Proposition 4.2 is proven.

$$|r_a(t) - r_b(t)| \leq s \tag{B.6}$$

Considering that the step size s can be arbitrary small, it is valid that $r_a(t) = r_b(t)$.

Since $V = Q_t \cup \bar{Q}_t$, by combing parts (1) and (2), part (3) of Proposition 4.2 is proven.

B.3 Proof of Theorem 4.1

Theorem 4.1 is proven by contradiction. Assume the rate vector $\boldsymbol{r}(t) = [r_1(t), ..., r_n(t)]$ assigned by Algorithm 4.1 is not lexicographically optimal. According to the previous literature [51], the optimum lexicographic rate assignment is unique for an arbitrary network. Then, there exists a lexicographically optimal rate vector $\boldsymbol{r}'(t) = [r'_1(t), ..., r'_n(t)]$. Based on Definition 4.1, $\boldsymbol{r}'(t)$ is lexicographically greater than $\boldsymbol{r}(t)$. There exists a CM node i such that $r'_i(t) > r_i(t)$ and $r'_j(t) = r_j(t)$ for any $1 \leq j \leq i-1$.

With the rate vector $\boldsymbol{r}(t)$ assigned by Algorithm 4.1, there are two cases: (1) $CH \in \bar{Q}_t$; (2) $CH \in Q_t$.

Case 1: If $CH \in \bar{Q}_t$, according Proposition 4.1, all the CM nodes are energy throttled

with the assignment $\boldsymbol{r}(t)$. It is not feasible to find a CM node i with $r_i'(t) > r_i(t)$. A higher transmission rate $r_i'(t)$ will have to violate the energy constrain. Thus, the rate vector $\boldsymbol{r}'(t)$ is infeasible.

Case 2: When $CH \in Q_t$, the CH node is energy throttled with the assignment $\boldsymbol{r}(t)$. If the assignment $\boldsymbol{r}'(t)$ is feasible, there at least exist an $m > i$ such that $r_m'(t) < r_m(t)$. Then:

$$r_i(t) < r_i'(t) < r_m'(t) < r_m(t) \tag{B.7}$$

Equation (B.7) indicates that the CM node i is energy sufficient due to the existence of a higher rate $r_i'(t)$. Then, based on part (3) of Proposition 4.2, it can be inferred that $r_i(t) \geq r_m(t)$ because the energy sufficient CM node has the highest transmission rate over all the other CM nodes. Thus, there does not exist such rate vector $\boldsymbol{r}'(t)$.

Combining Case 1 and Case 2, Algorithm 4.1 computes the optimum lexicographic rate assignment for an IoBT cluster.

B.4 Proof of Proposition 4.3

For any $i, j, k \in V$ and $j \neq k \neq i$, if $\lambda_{i,j}^{rx} = \lambda_{i,k}^{rx}$, then Equation (B.8) is valid for any node i (Recall that Λ_{max}^{rx} and Λ_{max}^{rx} are defined in line 7 and line 8 in Algorithm 4.3, respectively.).

$$\lambda_i^{rx} = \Lambda_{max}^{rx} = \Lambda_{min}^{rx} \tag{B.8}$$

Equation (4.3) can be rewritten as:

$$S_{CH}(t) = T\lambda_i^{rx}\frac{R_{CH}(t)}{\rho} + T\lambda^{DA}\frac{R_{CH}(t)}{\rho} + T\lambda_{CH,BS}^{tx}R_{CH}(t) \tag{B.9}$$

An optimum CH selection algorithm needs to elect the CH node with the highest data collection rate. Assuming node i is selected as the CH node, there are two possibilities when LRIC assigns a rate vector: (1) $i \in \bar{Q}_t$; (2) $i \in Q_t$.

Case 1. If the CH node i is energy sufficient, then its remaining energy $B_i(t)$ has a lower bound shown in Equation (B.10). According to Proposition 4.1, all the CM nodes must be energy throttled. Then, the rate of any CM node j can be derived by Equation (B.11).

$$B_i(t) > T\lambda_i^{rx} \sum_{j \in V_{CM}} r_j(t) + (T\lambda^{DA} + \rho T\lambda_{i,BS}^{tx}) \sum_{j \in V_{CM}} r_j(t) \tag{B.10}$$

$$r_j(t) = \frac{B_j(t)}{T\lambda_{j,i}^{tx}} \tag{B.11}$$

Based on Equation (4.4), the CH data rate is derived. Line 9 to 10 in Algorithm 4.3 follows the same logic to derive the CH data rate when the CH node is energy sufficient.

Case 2. When the CH node i is energy throttled, then:

$$B_i(t) = T \cdot \lambda_i^{rx} \sum_{j \in V_{CM}} r_j(t) + (T\lambda^{DA} + \rho T\lambda_{i,BS}^{tx}) \sum_{j \in V_{CM}} r_j(t) \tag{B.12}$$

The CH rate $r_i(t)$ is derived from Equation (4.4), as shown in Equation (B.13).

$$r_i(t) = \frac{\rho B_i(t)}{T(\lambda_i^{rx} + \lambda^{DA} + \rho\lambda_{i,BS}^{tx})} \tag{B.13}$$

Line 11 to 15 in Algorithm 4.3 uses the same equations to derive the CH rate when the CH node is energy throttled.

Combining cases 1 and 2, Algorithm 4.3 computes the data collection rate for each candidate IoBT nodes and then select the one with the highest rate. Thus, Algorithm 4.3 is optimal when the receiving costs from different senders are the same.

APPENDIX C

PROOF FOR CHAPTER 5

C.1 Proof of Proposition 5.1

Part (1) of Proposition 5.1 comes from the fair increment process of Algorithm 5.1. In Algorithm 5.1, if an IoBT node j becomes resource throttled in the tth slot, then its data segment size can not be augmented any more. On the other hand, for any resource sufficient node k, it is still valid to increment its data size until either node k becomes resource throttled or the remaining data size L_{rem} becomes zero. Therefore, Equation (C.1) is valid for any nodes $j, k \in \mathcal{V}$.

$$d_k(t) \geq d_j(t) \quad k \in \bar{Q}_t^{\boldsymbol{l}},\ j \in Q_t^{\boldsymbol{l}} \tag{C.1}$$

Similarly, part (2) of Proposition 5.1 can also be derived from the fair increment of the node latency in Algorithm 5.1. For any nodes $x, y \in \bar{Q}_t^{\boldsymbol{l}}$, Equation (C.2) is obtained. Considering that the time step size δ can be arbitrary small, it can be proven that $d_x(t) = d_y(t)$.

$$|d_x(t) - d_y(t)| \leq \delta \tag{C.2}$$

Since $\mathcal{V} = Q_t^{\boldsymbol{l}} \cup \bar{Q}_t^{\boldsymbol{l}}$, by combining parts (1) and (2), part (3) of Proposition 5.1 is validated.

C.2 Proof of Theorem 5.1

Theorem 5.1 can be proved by contradiction. Assume the partition $\boldsymbol{l}(t) = [l_1(t), ..., l_n(t)]$ derived from Algorithm 5.1 is not optimal. $\boldsymbol{d}(t) = [d_1(t), ..., d_n(t)]$ refers to the corre-

sponding node latency with the partition $\boldsymbol{l}(t)$. Then, there exists another feasible partition $\boldsymbol{l'}(t) = [l'_1(t), ..., l'_n(t)]$ with less overall latency. $\boldsymbol{d'}(t) = [d'_1(t), ..., d'_n(t)]$ refers to the nodal latency vector with the partition $\boldsymbol{l'}(t)$. In the latency vector $\boldsymbol{d}(t)$, node m is assumed to have the largest nodal latency, as shown in Equation (C.3). Similarly, node k is assumed to have the largest nodal latency, as shown in Equation (C.4). Equation (C.5) is derived based on Equation (5.25).

$$d_m(t) = \max_{i \in \mathcal{V}} d_i(t) \tag{C.3}$$

$$d'_k(t) = \max_{i \in \mathcal{V}} d'_i(t) \tag{C.4}$$

$$d'_k(t) < d_m(t) \tag{C.5}$$

For node k, there are two possible cases when comparing $d_k(t)$ and $d'_k(t)$: 1) $d'_k(t) \leq d_k(t)$; and 2) $d'_k(t) > d_k(t)$.

Case 1: If $d'_k(t) \leq d_k(t)$, Equation (C.6) is derived based on Equation (5.17).

$$l'_k(t) \leq l_k(t) \tag{C.6}$$

For both partitions $\boldsymbol{l}(t)$ and $\boldsymbol{l'}(t)$, the total data size equals to L. In order for the partition $\boldsymbol{l'}(t)$ to be valid, there at least exist a $q \in \mathcal{V}$ such that $l'_q(t) \geq l_q(t)$. Therefore, there exists a node q for Equation (C.7).

$$d'_q(t) \geq d_q(t) \tag{C.7}$$

Due to the fact that $l'_q(t) \geq l_q(t)$, Proposition 5.2 indicates that $q \in \bar{Q}_t^{\boldsymbol{l}}$. Equation (C.8)

is obtained according to part (3) of Proposition 5.1.

$$d_q(t) = \max_{i \in \mathcal{V}} d_i(t) = d_m(t) > d'_k(t) >= d'_q(t) \tag{C.8}$$

Consequently, Equation (C.8) contradicts with Equation (C.7). There does not exist such partition $l'(t)$.

Case 2: If $d'_k(t) > d_k(t)$, Equation (5.17) indicates that $l'_k(t) > l_k(t)$. Based on Proposition 5.2, $k \in \bar{Q}_t^{\boldsymbol{l}}$ with the partition $\boldsymbol{l}(t)$. Equation (C.9) is derived based on part (3) of Proposition 5.1.

$$d_k(t) = \max_{i \in \mathcal{V}} d_i(t) = d_m(t) > d'_k(t) \tag{C.9}$$

Equation (C.9) contradicts to the condition $d'_k(t) > d_k(t)$. Thus, the partition $\boldsymbol{l'}(t)$ is not valid.

Combining cases 1 and 2, it is verified that there does not exist another partition with less overall latency. Algorithm 5.1 is validated to be optimal.

REFERENCES

[1] I. F. Akyildiz, S. Nie, S.-C. Lin, and M. Chandrasekaran, "5g roadmap: 10 key enabling technologies," *Computer Networks*, vol. 106, pp. 17–48, 2016.

[2] J. A. Stankovic, "Research directions for the internet of things," *IEEE Internet of Things Journal*, vol. 1, no. 1, pp. 3–9, 2014.

[3] L. Da Xu, W. He, and S. Li, "Internet of things in industries: A survey," *Industrial Informatics, IEEE Transactions on*, vol. 10, no. 4, pp. 2233–2243, 2014.

[4] S. Yang, X. Yang, J. McCann, T. Zhang, G. Liu, Z. Liu, *et al.*, "Distributed networking in autonomic solar powered wireless sensor networks," *Selected Areas in Communications, IEEE Journal on*, vol. 31, no. 12, pp. 750–761, 2013.

[5] R. Shigeta, T. Sasaki, D. M. Quan, Y. Kawahara, R. J. Vyas, M. M. Tentzeris, and T. Asami, "Ambient rf energy harvesting sensor device with capacitor-leakage-aware duty cycle control," *Sensors Journal, IEEE*, vol. 13, no. 8, pp. 2973–2983, 2013.

[6] F. Hu, X. Liu, M. Shao, D. Sui, and L. Wang, "Wireless energy and information transfer in wban: An overview," *IEEE Network*, vol. 31, no. 3, pp. 90–96, 2017.

[7] M. Gorlatova, J. Sarik, G. Grebla, M. Cong, I. Kymissis, and G. Zussman, "Movers and shakers: Kinetic energy harvesting for the internet of things," in *The 2014 ACM international conference on Measurement and modeling of computer systems*, ACM, 2014, pp. 407–419.

[8] Q. Ju, H. Li, and Y. Zhang, "Towards human-powered iot: Optimizing harvested power from human daily motion," in *Ubiquitous Computing, Electronics and Mobile Communication Conference (UEMCON), 2017 IEEE 8th Annual*, IEEE, 2017, pp. 197–202.

[9] M. Collotta and G. Pau, "A novel energy management approach for smart homes using bluetooth low energy," *IEEE Journal on Selected Areas in Communications*, vol. 33, no. 12, pp. 2988–2996, 2015.

[10] V. C. Gungor, B. Lu, and G. P. Hancke, "Opportunities and challenges of wireless sensor networks in smart grid," *IEEE transactions on industrial electronics*, vol. 57, no. 10, pp. 3557–3564, 2010.

[11] B. Buchli, F. Sutton, J. Beutel, and L. Thiele, "Dynamic power management for long-term energy neutral operation of solar energy harvesting systems," in *Proceed-*

ings of the 12th ACM Conference on Embedded Network Sensor Systems, ACM, 2014, pp. 31–45.

[12] A. Kansal, J. Hsu, S. Zahedi, and M. B. Srivastava, "Power management in energy harvesting sensor networks," *ACM Transactions on Embedded Computing Systems (TECS)*, vol. 6, no. 4, p. 32, 2007.

[13] M. Pedram, N. Chang, Y. Kim, and Y. Wang, "Hybrid electrical energy storage systems," in *Low-Power Electronics and Design (ISLPED), 2010 ACM/IEEE International Symposium on*, IEEE, 2010, pp. 363–368.

[14] J. Taneja, J. Jeong, and D. Culler, "Design, modeling, and capacity planning for micro-solar power sensor networks," in *Proceedings of the 7th international conference on Information processing in sensor networks*, IEEE Computer Society, 2008, pp. 407–418.

[15] X. Jiang, J. Polastre, and D. Culler, "Perpetual environmentally powered sensor networks," in *Information Processing in Sensor Networks, 2005. IPSN 2005. Fourth International Symposium on*, IEEE, 2005, pp. 463–468.

[16] C. Abbey and G. Joos, "Supercapacitor energy storage for wind energy applications," *IEEE Transactions on Industry Applications*, vol. 43, no. 3, p. 769, 2007.

[17] J. Hester, L. Sitanayah, and J. Sorber, "Tragedy of the coulombs: Federating energy storage for tiny, intermittently-powered sensors," in *Proceedings of the 13th ACM Conference on Embedded Networked Sensor Systems*, ACM, 2015, pp. 5–16.

[18] V. Liu, A. Parks, V. Talla, S. Gollakota, D. Wetherall, and J. R. Smith, "Ambient backscatter: Wireless communication out of thin air," in *ACM SIGCOMM Computer Communication Review*, ACM, vol. 43(4), 2013, pp. 39–50.

[19] T. Zhu, Z. Zhong, Y. Gu, T. He, and Z.-L. Zhang, "Leakage-aware energy synchronization for wireless sensor networks," in *Proceedings of the 7th international conference on Mobile systems, applications, and services*, ACM, 2009, pp. 319–332.

[20] Y. Zhao, J. R. Smith, and A. Sample, "Nfc-wisp: A sensing and computationally enhanced near-field rfid platform," in *RFID (RFID), 2015 IEEE International Conference on*, IEEE, 2015, pp. 174–181.

[21] H. Yang and Y. Zhang, "Analysis of supercapacitor energy loss for power management in environmentally powered wireless sensor nodes," *IEEE transactions on power electronics*, vol. 28, no. 11, pp. 5391–5403, 2013.

[22] R. Chai and Y. Zhang, "A practical supercapacitor model for power management in wireless sensor nodes," *Power Electronics, IEEE Transactions on*, vol. 30, no. 12, pp. 6720–6730, 2015.

[23] Q. Ju and Y. Zhang, "Predictive power management for internet of battery-less things," *IEEE Transactions on Power Electronics*, vol. 33, no. 1, pp. 299–312, 2018.

[24] Y. Wang, Y. Liu, C. Wang, Z. Li, X. Sheng, H. G. Lee, N. Chang, and H. Yang, "Storage-less and converter-less photovoltaic energy harvesting with maximum power point tracking for internet of things," *IEEE Transactions on Computer-Aided Design of Integrated Circuits and Systems*, vol. 35, no. 2, pp. 173–186, 2016.

[25] Y. Choi, N. Chang, and T. Kim, "Dc–dc converter-aware power management for low-power embedded systems," *Computer-Aided Design of Integrated Circuits and Systems, IEEE Transactions on*, vol. 26, no. 8, pp. 1367–1381, 2007.

[26] W. Dargie, "Dynamic power management in wireless sensor networks: State-of-the-art," *Sensors Journal, IEEE*, vol. 12, no. 5, pp. 1518–1528, 2012.

[27] J. Hsu, S. Zahedi, A. Kansal, M. Srivastava, and V. Raghunathan, "Adaptive duty cycling for energy harvesting systems," in *Proceedings of the 2006 international symposium on Low power electronics and design*, ACM, 2006, pp. 180–185.

[28] C. M. Vigorito, D. Ganesan, and A. G. Barto, "Adaptive control of duty cycling in energy-harvesting wireless sensor networks," in *Sensor, Mesh and Ad Hoc Communications and Networks, 2007. SECON'07. 4th Annual IEEE Communications Society Conference on*, IEEE, 2007, pp. 21–30.

[29] S. Chen, P. Sinha, N. B. Shroff, and C. Joo, "A simple asymptotically optimal energy allocation and routing scheme in rechargeable sensor networks," in *INFOCOM, 2012 Proceedings IEEE*, IEEE, 2012, pp. 379–387.

[30] J. R. Piorno, C. Bergonzini, D. Atienza, and T. S. Rosing, "Prediction and management in energy harvested wireless sensor nodes," in *Wireless Communication, Vehicular Technology, Information Theory and Aerospace & Electronic Systems Technology, 2009. Wireless VITAE 2009. 1st International Conference on*, IEEE, 2009, pp. 6–10.

[31] N. Sharma, J. Gummeson, D. Irwin, and P. Shenoy, "Cloudy computing: Leveraging weather forecasts in energy harvesting sensor systems," in *Sensor Mesh and Ad Hoc Communications and Networks (SECON), 2010 7th Annual IEEE Communications Society Conference on*, IEEE, 2010, pp. 1–9.

[32] C. Renner, "Solar harvest prediction supported by cloud cover forecasts," in *Proceedings of the 1st International Workshop on Energy Neutral Sensing Systems*, ACM, 2013, p. 1.

[33] M. Gorlatova, A. Wallwater, and G. Zussman, "Networking low-power energy harvesting devices: Measurements and algorithms," *Mobile Computing, IEEE Transactions on*, vol. 12, no. 9, pp. 1853–1865, 2013.

[34] C. Renner, S. Unterschütz, V. Turau, and K. Römer, "Perpetual data collection with energy-harvesting sensor networks," *ACM Transactions on Sensor Networks (TOSN)*, vol. 11, no. 1, p. 12, 2014.

[35] Q. Ju, S.-T. Chen, and Y. Zhang, "Benchmarking renderscript: Potential for energy efficient multi-core mobile devices," in *Sensing, Communication, and Networking-Workshops (SECON Workshops), 2015 12th Annual IEEE International Conference on*, IEEE, 2015, pp. 1–6.

[36] S. Liu, J. Lu, Q. Wu, and Q. Qiu, "Harvesting-aware power management for real-time systems with renewable energy," *Very Large Scale Integration (VLSI) Systems, IEEE Transactions on*, vol. 20, no. 8, pp. 1473–1486, 2012.

[37] X. Lin, Y. Wang, N. Chang, and M. Pedram, "Concurrent task scheduling and dynamic voltage and frequency scaling in a real-time embedded system with energy harvesting," *IEEE Transactions on Computer-Aided Design of Integrated Circuits and Systems*, vol. 35, no. 11, pp. 1890–1902, 2016.

[38] B. Zhang, R. Simon, and H. Aydin, "Harvesting-aware energy management for time-critical wireless sensor networks with joint voltage and modulation scaling," *Industrial Informatics, IEEE Transactions on*, vol. 9, no. 1, pp. 514–526, 2013.

[39] A. Zappone, L. Sanguinetti, G. Bacci, E. Jorswieck, and M. Debbah, "Energy-efficient power control: A look at 5g wireless technologies," *IEEE Transactions on Signal Processing*, vol. 64, no. 7, pp. 1668–1683, 2016.

[40] G. Sun, Y. Liu, S. Liang, Z. Chen, A. Wang, Q. Ju, and Y. Zhang, "A sidelobe and energy optimization array node selection algorithm for collaborative beamforming in wireless sensor networks," *IEEE Access*, 2017.

[41] H. Moosavi and F. M. Bui, "Optimal relay selection and power control with quality-of-service provisioning in wireless body area networks," *IEEE Transactions on Wireless Communications*, vol. 15, no. 8, pp. 5497–5510, 2016.

[42] W. Zang, S. Zhang, and Y. Li, "An accelerometer-assisted transmission power control solution for energy-efficient communications in wban," *IEEE Journal on Selected Areas in Communications*, vol. 34, no. 12, pp. 3427–3437, 2016.

[43] S. Lin, J. Zhang, G. Zhou, L. Gu, J. A. Stankovic, and T. He, "Atpc: Adaptive transmission power control for wireless sensor networks," in *Proceedings of the 4th international conference on Embedded networked sensor systems*, ACM, 2006, pp. 223–236.

[44] A. Castagnetti, A. Pegatoquet, T. N. Le, and M. Auguin, "A joint duty-cycle and transmission power management for energy harvesting wsn," *Transactions on Industrial Informatics*, vol. 10, no. 20, pp. 928–936, 2014.

[45] Y. Fu, M. Sha, G. Hackmann, and C. Lu, "Practical control of transmission power for wireless sensor networks," in *Network Protocols (ICNP), 2012 20th IEEE International Conference on*, IEEE, 2012, pp. 1–10.

[46] T. N. Le, A. Pegatoquet, O. Berder, and O. Sentieys, "Energy-efficient power manager and mac protocol for multi-hop wireless sensor networks powered by periodic energy harvesting sources," *Sensors Journal, IEEE*, vol. 15, no. 12, pp. 7208–7220, 2015.

[47] C. Wu, D. Gunatilaka, A. Saifullah, M. Sha, P. B. Tiwari, C. Lu, and Y. Chen, "Maximizing network lifetime of wirelesshart networks under graph routing," in *2016 IEEE First International Conference on Internet-of-Things Design and Implementation (IoTDI)*, IEEE, 2016, pp. 176–186.

[48] J. Gong, J. S. Thompson, S. Zhou, and Z. Niu, "Base station sleeping and resource allocation in renewable energy powered cellular networks," *IEEE Transactions on Communications*, vol. 62, no. 11, pp. 3801–3813, 2014.

[49] I. Dietrich and F. Dressler, "On the lifetime of wireless sensor networks," *ACM Transactions on Sensor Networks (TOSN)*, vol. 5, no. 1, p. 5, 2009.

[50] Q. Ju and Y. Zhang, "Clustered data collection for internet of battery-less things," *IEEE Internet of Things Journal*, vol. 4, no. 6, pp. 2275–2285, 2017.

[51] K.-W. Fan, Z. Zheng, and P. Sinha, "Steady and fair rate allocation for rechargeable sensors in perpetual sensor networks," in *Proceedings of the 6th ACM conference on Embedded network sensor systems*, ACM, 2008, pp. 239–252.

[52] S. Yang and J. A. McCann, "Distributed optimal lexicographic max-min rate allocation in solar-powered wireless sensor networks," *ACM Transactions on Sensor Networks (TOSN)*, vol. 11, no. 1, p. 9, 2014.

[53] T. He, B. M. Blum, J. A. Stankovic, and T. Abdelzaher, "Aida: Adaptive application-independent data aggregation in wireless sensor networks," *ACM Transactions on Embedded Computing Systems (TECS)*, vol. 3, no. 2, pp. 426–457, 2004.

[54] W. B. Heinzelman, A. P. Chandrakasan, and H. Balakrishnan, "An application-specific protocol architecture for wireless microsensor networks," *IEEE Transactions on wireless communications*, vol. 1, no. 4, pp. 660–670, 2002.

[55] Q. Ju and Y. Zhang, "Adaptive clustering for internet of battery-less things," in *2017 IEEE Wireless Communications and Networking Conference (WCNC)*, San Francisco, USA, Mar. 2017.

[56] O. Younis and S. Fahmy, "Heed: A hybrid, energy-efficient, distributed clustering approach for ad hoc sensor networks," *IEEE Transactions on mobile computing*, vol. 3, no. 4, pp. 366–379, 2004.

[57] D. Wu, J. He, H. Wang, C. Wang, and R. Wang, "A hierarchical packet forwarding mechanism for energy harvesting wireless sensor networks," *IEEE Communications Magazine*, vol. 53, no. 8, pp. 92–98, 2015.

[58] D. Wei, Y. Jin, S. Vural, K. Moessner, and R. Tafazolli, "An energy-efficient clustering solution for wireless sensor networks," *IEEE transactions on wireless communications*, vol. 10, no. 11, pp. 3973–3983, 2011.

[59] M. Armbrust, A. Fox, R. Griffith, A. D. Joseph, R. Katz, A. Konwinski, G. Lee, D. Patterson, A. Rabkin, I. Stoica, *et al.*, "A view of cloud computing," *Communications of the ACM*, vol. 53, no. 4, pp. 50–58, 2010.

[60] M. Satyanarayanan, P. Bahl, R. Caceres, and N. Davies, "The case for vm-based cloudlets in mobile computing," *IEEE pervasive Computing*, vol. 8, no. 4, 2009.

[61] X. Chen, L. Jiao, W. Li, and X. Fu, "Efficient multi-user computation offloading for mobile-edge cloud computing," *IEEE/ACM Transactions on Networking*, vol. 24, no. 5, pp. 2795–2808, 2016.

[62] Y. Mao, J. Zhang, and K. B. Letaief, "Dynamic computation offloading for mobile-edge computing with energy harvesting devices," *IEEE Journal on Selected Areas in Communications*, vol. 34, no. 12, pp. 3590–3605, 2016.

[63] C. Leopold, *Parallel and distributed computing: A survey of models, paradigms and approaches*. John Wiley & Sons, Inc., 2001.

[64] Q. Ju and Y. Zhang, "Reducing charge redistribution loss for supercapacitor-operated energy harvesting wireless sensor nodes," in *Proceedings of the 2nd International Workshop on Energy Neutral Sensing Systems*, ACM, 2014, pp. 31–36.

[65] H. Yang and Y. Zhang, "Self-discharge analysis and characterization of supercapacitors for environmentally powered wireless sensor network applications," *Journal of Power Sources*, vol. 196, no. 20, pp. 8866–8873, 2011.

[66] Y. Zhang and H. Yang, "Modeling and characterization of supercapacitors for wireless sensor network applications," *Journal of Power Sources*, vol. 196, no. 8, pp. 4128–4135, 2011.

[67] MACCOR, *Maccor user manual[online]*. www.maccor.com, 2012.

[68] T. Zhu, Y. Gu, T. He, and Z.-L. Zhang, "Eshare: A capacitor-driven energy storage and sharing network for long-term operation," in *Proceedings of the 8th ACM Conference on Embedded Networked Sensor Systems*, ACM, 2010, pp. 239–252.

[69] Texas Instruments, *Tps6122x datasheet*. 2014.

[70] C. Moser, L. Thiele, D. Brunelli, and L. Benini, "Adaptive power management for environmentally powered systems," *Computers, IEEE Transactions on*, vol. 59, no. 4, pp. 478–491, 2010.

[71] Oak Ridge National Lab, *Oak ridge national lab rotating shadowband radiometer*. 2014.

[72] Atmel, *Atmega 128/128l datasheet*. 2011.

[73] Texas Instruments, *Cc2420: 2.4 ghz ieee 802.15.4 / zigbee-ready rf transceiver (rev. c)*. 2014.

[74] C. Alippi, G. Anastasi, M. Di Francesco, and M. Roveri, "Energy management in wireless sensor networks with energy-hungry sensors," *Instrumentation & Measurement Magazine, IEEE*, vol. 12, no. 2, pp. 16–23, 2009.

[75] C. Bergonzini, D. Brunelli, and L. Benini, "Comparison of energy intake prediction algorithms for systems powered by photovoltaic harvesters," *Microelectronics Journal*, vol. 41, no. 11, pp. 766–777, 2010.

[76] M. A. G. De Brito, L. Galotto, L. P. Sampaio, G. d. A. e Melo, and C. A. Canesin, "Evaluation of the main mppt techniques for photovoltaic applications," *IEEE transactions on industrial electronics*, vol. 60, no. 3, pp. 1156–1167, 2013.

[77] F. I. Simjee and P. H. Chou, "Efficient charging of supercapacitors for extended lifetime of wireless sensor nodes," *IEEE Transactions on power electronics*, vol. 23, no. 3, pp. 1526–1536, 2008.

[78] Q. Ju and Y. Zhang, "Charge redistribution-aware power management for supercapacitor-operated wireless sensor networks," *Sensors Journal, IEEE*, vol. 16, no. 7, pp. 2046–2054, 2016.

[79] Texas Instruments, *Tps6100x datasheet*. 2015.

[80] Linear Technology, *Ltc3401 datasheet*. 2001.

[81] Texas Instruments, *Tps6273x datasheet*. 2014.

[82] Maxim Integrated, *Max17620 datasheet*. 2015.

[83] Linear Technology, *Ltc3785 datasheet*. 2007.

[84] Maxim Integrated, *Max77801 datasheet*. 2015.

[85] M. Z. Zamalloa and B. Krishnamachari, "An analysis of unreliability and asymmetry in low-power wireless links," *ACM Transactions on Sensor Networks (TOSN)*, vol. 3, no. 2, p. 7, 2007.

[86] M. A. Landolsi and W. E. Stark, "On the accuracy of gaussian approximations in the error analysis of ds-cdma with oqpsk modulation," *Communications, IEEE Transactions on*, vol. 50, no. 12, pp. 2064–2071, 2002.

[87] Texas Instruments, *Cc2500: Low-cost low-power 2.4 ghz rf transceiver*. 2014.

[88] P. Zhang, G. Xiao, and H.-P. Tan, "Clustering algorithms for maximizing the lifetime of wireless sensor networks with energy-harvesting sensors," *Computer Networks*, vol. 57, no. 14, pp. 2689–2704, 2013.

[89] S. Lin, F. Miao, J. Zhang, G. Zhou, L. Gu, T. He, J. A. Stankovic, S. Son, and G. J. Pappas, "Atpc: Adaptive transmission power control for wireless sensor networks," *ACM Transactions on Sensor Networks (TOSN)*, vol. 12, no. 1, p. 6, 2016.

[90] I. F. Akyildiz and M. C. Vuran, *Wireless sensor networks*. John Wiley & Sons, 2010, vol. 4.

[91] S. Fu, Y. Zhang, Y. Jiang, C. Hu, C.-Y. Shih, and P. J. Marrón, "Experimental study for multi-layer parameter configuration of wsn links," in *Distributed Computing Systems (ICDCS), 2015 IEEE 35th International Conference on*, IEEE, 2015, pp. 369–378.

[92] C. Yang and K.-W. Chin, "On nodes placement in energy harvesting wireless sensor networks for coverage and connectivity," *IEEE Transactions on Industrial Informatics*, vol. 13, no. 1, pp. 27–36, 2017.

[93] A. P. Miettinen and J. K. Nurminen, "Energy efficiency of mobile clients in cloud computing.," *HotCloud*, vol. 10, pp. 4–4, 2010.

[94] Y. Mao, J. Zhang, S. Song, and K. B. Letaief, "Stochastic joint radio and computational resource management for multi-user mobile-edge computing systems," *IEEE Transactions on Wireless Communications*, vol. 16, no. 9, pp. 5994–6009, 2017.

[95] M. Gorlatova, J. Sarik, G. Grebla, M. Cong, I. Kymissis, and G. Zussman, "Movers and shakers: Kinetic energy harvesting for the internet of things," *IEEE Journal on Selected Areas in Communications*, vol. 33, no. 8, pp. 1624–1639, 2015.

[96] S. Zhang and A. Seyedi, "Statistical models for harvested power from human motion," *IEEE Journal on Selected Areas in Communications*, vol. 33, no. 8, pp. 1667–1679, 2015.

[97] S. Pelley, T. F. Wenisch, B. T. Gold, and B. Bridge, "Storage management in the nvram era," *Proceedings of the VLDB Endowment*, vol. 7, no. 2, pp. 121–132, 2013.

[98] W. Zhang, R. K. Mallik, and K. B. Letaief, "Optimization of cooperative spectrum sensing with energy detection in cognitive radio networks," *IEEE transactions on wireless communications*, vol. 8, no. 12, 2009.

[99] K. Kirkpatrick, "Software-defined networking," *Communications of the ACM*, vol. 56, no. 9, pp. 16–19, 2013.

[100] D. Shin, Y. Kim, J. Seo, N. Chang, Y. Wang, and M. Pedram, "Battery-supercapacitor hybrid system for high-rate pulsed load applications," in *Design, Automation & Test in Europe Conference & Exhibition (DATE), 2011*, IEEE, 2011, pp. 1–4.

[101] Y. Zhang, Y. Ge, and Q. Qiu, "Improving charging efficiency with workload scheduling in energy harvesting embedded systems," in *Design Automation Conference (DAC), 2013 50th ACM/EDAC/IEEE*, IEEE, 2013, pp. 1–8.

VITA

Qianao Ju received the B.S. degree and the M.E. degree in electrical engineering from Shanghai Jiao Tong University, Shanghai, in 2010 and 2013, respectively, and the M.S. degree from the School of Electrical and Computer Engineering, Georgia Institute of Technology, Atlanta, GA, in 2013. In August of 2013, he began his doctoral program at the School of Electrical and Computer Engineering, Georgia Institute of Technology. His research interests include Internet of Things, energy harvesting systems, adaptive power management and embedded systems.